



HAL
open science

Mathematical modelling of the contribution of senescent fibroblasts to basement membrane digestion during carcinoma invasion

Luís Almeida, Alexandre Poulain, Albin Pourtier, Chiara Villa

► **To cite this version:**

Luís Almeida, Alexandre Poulain, Albin Pourtier, Chiara Villa. Mathematical modelling of the contribution of senescent fibroblasts to basement membrane digestion during carcinoma invasion. 2024. hal-04574340v2

HAL Id: hal-04574340

<https://hal.science/hal-04574340v2>

Preprint submitted on 7 Jul 2024

HAL is a multi-disciplinary open access archive for the deposit and dissemination of scientific research documents, whether they are published or not. The documents may come from teaching and research institutions in France or abroad, or from public or private research centers.

L'archive ouverte pluridisciplinaire **HAL**, est destinée au dépôt et à la diffusion de documents scientifiques de niveau recherche, publiés ou non, émanant des établissements d'enseignement et de recherche français ou étrangers, des laboratoires publics ou privés.



Distributed under a Creative Commons Attribution 4.0 International License

Mathematical modelling of the contribution of senescent fibroblasts to basement membrane digestion during carcinoma invasion

Luís Almeida¹, Alexandre Poulain^{2,¶}, Albin Pourtier^{3,*}, Chiara Villa^{4,¶,*},

¹ Sorbonne Université, CNRS, Université de Paris, Laboratoire Jacques-Louis Lions UMR 7598, 75005 Paris, France.

² Univ. Lille, CNRS, UMR 8524 - Laboratoire Paul Painlevé, F-59000 Lille, France.

³ Univ. Lille, CNRS, Inserm, CHU Lille, Institut Pasteur Lille, UMR9020-U1277 -CANTHER -Cancer Heterogeneity Plasticity and Resistance to Therapies, F-59000 Lille, France.

⁴ Sorbonne Université, CNRS, Université de Paris, Inria, Laboratoire Jacques-Louis Lions UMR 7598, 75005 Paris, France.

* Corresponding authors. Emails: albin.pourtier@univ-lille.fr, chiara.villa.1@sorbonne-universite.fr

¶ These authors contributed equally to this work.

Abstract

Senescent cells have been recognized to play major roles in tumor progression and are nowadays included in the hallmarks of cancer [46]. Our work aims to develop a mathematical model capable of capturing a pro-invasion effect of senescent fibroblasts located in the conjunctive tissue. We focus in the present article on the first moments of the invasion cascade. Considering a localized epithelial tumor, we model the digestion of the collagen fibers of the basement membrane by the proteolytic enzyme MMP-2. The activation of MMP-2 is modelled in detail, as MT1-MMPs bound to the surface of tumor cells interact with proMMPs and TIMPs, proteins enriched in the secretome of senescent Cancer-Associated Fibroblasts, along with its inhibition by TIMPs. Using numerical simulations of the model, calibrated via an extensive literature search, reproducing biologically relevant scenarios, we test the model's suitability to investigate the effect on basement membrane digestion of fibroblasts presenting a senescence-associated secretory phenotype. Via model reduction, steady state and global sensitivity analyses, we identify the most influential parameters in view of their calibration with empirical data. We conclude the paper discussing mathematical and interdisciplinary perspectives.

1 Introduction

1.1 Biological context

1.1.1 Carcinoma progression

Cancer is a disease characterized by a disorder of the regulatory processes, *i.e.* a disease of cellular homeostasis. Despite the tremendous progress made in the past decades to understand tumor progression and find efficient treatment strategies, cancer persists as the first cause of death in many countries. This is partly due to the extreme complexity of this disease, which involves numerous actors and interlaced biological and physical processes. In particular, other cells (e.g. endothelial cells, fibroblasts, immune cells) in the tumor micro-environment (TME) can act alternatively in favour and against tumor advancement, depending on their activated or altered status along cancer etiology or progression [47, 48].

Carcinomas are tumors that originate in an epithelium (such as lung, breast, colorectum, prostate, stomach, liver, thyroid, cervix, bladder, ...) prior to their progression toward the invasion of their cellular and matrix micro-environment. Carcinomas account for the major part of cancer incidence worldwide (about 20 millions cases) with a mean mortality rate of about 50% worldwide, although the latter varies a lot depending on the country/region [37].

The risk of being diagnosed for a carcinoma is related to ageing [12, 110]. Among the various carcinomas, non-melanoma skin cancers such as basal cell carcinomas or squamous cell carcinomas are amongst those whose incidence will be the most dynamic in the next decades [56]. Hence, although the rate of mortality is moderate in most of these cancers, their massive incidence is already a critical issue.

Typical in solid tumors, carcinoma evolution can be broken down into a series of steps common to rather most types. Tumor initiation occurs from an accumulation of mutations in a single cell, or a few cells, resulting in abnormal proliferation. After a commonly avascular growth, tumors generally stabilise at a diameter of 0.1 – 0.2cm [53], from lack of nutrients and/or space. Regulation by the environment may

52 also occur. At this stage, the carcinoma remains *in situ*, meaning that the epithelial cells are still in their
53 original compartment, touching their underlying basal lamina, physical and anchoring border with the
54 neighbouring conjunctive tissue [93, 88]. Carcinoma progression presents then the basal lamina rupture
55 as a critical point prior to invasion, *i.e.* progression within the TME. The invasion of cancer cells within
56 the surrounding tissue is associated with the development of malignancy, the acquisition of aggressive
57 traits by the cells, and metastasis. Although cancer risk is commonly attributed to intrinsic or inherited
58 mutations, the involvement of age-related perturbations within the TME in the increase of the cancer
59 risk or its progression is clear [71, 110]. In the present article, we are interested in the contributions of
60 senescent stromal cell (fibroblasts) secretions, and particularly MMPs, in the progression of carcinomas
61 in the initial stages of cancer invasion via the digestion of the basement membrane.

62 1.1.2 Basement membrane digestion

63 During invasion, tumor cells need to migrate within the extracellular matrix (ECM) – *i.e.* the network
64 consisting of extracellular macromolecules providing cells with structural support – in the conjunctive
65 tissue (CT), after they have successfully degraded the basement membrane (BM) – *i.e.* a thin layer of dense
66 ECM separating the tumor from the CT. The ECM is made of a network of fibers, with collagen being
67 the most abundant structural protein (amongst others such as elastin, laminin, fibronectin, proteoglycans,
68 glycoproteins, . . .), and is crucial for the homeostasis and the regulation of the cell migration, growth and
69 differentiation. Its cellular and molecular composition varies along ageing [39, 70].

70 Cancer cells can break through dense barriers of ECM using proteolytic enzymes that remodel the
71 ECM's fibers network and expose new routes of invasion. The matrix metalloproteinases (MMPs) class is
72 a large family of proteins, secreted in nonactive forms (proMMPs) and become proteolytically active in the
73 extracellular medium under the action of other proteinases such as Membrane-Type Metalloproteinases
74 (MT-MMPs), but also serine proteinases, furin, or other MMPs. In fact, MMPs also have cross-activating
75 effects on diffusing or soluble MMPs: MMP-2, for instance, may be activated both by MT1-MMP and in-
76 terstitial MMP-1 [72]. MMP activation occurs after successive proteolytic cleavages within the pro-domain
77 and a bait domain leading to a cystein-zinc ion switch that will drive the intra-molecular remodeling of the
78 MMP [108]. The various forms of the MMPs are sensitive to their binding to proteins known as Tissue-
79 Inhibitors of MetalloProteinases (TIMPs). The main function of TIMPs is to act as MMP inhibitors,
80 playing a crucial role in regulating proteolytic degradation in a variety of physiological processes, hence
81 ensuring homeostasis [106]. In cancer, however, the physiological ratio between TIMPs and proMMPs
82 may be disrupted, favoring tumor invasion. TIMPs are commonly found in the TME [27], and produced
83 by stromal cells such as fibroblasts (see *e.g.* [14]).

84 Being interested in BM digestion, in this paper we focus on MMP-2, which is known to digest gelatin
85 and type IV collagen, this latter being one of the main components of the BM [104]. MMP-2 may be
86 overexpressed both by tumor and stromal cells, such as fibroblasts, and it is generally produced in its
87 inactive form. The activation depends on the activity of MT1-MMP that relies on the stabilizing effect of
88 TIMP-2. Indeed, after a stabilized complex composed of two MT1-MMP and one TIMP is formed, pro-
89 MMP-2 is presented to this latter by integrin, resulting in the cleavage of a part of it and, ultimately, the
90 activation of the MMP-2. This effect is therefore dependent on the amount of TIMP-2 in a dose-dependent
91 manner, as an excess of this inhibitory enzyme will disorganize the dimeric MT1-MMP complex and inhibit
92 the interaction with the proMMP-2 protein and this latter activation [54, 72, 85]. Membrane bound
93 MT1-MMP is enriched at tumor invadopodia, *i.e.* specific membrane protrusions where tumor cells invade
94 their TME. MT1-MMP membrane expression shows a turn-over which has been indicated as a necessary
95 function to control proMMP-2 activation and increase collagen digestion [109]. Clear gelatinolytic activity
96 was described in the stromal compartment proximal to damaged BMs in human skin biopsies, from aged
97 and young donors, in association with the detection of cells displaying markers of cancer initiation [81].
98 The basal membrane in aged tissues is thinner in association with profound modifications of molecular
99 and cellular components in the underlying microenvironment contributing to epithelial dysfunctions with
100 potential promotion of cancer [39]. Among the stromal cells in the TME, senescent fibroblasts (SFs) have
101 been observed to secrete pro- and active MMP1 and MMP-2 [81].

102 1.1.3 The role of senescent fibroblasts

103 Senescence is a cellular state characterized by an arrest of proliferation, resistant to apoptosis, resulting
104 from a panel of replicative, oncogenic, oxydative, DNA-impacting, metabolic stresses [11, 76]. Senescent
105 cells accumulate with age in various tissues as in the skin [28]. Among many others, cancer is an age-
106 related disease [12, 110]. In association with the cell-cycle arrest, inducing senescence of cancer cells have

107 been aimed and reported to regulate tumor growth. Cancer progression should however be considered
108 within its microenvironment network of influences. Indeed, while normal mammary fibroblasts can reg-
109 ulate cancerous features of breast epithelial cells in collagen 3D matrices via their secretions and ECM
110 contraction level [78], senescence of stromal cells contribute to tumor progression via a specific secretome
111 the Senescence-Associated Secretory Phenotype, SASP. Therefore, as highlighted in Hanahan’s latest pre-
112 sentation of the hallmarks of cancer [46], senescent cells are nowadays recognized as important contributors
113 to cancer progression via the release a huge amount of proteins – *e.g.* growth factors, chemokines, MMPs
114 – in the TME [36, 23, 24, 49, 64, 69, 81]

115 Senescent fibroblasts as Cancer-Associated Fibroblasts (CAFs) share common features as they display
116 different subsets/impacts depending on their molecular or activation state. Activated CAFs and late senes-
117 cent fibroblasts display mostly similar secretomes. Hence, the acquisition of a senescence-associated secre-
118 tory phenotype by SFs turns them equivalent to a subtype of Cancer-Associated Fibroblasts (CAFs) [5]
119 that similarly secrete proMMP-2 on top of many growth factors, cytokines such as the interleukin IL-
120 8 [107], ECM components and other enzymes that affect the TME similarly to the senescent fibroblasts
121 SASP. In line with the antagonistic pleiotropy hypothesis [97, 35], targeting senescent cells is under active
122 therapeutic trials. The removal of senescent cells *in vivo* was shown to reduce age-related diseases in mice,
123 among which cancer risk [6, 45]. Thus, SFs may promote carcinogenesis and carcinoma progression in aged
124 organisms. The SASP have numerous possible impacts leading to different therapeutical concepts [43, 76].
125 Early steps of cancer invasions rely on basal membrane disruption. The fibroblast’s SASP displays strong
126 MMP levels and activities, and fibroblasts as CAFs contribute to cancer invasion via their MMP-related
127 matrix digestion or via the remodelling the latter (stiff tracks) [5, 111]. Despite accumulating evidence
128 on the impact of SFs in carcinoma progression, much more needs to be achieved in order to identify the
129 net of cellular contributions in order to adapt potential treatment strategies targeting SFs to prevent or
130 slow down cancer invasion. We seek to develop a theoretical platform, initially fed by data from literature
131 and biological data from patient samples or biological models, in order to provide a tool to highlight and
132 manipulate critical actors of the first steps of the age-related cancer risk progression, *i.e.* the digestion of
133 the BM as initial mark of invasion.

134 1.2 Mathematical modelling

135 Mathematical and computational models are nowadays commonly used to study biological systems. They
136 allow to test hypotheses, uncover hidden mechanisms and explore scenarios *in silico*, with limited cost
137 and time engagement. In cancer research, this ultimately helps to improve our understanding of tumor
138 progression and propose treatment optimisation strategies.

139 The field of mathematical oncology has undergone enormous growth in the past thirty years (see for
140 instance the review articles [1, 3, 8, 10, 13, 95] and references therein). The integration of mathematical
141 and computational models into precision oncology is only emerging in recent times, particularly through
142 the development of digital twins [52, 112]. This includes, for instance, their application to radiation
143 treatment of non-melanoma skin cancers [1].

144 Enormous modelling efforts have been made to describe ECM digestion and cancer invasion of the
145 CT, *e.g.* see [33, 99] and references therein. Models comprising systems of partial differential equations
146 (PDEs), which allow for a mechanistic description of the invasion process at the tissue-scale, comprise a
147 particularly prolific branch of this field following the first model proposed by Gatenby and Gawlinski [42].
148 However, while many models have been proposed for different types of movements in the CT, fewer are
149 the works focussing on the role of stroma cells in boosting cancer invasion, on the biochemical reactions
150 responsible for activation of proteolytic enzymes and on the digestion of the BM.

151 1.2.1 Models of cancer invasion promoted by stroma cells

152 Among the many stroma cells that play a role in cancer progression, particular attention has been given
153 to macrophages and fibroblasts, whose prominent role in tumor spread has lead to dedicated studies on
154 Tumor-Associated Macrophages (TAMs) and CAFs. The focus on these stroma cells and cancer-associated
155 phenotypes has indeed spilled over to the mathematical modelling literature.

156 Various works proposed PDE and computational models of tumor spread under the cytotoxic action
157 of macrophages, or TAMs, *e.g.* see [9, 31, 68, 79, 87, 103]. In these works, the crosstalk between tumor
158 cells and macrophages results in the emergence of spatial patterns in the tumor spread. Most models
159 predict these features whilst ignoring ECM degradation, with the emergent behaviour resulting from
160 macrophage infiltration in the tumor, enhanced cell aggregation and cooperative migration. Eftimie and

161 coworkers [9, 103] additionally showed that tumor cell motility can significantly increase in the presence
162 of TAMs, which may secrete MMPs involved in the degradation of the ECM.

163 Other works focused on modelling, using PDEs [66, 65] or agent-based [50] models, the dynamics
164 stemming from the molecular crosstalk between cancer cells and fibroblasts, leading to fibroblast differ-
165 entiation into myofibroblasts [66, 65] or CAFs [50], which then enhanced cancer cell proliferation and
166 motility. Kim *et al.* [66], in particular, reproduced *in silico* a Tumor Chamber Invasion Assay, in which
167 cancer cells and fibroblasts are plated in two chambers separated by a semi-permeable membrane which
168 allows soluble molecules to pass through, but not cells, and its extension including a layer of ECM on
169 the membrane in [65]. In the latter work, myofibroblasts secrete proMMPs which are assumed to become
170 active and degrade the ECM in combination with cancer cells, an assumption which indirectly models
171 the MMP-activating role of MT1-MMPs on the membrane of cancer cells. This simplified approach to
172 modelling MMP activation was also employed by Gallinato *et al.* [41], who proposed a PDE model for
173 the transition of a tumor from the *in situ* stage to the invasive phase, in which fibroblasts in the CT
174 secreted proMMPs. The proteolytic degradation of the BM by active MMPs led to an increase in the BM
175 permeability over time, ultimately allowing cells to pass through.

176 The invasion-boosting effect of SFs was captured by the hybrid model presented by Kim *et al.* [64],
177 which reproduced experimental observations on melanoma invasion. In their work, matrix-degrading
178 enzymes are assumed to be secreted by SFs already in their activated form. Nonetheless, as detailed
179 in Section 1.1.2, MMP activation may involve complex interactions and ultimately TIMPs may play an
180 important role in regulating ECM degradation given its dual role of MMP activator and inhibitor [77].

181 1.2.2 Models of TIMPs-regulated proteolytic degradation of the ECM

182 The first model of MMP-mediated ECM degradation accounting for the complex biochemical reactions
183 responsible for MMP activation was proposed by Karagiannis and Popel [62]. Ignoring spatial dynamics or
184 sources of proMMPs and TIMPs, the model comprises a system of ordinary differential equations (ODEs)
185 and was employed to investigate how varying the initial concentrations of proMMP-2 and TIMP-2 affects
186 the final percentage of collagen digested. The authors found that a high initial TIMP-2 concentration
187 saturates ECM degradation, as expected from its inhibitory function, and that the highest levels of collagen
188 digestions were obtained for intermediate concentrations of TIMP-2, resulting from the key role this protein
189 has in the activation of MMP-2. Analogous results were obtained in [98], who employed a similar model
190 to explore the efficacy of different MMP inhibitors, motivated by the large variety of interactions between
191 complexes formed during MMP-2 activation. The model proposed in [62] was extended by Donze *et al.* [30]
192 to analyse the existence and stability of oscillatory proteolytic dynamics assuming a periodic switch in
193 the role of TIMP-2 as activator or inhibitor of MMP-2. Another extension was proposed by Hoshino
194 *et al.* [55] who included MT1-MMP turnover on the membrane of cancer cells, following experimental
195 results highlighting the importance of MT1-MMP expression on invadopodia for ECM digestion. They
196 found that low turnover rates hindered ECM degradation also due to the key role of MT1-MMP in the
197 MMP-2 activation process, providing a systematic explanation for the experimental observations.

198 Deakin and Chaplain [17] implemented simplified MMP-2 activation dynamics, mediated by TIMP-2
199 and MT1-MMP, in a spatially explicit model of cancer invasion. The model, comprising a system of
200 PDEs, built on the previous work of Chaplain and Lolas [18] which considered ECM digestion by cancer
201 cells to be regulated by the plasminogen activation system. The model in [17], which could already
202 predict complex invasion patterns, assumed proMMP-2 to be already attached to the MT1-MMP-TIMP-2
203 complex and TIMP-2 to be only secreted by cancer cells, and did not include MMP-2 inhibition by TIMP-
204 2. Conversely, in a model of glioma invasion [89] the authors considered the inhibitory effect of TIMP-2
205 on MMP-2, respectively secreted by healthy and cancer cells in the presence of healthy tissue, although
206 MMP-2 was assumed to be secreted already in its active form. The aim of this work was to investigate
207 how the production of TIMP-2 and that of MMP-2 may balance each other to contain invasion. A similar
208 investigation was conducted by Joshi *et al.* [61], who considered a well-mixed system of stem cells to
209 reproduce *in vitro* experiments to elucidate the mechanisms underlying stem cell-based transplantation
210 therapies.

211 Despite the variety of models that have been proposed which consider the role of TIMPs in the
212 proteolytic degradation of the ECM, the few spatially explicit ones focus on the invasion of the CT by
213 cancer cells, assuming the digestion of the BM has already occurred. Indeed, we highlight that in [41] the
214 inhibitory effect of TIMPs is considered using a constant decaying rate in the active MMPs concentration
215 equation. Hence, the dynamics of TIMPs concentration and the dual role (activation/inhibition) that
216 TIMP plays is not represented.

1.2.3 Models of cancer invasion mediated by the digestion of the basal membrane

Ribba *et al.* [94] proposed a modelling framework that represents the digestion of the BM and the healthy tissue to investigate the role of therapies targeting MMPs, modelling both the BM and healthy tissue as d -dimensional domains. Nonetheless, the BM is very thin compared to the rest of the tissue, measuring between 1 and 1.5 μm in width [80], and modelling frameworks considering the BM to be a $d-1$ dimensional manifold portray more accurately the dimensionality of the invasion process. In the works of Kim and coworkers introduced in Section 1.2.1 [65, 66], such multi-dimensional coupling was employed to model the semi-permeable membrane in the Invasion Chamber Assay they were reproducing, while keeping the ECM in [66] as a d -dimensional domain. The thin membrane modelled was permeable only to soluble molecules, which satisfied the transmission conditions derived by Friedman *et al.* [40] via homogenization, and not cells, which satisfied no-flux boundary conditions.

Such multi-dimensional coupling has been employed in the PDE model of BM invasion by tumor cells proposed by Gallinato *et al.* [41]. In their model, the authors apply nonlinear Kedem-Katchalsky transmission conditions [63, 67] across the BM, which describe the discontinuity of the pressure across the thin weakly porous membrane as a linear function of the flux. This discontinuity depends on permeability of the membrane, which in [41] is assumed to increase over time under the proteolytic action of MMPs, as previously described in Section 1.2.1. Chaplain *et al.* [19] presented a formal derivation of biophysically-consistent transmission conditions which, compared to those in [41], allow the cell volume fraction to also be discontinuous across the membrane, while ensuring mass conservation. These conditions, which were later extended to the case of multiple populations in [44] and rigorously derived in [21], can be regarded as a nonlinear generalisation of the classical Kedem-Katchalsky interface conditions [63]. In [19], in particular, they capture BM digestion leading to cancer invasion by letting the effective mobility coefficient depend on the local concentration of MMPs, released by cancer cells in the active form.

The selected literature review we presented showcases the very rich research in tumor invasion modelling, with many elements of the biological system we seek to model. However, recent empirical observations on the role of SF secretome on carcinoma invasion, which includes both proMMP-2 and TIMP-2, calls for further development of these modelling frameworks.

1.3 Scope and outline of the paper

In the present work, we propose a biophysically consistent mathematical model of BM digestion by MMP-2, which are produced in their inactive form together with TIMP-2 by SFs in the stroma, and activated by TIMP-2 and MT1-MMPs expressed on the surface of cancer cells. To the authors' knowledge a mathematical model that captures accurately this dynamics while representing the evolution of the BM density in both time and space does not exist in the literature.

The model, comprising a system of PDEs and ODEs, combines the following features:

- i. secretome spatiotemporal dynamics in the CT, including secretion by SFs modelled as local sources in the stroma;
- ii. transmission of SF secretome from the stroma to the BM;
- iii. detailed biochemical reactions regulating MMP-2 activation at the BM;
- iv. BM digestion by active MMP-2.

We model the BM as a $d-1$ dimensional manifold (where d is the dimension of the domain modelling the stroma), and let the biochemical reactions regulating MMP activation occur in this domain, aided by cancer cells in the strict vicinity of the BM. It is important to consider that the amount of soluble molecules coming from the CT contributing to the MMP activation dynamics may be lowered as these molecules pass from the CT to the BM, the latter being more dense and thus less permeable. Moreover, the utilization of these molecules in the activation cascade may affect their overall dynamics, *e.g.* by resulting in a sink at the boundary corresponding to the BM. To ensure these biophysical effects are not neglected, we formally derive the transmission conditions of SF secretome at the BM by performing a dimensionality reduction procedure on the extended model in which the BM is modelled as a d -dimensional domain. These phenomena, which were not captured in [19, 41], represent an important element of novelty introduced in our work, together with the comprehensive framework including all of the dynamics listed in points i-iv above.

The model aims to capture accurately the biological phenomena described above and to be tractable. To improve analytical and computational tractability, also in view of model calibration with experimental data and model extensions, we derive a reduced model under simplifying assumptions and study this latter analytically. Via numerical simulations and global sensitivity analyses, we explore biological scenarios and compare the sensitivity of the two models, to ensure key elements of the model's predictive capability

273 are not lost during model reduction. Using relevant parameter values carefully drawn from the literature
274 (that rely on dosages and experimental measurements), the numerical simulations of our model illustrate
275 the model’s ability to accurately describe the rupture of the BM, and the potential effect of SFs on tumor
276 progression from the *in situ* stage to the invasive one.

277 The paper is organized as follows: the model assumptions and equations are presented in Section 2;
278 the reduced model is summarized in Section 2.3 together with selected key analytical results; results of
279 the numerical simulations and global sensitivity analyses are outlined in Section 3; a discussion of the
280 results and research perspectives is given in Section 4.2, particularly in view of the model’s extension to
281 a comprehensive framework investigating tumor invasion aided by stroma cells. A list of frequently used
282 acronyms can be consulted at the end of the manuscript (Table 4).

283 2 Methods

284 2.1 The mathematical model

285 2.1.1 Model assumptions

286 We consider a potentially invasive tumour in a healthy non-proliferating tissue, focusing on the stage at
287 which the tumour is isolated and separated from the CT by a dense BM. The BM permeability depends
288 on the local density of ECM, and cancer cells may invade the CT only if the ECM density is sufficiently
289 lowered by proteolytic degradation. In order to study the effect of the position of the SFs and the rate
290 at which they secrete TIMPs and proMMPs on the digestion of the BM, we consider a reduced model of
291 SFs’ secretome dynamics in the CT, and ECM degradation at the BM mediated by MMP-2 activation.
292 In particular, the model reduction is based on the following assumptions and simplifications:

- 293 • We do not model explicitly the healthy cells but we take into account the ECM remodelling effect
294 of healthy cells near the BM.
- 295 • We assume cancer cell proliferation has reached saturation near the BM due to the physical con-
296 straints imposed by it. Therefore, we neglect the spatio-temporal dynamics of cancer cells, but do
297 take into account the fact that a higher cell density near the BM results in higher concentrations of
298 molecules involved in MMP-2 activation.
- 299 • We neglect the proteolytic action of MT1-MMPs in order to focus on their role in MMP-2 activation.
300 We also neglect the secretion of endogenous proMMP-2 by tumor cells.
- 301 • We do not model dynamics of specific integrins (*e.g.* $\alpha v\beta 3$ or $\beta 1$) and their important roles in the
302 activation cascade of MMP-2, but we assume that this effect is captured within specific parameters
303 (*i.e.* the reaction rates of our system).

304 We propose a model which translates into mathematical terms the following biological assumptions:

- 305 A1. The collagen fibers in the BM can only be decomposed by active MMPs.
- 306 A2. The reverse reaction decomposing the active MMP-ECM protein complex into the original enzyme
307 and substrate occur at fast rates, *i.e.* ECM degradation follows Michaelis-Menten kinetics.
- 308 A3. The ECM can be remodelled (*i.e.* produced) by healthy cells, provided space is available.
- 309 A4. MT1-MMPs, which are present on the cancer cell surfaces in monomeric form due to protein ex-
310 pression [16] and recycling of internalised MT1-MMPs [109], can activate proMMP-2 only when in
311 dimeric form.
- 312 A5. MT1-MMP dimerization, proMMP-2 activation and TIMPs-mediated MMP-2 inhibition occur ac-
313 cording to the biochemical reactions depicted in Figure 1.
- 314 A6. MMP and TIMP molecules decay over time (naturally and due to uptake/elimination by other cells).
- 315 A7. MT1-MMP and complexes involving MT1-MMP on the surface of cancer cells decay over time due
316 to the MT1-MMP internalization by tumour cells involved in the rapid turnover of this enzyme [55].
- 317 A8. SFs secrete both proMMP-2 and TIMPs, increasing the physiological levels of these molecules to
318 pathological levels.

319 A9. While MT1-MMPs and associated complexes are bound to the cell surfaces, soluble MMPs and
 320 TIMPs secreted by SFs are diffusive.

321 Note that the biochemical reactions summarized in Figure 1 allow us to capture the role TIMP-2 has in
 322 the proMMP-2 activation process and the fact that they may hinder the proteolytic action of MMP-2 in
 323 three possible ways [77]:

- 324 (i) by excessive binding to MT1-MMP, reducing the number of free MT1-MMP molecules available for
 325 proMMP-2 fission;
 326 (ii) by directly binding to proMMP-2, thus sequestering it from the activation complex;
 327 (iii) by directly binding to active MMP-2, blocking its proteolytic action.

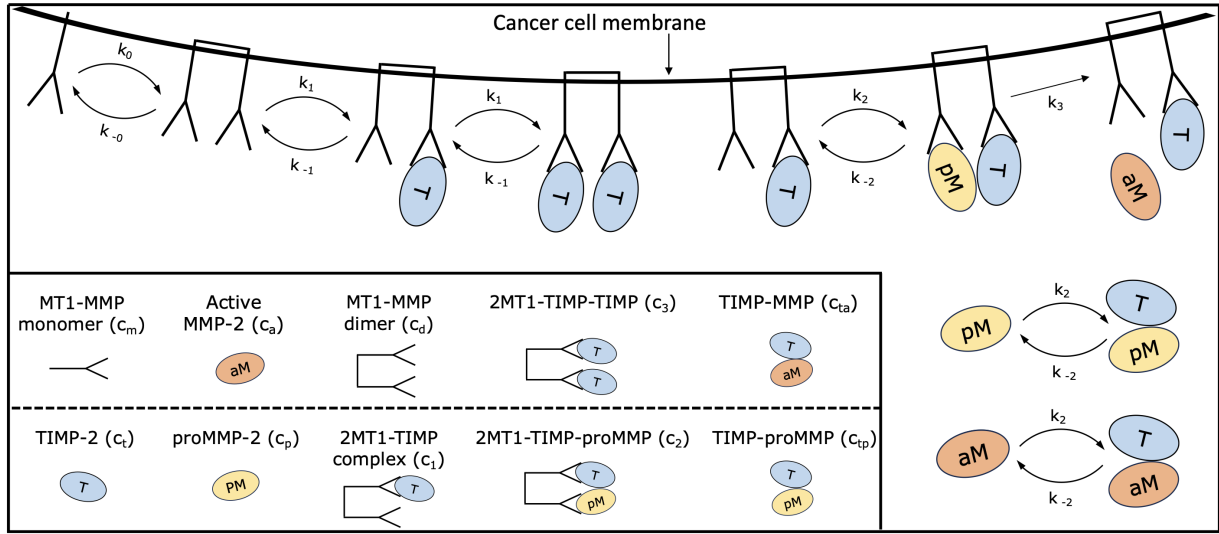


Figure 1: **Biochemical reactions included in the model.** Visual summary of biochemical reactions between MT1-MMP monomers, MT1-MMP dimers, proMMP-2s, TIMP-2s and active MMP-2s included in the model. MT1-MMPs, and all derived complexes, reside on the membrane of cancer cells, and may be subject to turnover (via expression and internalisation), a simplified version of which is included in our model. The association and dissociation rate k_i depend on specific integrin availability (e.g. beta 3 integrin is responsible for recruiting proMMP-2 [26]) and may *de facto* be subject to temporal fluctuations, but are assumed to be constant in our model for simplicity.

328 2.1.2 Model equations

329 Let $t \in \mathbb{R}_{\geq 0}$ denote time and $x = (x_1, x_2) \in \Omega$ denote the spatial position in the two-dimensional domain
 330 $\Omega \subset \mathbb{R}^2$, modelling a 2D cross-section of the CT. The boundary of the domain Ω is denoted $\partial\Omega$. Namely,
 331 we assume the domain to be the square $\Omega = [0, L] \times [0, L]$ and that the BM is located at the top boundary
 332 $\Gamma \equiv \{x = (x_1, L)\}$ with $x_1 \in [0, L]$, as illustrated in Figure 2.

333 In this article, we use the following units: seconds (s) for time, decimeter (dm) for space, and nanomolar
 334 (nM=nmol/dm³) for molecular concentrations and BM density. Moreover, we use the following notation
 335 (see also Figure 1):

- 336 • The density of tumor cells in a sufficiently close neighbourhood of the BM is denoted by ρ^0 (in
 337 number of cell/dm³) and is assumed to be constant for $t \in [0, T]$ where $T > 0$ is a finite time
 338 horizon.
- 339 • The density of ECM in the BM, *i.e.* at $x \in \Gamma$, is denoted by $M(x, t)$ (in nM);
- 340 • The concentration of MT1-MMPs in monomeric and dimeric form at $x \in \Gamma$ are denoted, respectively,
 341 by $c_m(x, t)$ and $c_d(x, t)$ (in nM).
- 342 • The concentration of unbound proMMP-2, TIMP-2 and active MMP-2 at $x \in \Gamma$ are denoted, re-
 343 spectively, by $c_p(x, t)$, $c_t(x, t)$ and $c_a(x, t)$ (in nM).

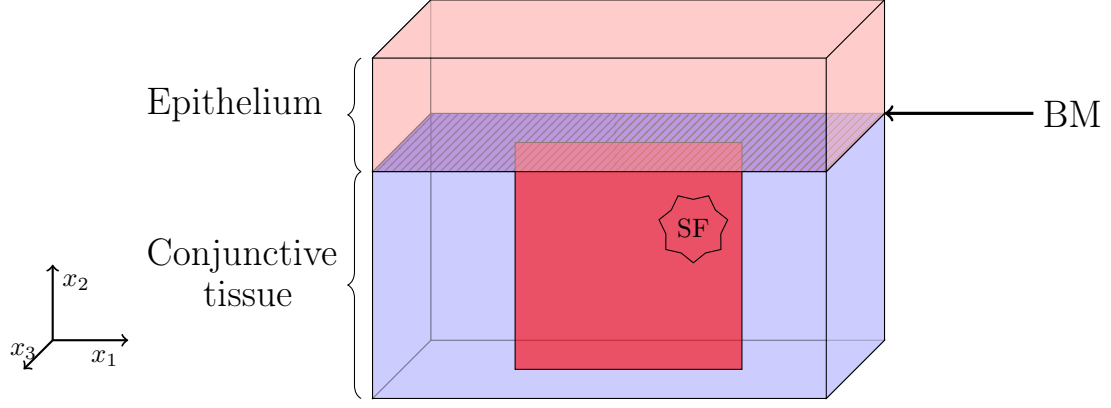


Figure 2: **Schematic illustration of the epithelium, CT, and the BM.** The red vertical plan represents our two-dimensional domain Ω that is a cross section of the CT. We also represented that the CT contains a SF (denoted by the star-shaped cell).

- 344 • The concentration of unbound soluble proMMP-2 and TIMP-2 secreted by SFs in the CT, *i.e.* $x \in \Omega$,
345 are denoted, respectively, by $\bar{c}_p(x, t)$ and $\bar{c}_t(x, t)$ (in nM).
- 346 • The concentration of the different MT1-MMP dimer ('2MT1') complexes observed at $x \in \Gamma$ during
347 MMP-2 activation by $c_i(x, t)$ with $i = 1, \dots, 3$, *i.e.* 2MT1-TIMP ($i = 1$), 2MT1-TIMP-proMMP
348 ($i = 2$) and 2MT1-TIMP-TIMP ($i = 3$) (in nM).
- 349 • The concentration of TIMP-bound proMMP-2 and MMP-2 at $x \in \Gamma$ are denoted, respectively, by
350 $c_{tp}(x, t)$ and $c_{ta}(x, t)$ (in nM).

351 Then, the model is given by the following ordinary differential equation system at $x \in \Gamma$ for $t \in (0, T)$

$$\frac{dM}{dt} = -\gamma c_a \frac{M}{K_m + M} + r_M \left(1 - \frac{M}{M_{\max}} \right)_+, \quad (2.1)$$

$$\frac{dc_m}{dt} = \alpha_m \rho^0 - k_0 c_m^2 + k_{-0} c_d - \beta_m c_m, \quad (2.2)$$

$$\frac{dc_d}{dt} = k_0 c_m^2 - k_{-0} c_d - k_1 c_d c_t + k_{-1} c_1 - \beta_d c_d, \quad (2.3)$$

$$\frac{dc_p}{dt} = I_p(t) - k_2 c_p (c_t + c_1) + k_{-2} (c_{tp} + c_2) - \beta_p c_p, \quad (2.4)$$

$$\frac{dc_t}{dt} = I_t(t) - c_t [k_1 (c_d + c_1) + k_2 (c_p + c_a)] + k_{-1} (c_1 + c_3) + k_{-2} (c_{tp} + c_{ta}) - \beta_t c_t, \quad (2.5)$$

$$\frac{dc_a}{dt} = k_3 c_2 - k_2 c_t c_a + k_{-2} c_{ta} - \beta_a c_a, \quad (2.6)$$

$$\frac{dc_1}{dt} = k_1 c_d c_t - c_1 [k_1 c_t + k_2 c_p] + k_{-1} (c_3 - c_1) + (k_{-2} + k_3) c_2 - \beta_1 c_1, \quad (2.7)$$

$$\frac{dc_2}{dt} = k_2 c_1 c_p - (k_{-2} + k_3) c_2 - \beta_2 c_2, \quad (2.8)$$

$$\frac{dc_3}{dt} = k_1 c_1 c_t - k_{-1} c_3 - \beta_3 c_3, \quad (2.9)$$

$$\frac{dc_{tp}}{dt} = k_2 c_t c_p - k_{-2} c_{tp} - \beta_{tp} c_{tp}, \quad (2.10)$$

$$\frac{dc_{ta}}{dt} = k_2 c_t c_a - k_{-2} c_{ta} - \beta_{ta} c_{ta}. \quad (2.11)$$

352 modelling the digestion of the ECM in the BM, coupled – though the terms $I_p(t)$ and $I_t(t)$ in (2.4) and (2.5),
 353 defined in (2.14), the initial conditions and boundary conditions (2.18)-(2.19) – with the following PDE
 354 system for $(x, t) \in \Omega \times (0, T)$,

$$\partial_t \bar{c}_p - \bar{D}_p \Delta \bar{c}_p = \bar{S}_p(x) - \beta_p \bar{c}_p, \quad (2.12)$$

$$\partial_t \bar{c}_t - \bar{D}_t \Delta \bar{c}_t = \bar{S}_t(x) - \beta_t \bar{c}_t, \quad (2.13)$$

355 modelling the spatio-temporal dynamics of the concentration fields of TIMP-2 and proMMP-2 in the CT.

356 **ECM degradation and remodeling in the BM.** The first term on the right-hand-side of equation
 357 (2.1) models the proteolytic degradation of ECM proteins by active MMP-2s (A1), modelled according
 358 to Michaelis-Menten kinetics (A2), with turnover number $\gamma > 0$ and Michaelis-Menten constant $K_m > 0$.
 359 Following the modelling strategy adopted in [29], the second term on the right-hand-side of equation (2.1)
 360 models ECM remodeling (A3), which occurs at a maximum rate $r_M > 0$ and only if space is available,
 361 where $M_{\max} > 0$ is the ECM density carrying capacity at the BM and where we have used the notation
 362 $(\cdot)_+ = \max(\cdot, 0)$.

363 **MMP-2 activation near the BM.** The first term on the right-hand-side of equation (2.2) models
 364 the expression of MT1-MMP in monomeric form on the surface of cancer cells (A4), occurring at a
 365 rate $\alpha_m > 0$. The terms highlighted in *teal* in equations (2.2)-(2.11) model the biochemical reactions
 366 summarised in Figure 1 (A5) according to the law of mass action, with reaction rates $k_i > 0$ ($i =$
 367 $0, -0, 1, -1, 2, -2, 3$). The last terms on the right-hand-side of equations (2.4)-(2.6), (2.10) and (2.11)
 368 model natural decay of $c_i(t, x)$ at a rate $\beta_i > 0$, for $i = \{p, t, a, tp, ta\}$ (A6). The last terms on the
 369 right-hand-side of equations (2.2)-(2.3) and (2.7)-(2.9) model internalization of MT1-MMP (A7) at rates
 370 $\beta_i > 0$, for $i = \{m, d, 1, 2, 3\}$ (assumed to be equal). Finally, the first terms on the right-hand-side
 371 of equations (2.4) and (2.5) model the inflow/outflow of proMMP-2 and TIMP-2 due to environmental
 372 sources (A8), and are given by

$$I_p(t) = \hat{\kappa}_p (\bar{c}_p|_{x=0} - c_p) \quad \text{and} \quad I_t(t) = \hat{\kappa}_t (\bar{c}_t|_{x=0} - c_t), \quad (2.14)$$

373 modelling the transmission of proMMP-2 and TIMP-2 from the CT to the BM at the right boundary Γ ,
 374 with transmission rates $\hat{\kappa}_i > 0$, as derived in the formal model reduction procedure inspired by [74] and
 375 detailed in Appendix A.

376 **SFs' secretome dynamics in the CT.** The second terms on the left-hand-side of equations (2.12)
 377 and (2.13) model diffusion of $\bar{c}_p(t, x)$ and $\bar{c}_t(t, x)$ at a rate $D_p > 0$ and $D_t > 0$, respectively (A9). The
 378 first terms on the right-hand-side of equations (2.12) and (2.13), *i.e.* $\bar{S}_p(x)$, $\bar{S}_t(x)$, respectively model the
 379 sources of proMMP-2 and TIMP-2 in the CT. They are of the form

$$\bar{S}_p(x) = s_p^{ph} + f_p(x) \quad \text{and} \quad \bar{S}_t(x) = s_t^{ph} + f_t(x), \quad (2.15)$$

380 where s_i^{ph} ($i = \{p, t\}$) is a constant source term modelling the physiological production of proMMP-2 and
 381 TIMP-2 by cells of the CT, and $f_i(x)$ ($i = \{p, t\}$) model the constant secretion of proMMP-2 and TIMP-2
 382 by SFs. In particular, we take

$$f_p(x) = \sum_{i=1}^N r_p \delta_{x_i, \sigma}(x) \quad \text{and} \quad f_t(x) = \sum_{i=1}^N r_t \delta_{x_i, \sigma}(x)$$

383 where we model proMMP-2 and TIMP-2 production at maximum rates $r_p > 0$ and $r_t > 0$, respectively,
 384 as sharp gaussians centered at the positions $x_i \in \Omega$ ($i = 1, \dots, N$) of the N SFs present in the domain,
 385 *i.e.* we define

$$\delta_{x_i, \sigma}(x) := \frac{1}{\sqrt{2\pi}\sigma^2} \exp\left(-\frac{(x - x_i)^2}{2\sigma^2}\right), \quad (2.16)$$

386 for some small variance $0 < \sigma^2 \ll 1$ (we take $\sigma^2 = 0.04 \text{ dm}^2$). Finally, as in equations (2.4) and (2.5), the
 387 last terms in (2.12) and (2.13) model natural decay (A6).

388 **Boundary conditions.** We assume that soluble proMMPs and TIMPs produced by SFs cannot cross
 389 the boundaries of the domain, and complement equations (2.12) and (2.13) with the Neumann boundary
 390 conditions

$$\bar{D}_p \nabla \bar{c}_p \cdot \nu = \bar{D}_t \nabla \bar{c}_t \cdot \nu = 0 \quad \text{on } \partial\Omega \setminus \Gamma \times (0, T), \quad (2.17)$$

391 with ν the outward normal vector to the boundary $\partial\Omega$. While *in vivo* these soluble molecules may
 392 escape the tissue through epithelial membranes, the physical walls of experimental devices justify this
 393 assumption *in vitro*. The transmission of proMMP-2 and TIMP-2 from the CT to the BM is captured by
 394 Robin boundary conditions at Γ , as derived in the model reduction procedure detailed in Appendix A,
 395 *i.e.* equations (2.12) and (2.13) are also complemented with (which are compatible with (2.14))

$$-\bar{D}_p \nabla \bar{c}_p \cdot \nu = \kappa_p (\bar{c}_p - c_p), \quad \text{on } \Gamma \times (0, T), \quad (2.18)$$

$$-\bar{D}_t \nabla \bar{c}_t \cdot \nu = \kappa_t (\bar{c}_t - c_t), \quad \text{on } \Gamma \times (0, T), \quad (2.19)$$

396 where $\kappa_p > 0$ and $\kappa_t > 0$ describe the diffusive permeability of proMMP-2 and TIMP-2, respectively, in
 397 the BM. While these molecules can cross the BM, we assume that they will immediately interact with
 398 cancer cells in the close proximity of the BM. Such dynamics can be adequately captured by the chosen
 399 boundary conditions at Γ .

400 **Initial conditions.** We consider the initial conditions to reflect the scenario in which no ECM degra-
 401 dation, biochemical reaction, or secretion by SFs has taken place. Thus, for simplicity, we consider the
 402 initial ECM density to be at carrying capacity, *i.e.*

$$M(x, 0) = M_{\max} \quad \text{on } \Gamma. \quad (2.20)$$

403 All other soluble molecules, in the CT and at the BM, are taken to be at physiological levels at day 0, *i.e.*

$$c_i(x, 0) = c_i^{\text{ph}} \quad \text{for } i = \{m, d, a, 1, 2, 3, tp, ta\} \quad \text{on } \Gamma, \quad (2.21)$$

$$c_p(x, 0) = c_p^{\text{ph}} \quad \text{and} \quad c_t(x, 0) = c_t^{\text{ph}} \quad \text{on } \Gamma, \quad (2.22)$$

$$\bar{c}_p(x, 0) = \bar{c}_p^{\text{ph}} \quad \text{and} \quad \bar{c}_t(x, 0) = \bar{c}_t^{\text{ph}} \quad a.e. \text{ in } \bar{\Omega}. \quad (2.23)$$

404 2.2 Parameter values

405 The baseline values used for the model parameters are summarized in Table 1. We combine results
 406 from experiments and computational works to characterize the maximum number of parameters from
 407 the existing literature (see Reference publications in Table 1). Some parameters are estimated here,
 408 consistently with our model equations (marked with a * next to the Reference publications in Table 1).
 409 In particular:

- 410 • the BM carrying capacity is estimated from empirical measurements of collagen IV, the main com-
 411 ponent of the BM, and its molecular weight;
- 412 • internalisation rates of MT1-MMP dimers and complexes are assumed to be the same as those of
 413 MT1-MMP monomers;
- 414 • decay rates of proMMP-2, TIMP-2 and MMP-2 are computed from half-life values, those of TIMP-
 415 2/proMMP-2 and TIMP-2/MMP-2 complexes are estimated from physiological levels assuming they
 416 correspond to equilibrium concentrations;
- 417 • physiological production rates of proMMP-2 and TIMP-2 are estimated from physiological levels
 418 assuming they correspond to equilibrium concentrations;
- 419 • physiological levels of MT1-MMPs, proMMP-2, TIMP-2, MMP-2 and TIMP-2/MMP-2 complex are
 420 estimated from empirical measurements of serum levels of these proteins and their molecular weight;
- 421 • values of the diffusive permeability and transmission rates of proMMP-2 and TIMP-2 in the BM are
 422 estimated consistently with the physical considerations and definitions introduced in the formal BM
 423 dimension reduction procedure, detailed in appendix A.

424 Details about the references used and the computations made to obtain the above-listed parameter values
 425 can be found in Appendix B.

426 **Remark 1.** *It is worth mentioning that we use measurements in blood and transpose the values to tissue*
 427 *concentrations. This may be untrue and most probably the values depend on the tissue. However, as we*
 428 *were unable to find measurement in tissue samples, we use these values in this work. This can easily be*
 429 *updated whenever better data is available.*

Parameter	Biological meaning	Value & Unit	Reference
γ	Maximum ECM degradation rate	0.236 s ⁻¹	[61]
K_m	Michaelis-Menten constant of ECM proteolytic degradation	0.1357 nM	[61]
r_M	Maximum ECM remodeling rate	6.18 × 10 ⁻⁴ nM/s	[61]
M_{\max}	ECM carrying capacity	62.5 × 10 ³ nM	* [2]
α_m	Production rate of monomeric MT1-MMP by cancer cells	5 × 10 ⁻⁴ nmol/s/cell	[17]
ρ^0	Number of tumor cells adjacent to the BM	1 × 10 ² cells/dm ²	*
k_0	Maximum MT1-MMP dimerization rate	2 1/nM/s	[55]
k_{-0}	Dissociation rate of MT1-MMP dimers	1 × 10 ⁻² s ⁻¹	[55]
k_1	Association rate of TIMP-2 and MT1-MMP	2.71 1/nM/s	[105]
k_{-1}	Dissociation rate of bound MT1-MMP and TIMP-2	1 × 10 ⁻⁴ s ⁻¹	[105]
k_2	Association rate of proMMP-2 and TIMP-2	0.14 1/nM/s	[86]
k_{-2}	Dissociation rate of bound proMMP-2 and TIMP-2	1 × 10 ⁻⁴ s ⁻¹	[86]
k_3	MMP-2 activation rate	0.02 s ⁻¹	[62]
β_m	MT1-MMP monomer internalization rate	3.85 × 10 ⁻²	[55]
β_d	MT1-MMP dimer internalization rate	3.85 × 10 ⁻²	* [55]
$\beta_1, \beta_2, \beta_3$	Internalization rate of MT1-MMP complexes	3.85 × 10 ⁻²	* [55]
β_p	Decay rate of proMMP-2	6.08 × 10 ⁻⁴ s ⁻¹	* [83]
β_t	Decay rate of TIMP-2	4.45 × 10 ⁻⁵ s ⁻¹	* [15]
β_a	Decay rate of active MMP-2	1.22 × 10 ⁻³ s ⁻¹	* [83]
β_{tp}	Decay rate of TIMP-2/proMMP-2 complex	3.60 s ⁻¹	*
β_{ta}	Decay rate of TIMP-2/MMP-2 complex	0.035 s ⁻¹	*
D_p, D_t	Diffusion coefficients of proMMP-2, TIMP-2	1.29 × 10 ⁻⁶ dm ² /s	[17, 22]
s_p^{ph}	Physiological production rate of proMMP-2	1.09 × 10 ⁻² nM/s	* [90, 83]
s_t^{ph}	Physiological production rate of TIMP-2	4.28 × 10 ⁻⁴ nM/s	* [15, 90]
r_p	Production rate of proMMP-2 by senescent fibroblasts	8.34 × 10 ⁻⁴ nM/s	*
r_t	Production rate of TIMP-2 by senescent fibroblasts	2.22 × 10 ⁻⁶ nM/s	*
κ_p, κ_t	Diffusive permeability of proMMP-2 and TIMP-2 in the BM	1.935 × 10 ⁻⁶ dm/s	* [17, 22, 96]
$\hat{\kappa}_p, \hat{\kappa}_t$	Transmission rate of proMMP-2 and TIMP-2 across the BM	0.9675 s ⁻¹	* [17, 22, 96]
c_m^{ph}	Physiological levels of monomeric MT1-MMP	0.14 nM	* [73]
c_d^{ph}	Physiological levels of dimeric MT1-MMP	0.14 nM	* [20]
c_p^{ph}	Physiological levels of proMMP-2	18 nM	* [90, 101]
c_t^{ph}	Physiological levels of TIMP-2	9.6 nM	* [90, 102]
c_a^{ph}	Physiological levels of active MMP-2	0.44 nM	* [90, 101]
c_{ta}^{ph}	Physiological levels of TIMP-2/MMP-2 complex	17 nM	* [90]
c_{tp}^{ph}	Physiological levels of TIMP-2/proMMP-2 complex	6.72 nM	* [4]
$c_1^{\text{ph}}, c_2^{\text{ph}}, c_3^{\text{ph}}$	Physiological levels of MMP-2 activation complexes	0 nM	*

Table 1: List of parameters found in equations and initial conditions (2.1)-(2.23) and baseline parameter values used in this paper, drawn from the literature. Parameters which are not explicitly found in the literature and were calculated here are marked with a * in the last column. Details about the calculations used to estimate parameters from the referenced papers can be found in Appendix B.

430 Few parameters lack empirical measurements or estimates in the literature (marked with only a * in
431 the last column of Table 1). For simplicity, we set the physiological levels of the remaining molecular
432 complexes to zero. Relevant parameter values for the tumor cell density in contact with BM and the
433 production rates of proMMP-2 and TIMP-2 by SFs are found using numerical testing. In particular,
434 baseline values of TIMP-2 and proMMP-2 production rates by SFs are chosen to add 1% and 200%,
435 respectively, to the respective physiological production rate at the SF location.

436 2.3 Reduced system from simplifying assumptions

437 To improve analytical and computational tractability, in view of future work comprising model calibration
438 with experimental data and model extensions, we derived a reduced system under simplifying assumptions.

439 In summary, we assume the inhibitory action of TIMP-2 is irreversible, that the evolution of the
440 complexes' concentrations c_1, c_2, c_3 and MT1-MMP turnover are very fast compared to other dynamics in
441 the system, and that natural decay in the BM is negligible in the timescale considered (cf. SA1-SA4 in

442 Appendix C). In the reduced, simplified model we have that $\forall x \in \Gamma$ and $t \in (0, T)$

$$\frac{dM}{dt} = -\gamma c_a \frac{M}{K_M + M} + r_M \left(1 - \frac{M}{M_{\max}}\right), \quad (2.24)$$

$$\frac{dc_t}{dt} = \hat{\kappa}_t \bar{c}_t - k_2 c_t (c_p + c_a) - \hat{\kappa}_t c_t, \quad (2.25)$$

$$\frac{dc_p}{dt} = \hat{\kappa}_p \bar{c}_p - k_2 c_p c_t \left(1 + \frac{k_1 k_3}{k_{-1}(k_{-2} + k_3)} \bar{c}_d\right) - \hat{\kappa}_p c_p, \quad (2.26)$$

$$\frac{dc_a}{dt} = \frac{k_1 k_2 k_3}{k_{-1}(k_{-2} + k_3)} \bar{c}_d c_t c_p - k_2 c_t c_a, \quad (2.27)$$

443 in which \bar{c}_d is a given parameter representing the constant concentration of available dimeric MT1-MMP
 444 and $\bar{c}_i \equiv \bar{c}_i(x, t)|_{\Gamma}$ ($i = \{t, p\}$), *i.e.* the concentrations of TIMP-2 and proMMP-2 at the BM coming from
 445 the CT. System (2.24)–(2.27) is coupled to System (2.12)–(2.13).

446 **Equilibrium concentrations.** We analysed the steady state of the reduced system (2.25)–(2.27), cf.
 447 Appendix C.1.1. The corresponding equilibrium concentrations are plotted in Figure 3 for varying values of
 448 the concentrations of TIMP-2 and proMMP-2 reaching the BM from the CT. We see that the equilibrium
 449 concentration of active MMP-2: increases (linearly) with the amount of proMMP-2 coming from the CT;
 450 (linearly) decreases with the amount of TIMP-2 coming from the CT; is zero in the absence of TIMP-2
 451 coming from the CT; increases with the amount of MT1-MMP dimers (cf. Supplementary Figure S1).
 452 These results are consistent with the dual role of TIMP-2 in MMP-2 activation.

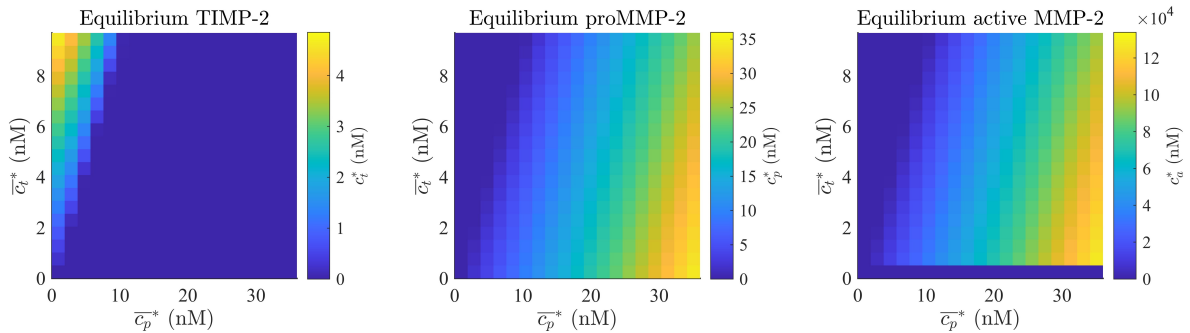


Figure 3: **The analytical equilibrium of the reduced system demonstrates that the dual role of TIMP-2, as activator and inhibitor of MMP-2, is still captured in the reduced model.** Concentration of TIMP-2 (left), proMMP-1 (center) and active MMP-2 (right) at steady state of the reduced ODE system (2.25)–(2.27), for varying fixed concentrations of proMMP-2 (\bar{c}_p^*) and TIMP-2 (\bar{c}_t^*) coming from the CT. The steady state is given by (C.3) for $\bar{c}_t^* > 0$, and by (C.4) otherwise, under the parameter values listed in Table 1 and $C_a = 0$. The latter corresponds to the value obtained at equilibrium under initial conditions $c_t = c_p = c_a = 0$ at $t = 0$. We consider TIMP-2 and proMMP-2 concentrations from the CT in the ranges $\bar{c}_t^* \in [0, c_t^{\text{ph}} + 1\%c_t^{\text{ph}}]$ and $\bar{c}_p^* \in [0, c_p^{\text{ph}} + 200\%c_p^{\text{ph}}]$, in line with the parameter choices reported in Section 2.2.

453 **BM rupture and cancer invasion.** We define BM rupture as the decrease of the BM density below
 454 an arbitrary value that corresponds to the critical density below which tumor cells can invade. We
 455 derived a condition for this long-term sustained BM rupture, allowing cells to begin invading the CT,
 456 cf. Appendix C.1.2. From this condition, we have that BM rupture and cancer invasion is more likely
 457 to occur for: higher values of active MMP-2 at equilibrium, which depends on the amount of proMMP-
 458 2 and TIMP-2 coming from the CT and MT1-MMP2 dimers; higher BM degradation rates; lower BM
 459 remodeling rates. These results are consistent with the biological meaning of these quantities.

460 2.4 Numerical method and set up

461 To test the model's ability to predict biologically relevant scenarios, we conduct numerical simulations
 462 of the full System (2.1)–(2.13), complemented with definitions (2.14)–(2.16), boundary conditions (2.17)–
 463 (2.19), and initial conditions (2.20)–(2.23), under the baseline parameter values stated in Table 1. The

464 results are discussed in Section 3.1, while section 3.2 is dedicated to a global sensitivity analysis of both
 465 the full and reduced models, using the SAFE (Sensitivity analysis For Everyone) toolbox [92].

466 In Section 3.1 we set $\dim(\Omega) = 2$ and $\dim(\Gamma) = 1$ (“2D” case), while in Section 3.2 we set $\dim(\Omega) = 1$
 467 and $\dim(\Gamma) = 0$ (“1D” case). In particular, in 2D we assume that the domain $\Omega = [0, L] \times [0, L]$ is a
 468 square of side length L dm (or, in 1D, a line of length L dm). We consider a uniform discretization of the
 469 domain Ω using $N_x \times N_x$ nodes (or, in 1D, using N_x nodes), and using N_x nodes for Γ . We construct a
 470 cell-centered finite volume spatial discretization of our system and integrate it in time using an explicit
 471 Runge-Kutta integration method, up to a final time T . For details about our numerical scheme, we refer
 472 to Appendix D, and the values of T , L and N_x used are reported in Table 2.

Parameter	Meaning	Unit	Value S.3.1	Value S.3.2
$\dim(\Omega)$	Dimension of the CT		2	1
T	End time	days	7	1
L	Length in each dimension of Ω	dm	0.1	0.1
N_x	Number of nodes in the x_i direction		50	20

Table 2: Simulation parameters used in Section 3.1 and Section 3.2.

473 Our code (with scripts to replicate the figures of this article) can be downloaded from Zenodo <https://doi.org/10.5281/zenodo.12654067> or from GitHub <https://github.com/alexandre-poulain/TumInvasion-BM>.
 474
 475

476 3 Results

477 3.1 Model’s ability to reproduce biologically relevant scenarios

478 3.1.1 Biologically relevant test cases

479 To test the model’s ability to reproduce biologically relevant scenarios, we consider three test cases:

- 480 • *Healthy test case:* we consider a healthy tissue, free from any tumor cells, *i.e.* $\rho_0 = 0$, and assume
 481 that there are no SFs in the CT.
- 482 • *Tumor test case:* we assume that a tumor is present, but no SFs, and the tumor cell density in
 483 contact with the BM is given by $\rho_0 = 10^3 \chi_{[L/4, 3L/4]}$.
- 484 • *Tumor with a senescent fibroblast test case:* we assume a tumour is present, and again consider
 485 $\rho_0 = 10^3 \chi_{[L/4, 3L/4]}$, as well as a SF in the CT at a position (x_1^{SF}, x_2^{SF}) .

486 3.1.2 Results of the full model under the baseline parameter set

487 The BM density at day 7 predicted by the model for each test case is displayed in Figure 4 (left), where we
 488 also mark the critical BM density for BM rupture (assumed to be $M_{\text{crit}} = M_{\text{max}}/2$), and the corresponding
 489 concentration of TIMP-2 and proMMP-2 in the CT at day 7 is displayed in Figure 5. We also show the
 490 time evolution of the BM density in Figure 4 (right), which is still evolving at day 7 in the presence of a
 491 tumour – in fact, its dynamics span several weeks (cf. Supplementary Figure S2). This is not the case for
 492 the remaining molecular concentrations in our system, which have all reached a steady state by day 7 –
 493 in fact, their dynamics only span several hours (cf. Supplementary Figures S3-S5).

494 **Healthy test case.** In the healthy test case we observe no BM degradation, as displayed in Figure 4
 495 (green line), and as expected in a healthy epithelial tissue. As we assumed no tumor cells are present in a
 496 healthy tissue, there is no production of monomeric MT1-MMP and consequently no MMP-2 activation:
 497 even though their initial concentrations were positive, they becomes zero exponentially fast (cf. Supple-
 498 mentary Figure S3) due to internalisation and natural decay. Interestingly, we notice that a gradient of
 499 TIMP-2 and proMMP-2 in the CT forms in the x_2 direction, *i.e.* orthogonally to the BM, as displayed in
 500 Figure 5 (first column). This is due to the transmission conditions at the BM and the reactions occurring
 501 at this location, which result in an increase in TIMP-bound proMMPs (cf. Supplementary Figure S3).

502 **Tumor test case.** In the tumour test case we observe partial degradation of the BM in the region
 503 where the tumour is present, as displayed in Figure 4 (blue line). This localized degradation of the BM
 504 in the tumor region is explained by the localization of MT1-MMP produced by tumor cells, which ensure

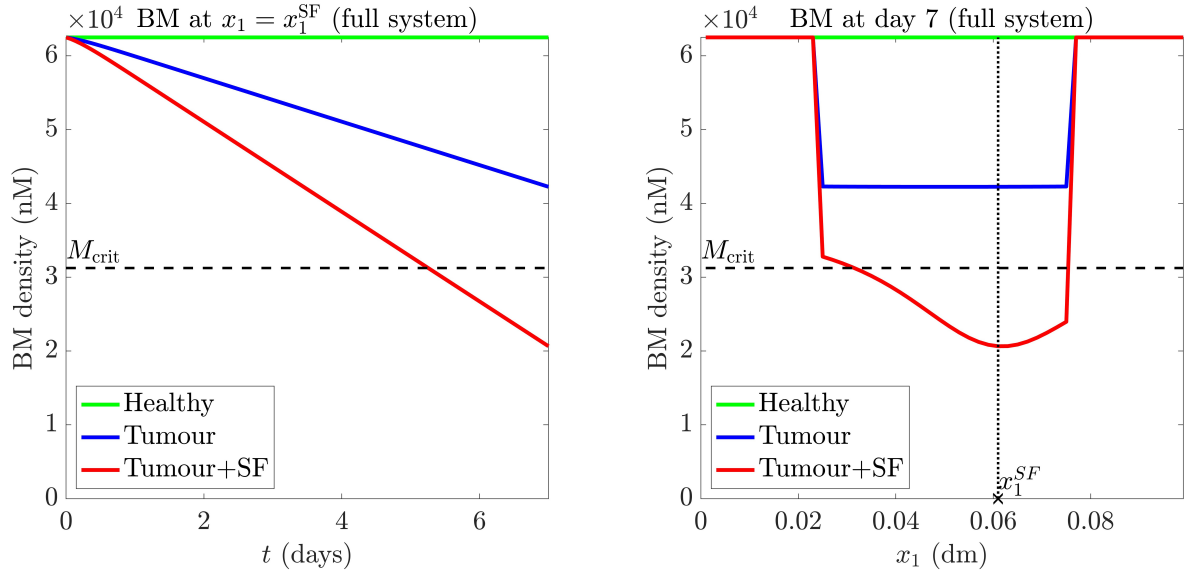


Figure 4: **The model predicts that the presence of a SF speeds up BM digestion, with the fastest digestion rate occurring at the point closest to the SF.** BM density predicted by the full model for the healthy (green), tumour (blue) and tumour+SF (red) test cases. The BM density $M(t, x)$ is plotted over time (up to day 7) at $x_1 = x_1^{SF}$, *i.e.* at the point in the BM closest to the SF, on the left. On the right we plot the spatial distribution of the BM density at day 7, marking the position $x_1 = x_1^{SF}$ closest to the SF with a dotted line. The dashed horizontal line marks the critical BM density M_{crit} below which we expect cells to be able to invade BM. These results are obtained solving System (2.1)–(2.13), under definitions (2.14)–(2.16), boundary conditions (2.17)–(2.19), and initial conditions (2.20)–(2.23), under the parameter values in Table 1 or as specified in Section 3.1.1 for each test case.

505 positive levels of active MMP-2 persist locally (cf. Supplementary Figure S3). This supported by the
 506 experimental results of [81], in which we observe a localized activation of proMMP-2 close to the BM.
 507 Nonetheless, the resulting levels of active MMP-2 do not suffice to predict cancer invasion within one week
 508 – this will happen as time advances (cf. Supplementary Figure S2). On the other hand, we observe in
 509 Figure 5 (second column) a gradient of TIMP-2 and proMMP-2 concentrations in the CT analogous to
 510 that observed in the healthy test case, with slightly lower levels of TIMP-2 recorded in the CT at day 7.
 511 This is likely due to the recruitment of these molecules in the MMP-2 activation cascade, as demonstrated
 512 by the increase in the levels of molecular complexes (cf. Supplementary Figure S3, bottom row).

513 **Tumour with a SF test case.** With the addition of a SF close to the BM – specifically, at a distance
 514 of 0.5 mm in Figures 4 and 5 – we instead observe BM rupture within 5 days, as displayed in Figure 4 (red
 515 line). This is due to the the large amount of proMMP-2 secreted by the SF that reached the BM in the
 516 tumour region, creating a larger imbalance between activation and inhibition compared to the tumor test
 517 case, resulting in a larger amount of active MMP-2 (cf. Supplementary Figure S5) and ultimately faster
 518 BM digestion. Interestingly, the digestion of the BM is asymmetric in space, with the fastest digestion
 519 rate occurring at $x_1 = x_1^{SF}$, *i.e.* in correspondence of the SF position, at which point we expect complete
 520 BM digestion shortly after 10 days (cf. Supplementary Figure S2). This is due to the radial diffusion of
 521 the SF secretome from the SF position in the CT, as displayed in Figure 5 (bottom right plot), which
 522 creates spatial heterogeneity in the enzymes concentration fields in the BM mirroring the pattern observed
 523 in the BM, with the largest amount of proMMP-2 in the BM occurring at the point closest to the BM (cf.
 524 Supplementary Figure S5), *i.e.* at $x_1 = x_1^{SF}$ in our geometric setting. The spatial pattern of proMMP-2
 525 in the CT is not observed for TIMP-2 in Figure 5 (top right plot) only because production of TIMP-2 by
 526 the SF is assumed to be small, and thus the effect of the SF on this concentration field appears negligible.

527 3.1.3 Further exploring the role of SF location and secretion rates

528 Under the baseline parameter set it is clear that the presence of a SF close to the BM may significantly
 529 speed up BM digestion and, consequently, cancer invasion due to their secretome. We recall that, due to
 530 a lack of empirical measurements, the secretion rates of TIMP-2 and proMMP-2 by SFs were arbitrarily

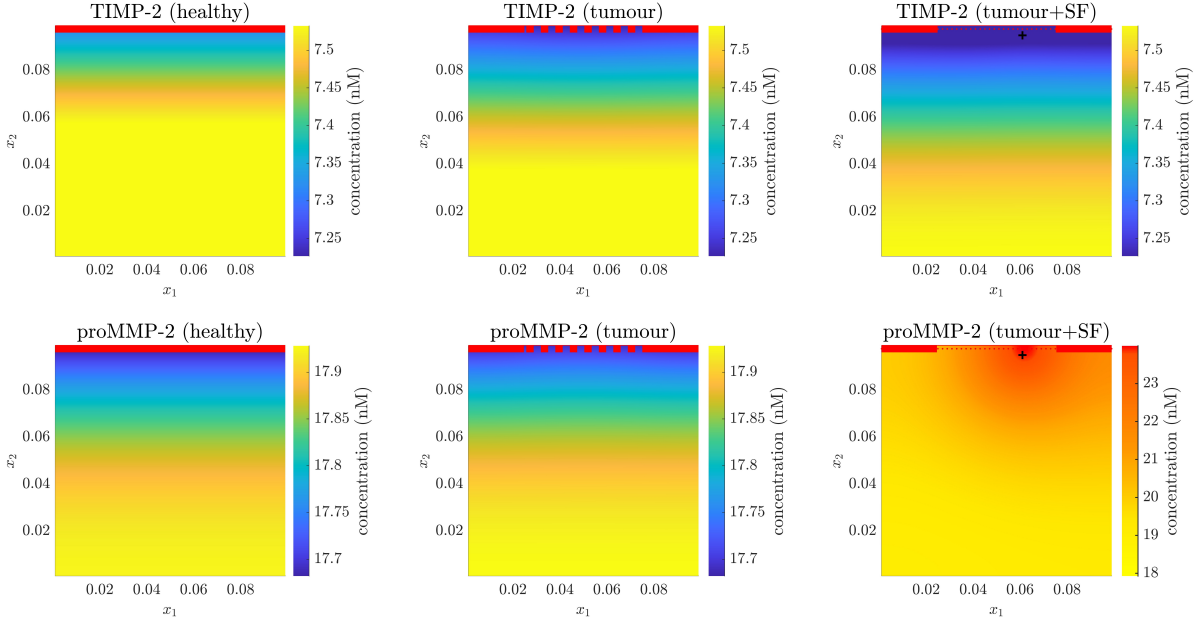


Figure 5: **The inclusion of a SF in the model results in the prediction of accurate gradients of proMMP-2 in the CT, and faster digestion of the BM.** TIMP-2 (top) and proMMP-2 (bottom) concentrations in the CT at day 7 predicted by the full model for the healthy (left), tumour (center) and tumour+SF (right) test cases. On the right plots, the cross marks the position of the SF in the CT, *i.e.* the center of diffusion of SF secretome. The BM is marked in red at $x_2 = L$ along with its status at day 7: intact (solid line), partially degraded (dashed) or ruptured (dotted), *i.e.* degraded below a critical value, cf. Figure 4 (left). These results are obtained solving System (2.1)–(2.13), under definitions (2.14)–(2.16), boundary conditions (2.17)–(2.19), and initial conditions (2.20)–(2.23), under the parameter values in Table 1 or as specified in Section 3.1.1 for each test case.

531 set in the baseline scenario. We thus explored how the BM density at $x_1 = x_1^{SF}$, *i.e.* the point at the
532 BM most affected by SF secretome, varying the distance of the SF from the BM, and its TIMP-2 and
533 proMMP-2 secretion rates, as displayed in Figure 6. We observe that higher secretion rates of proMMP-2
534 and lower secretion rates of TIMP-2 by SFs result in a lower BM density at day 7 and thus higher change
535 of observing BM rupture within a week. This is in line with the results of the steady state analysis of the
536 reduced system and the equilibrium concentration of active MMP-2 shown in Figure 3. However, if the
537 SF does not secrete any TIMP-2, BM degradation may still occur, suggesting that physiological levels of
538 TIMP-2 in the CT suffice to initiate the MMP-2 activation cascade, and any TIMP-2 produced by SF will
539 likely play a saturating role. Finally, it is clear from Figure 6 that decreasing the distance of the SF from
540 the BM increases its influence on BM dynamics, and BM rupture may be observed at day 7 for a wider
541 range of TIMP-2 and proMMP-2 secretion rates. We expect that increasing the proportion of SFs in the
542 CT close to the BM would lead analogous results.

543 3.2 Global sensitivity analysis of the full and reduced models

544 3.2.1 Description of the global sensitivity analysis method

545 Global sensitivity analysis (GSA) is a powerful tool to study how the uncertainty in the model's outputs
546 depends on the uncertainties of the inputs. To better understand the relative importance of the parameters
547 of the model and identify key ones, we conduct GSA using the SAFE toolbox [92, 91] for Matlab. In
548 particular, we employ the Elementary Effects (EEs) Test included in the toolbox, encoding a revised
549 version of the Morris method [84]. This GSA method is based on the calculation of the EEs associated
550 with each model input (parameter values, in our case), and revised versions of the Morris method consider
551 the absolute value of EEs to avoid potential cancellation effects in the summation of EEs with opposite
552 signs. In particular:

- 553 • a large mean of the absolute value of the EEs indicates the parameter has individual important effect
554 and, *viceversa*, a small mean indicates the parameter has a negligible effect on the output;

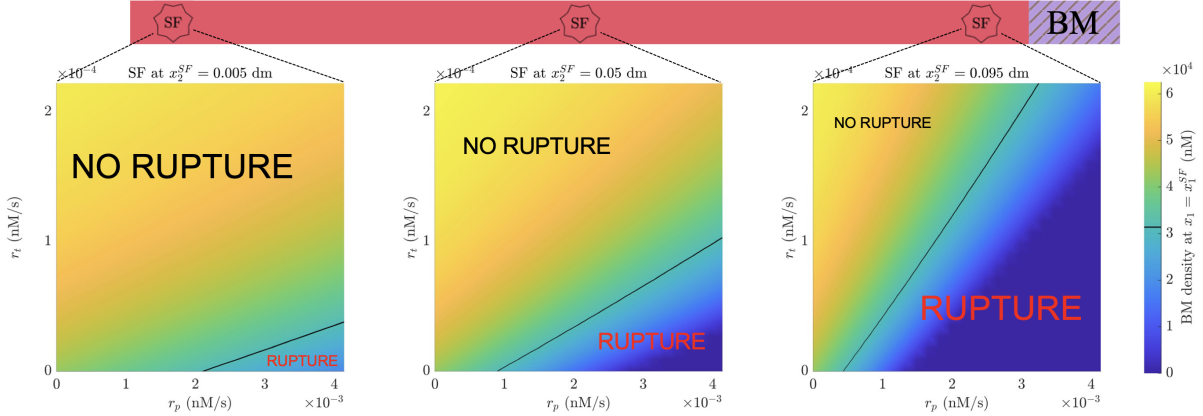


Figure 6: **The model predicts that the presence of a SF in the CT can induce BM rupture according to a delicate balance between its distance from the BM and the rates at which it secretes proMMP-2 and TIMP-2.** BM density at the point closest to the SF (*i.e.* at $x_1 = x_1^{SF}$) predicted by the full model for the tumour+SF test case, varying the distance between the SF and the BM. In particular, we consider a SF located at $x_2^{SF} = 0.005$ dm (left), at $x_2^{SF} = 0.05$ dm (center) and at $x_2^{SF} = 0.095$ dm (right), recalling that the BM is located at $x_2 = 0.1$ dm. In each plot, the BM density predicted by the model at day 7 is shown for varying values of the proMMP-2 secretion rate $r_p \in [0, 4.17 \times 10^{-3}]$ s⁻¹ and the TIMP-2 secretion rate $r_t \in [0, 2.22 \times 10^{-4}]$ s⁻¹ by the SF. The black line marks the critical BM density M_{crit} below which ECM pore size are sufficiently large for cancer cells to pass through, here referred to as BM rupture. Following this criterion, the regions of the parameter space in which the model predicts “RUPTURE” or “NO RUPTURE” by day 7 are marked on each plot. These results are obtained solving System (2.1)–(2.13), under definitions (2.14)–(2.16), boundary conditions (2.17)–(2.19), and initial conditions (2.20)–(2.23), under the parameter values in Table 1 or as specified in Section 3.1.1 for the Tumour+SF test case.

- a large standard deviation of the absolute value of the EEs indicates the parameter has a non-linear effect or one dependent on its interaction with other parameters.

The EE Test is the least computationally expensive GSA method, and it is therefore particularly suited for screening and ranking of model inputs in more involved mathematical models, like the one presented here. For an overview of GSA methods, we refer the interested reader to the review article [58].

As GSA methods need to run a lot of simulations of the model, we restrict our analysis to the one dimensional case, *i.e.* $\dim(\Omega) = 1$ and $\dim(\Gamma) = 0$. As the addition of a SF in the CT can particularly speed up BM digestion, as seen in Section 3.1, we set up our GSA to target variations of the BM density M . To capture variations in the time evolution of this quantity, we consider $N_t = 100$ equally spaced time points t_j ($j = 1, \dots, 100$) at which we save the BM density $M(t_j)$, and compute

$$Y = \Delta t \sum_{j=1}^{N_t} \frac{|M(t_j)|}{|M^0|}, \quad (3.1)$$

where $\Delta t = T/N_t$ is the spacing between two saved time points. From now on, the quantity Y will be referred to as the output of our simulations. The spatio-temporal parameters used in each model simulation (*i.e.* T, L, N_x) for the GSA are specified in Table 2 (last column). The parameter sets considered as inputs during the GSA are specified in following sections for the full and reduced model, respectively. For each parameters set, the GSA relies on 500 points sampled from the parameter space using the Latin Hypercube technique with a radial sampling method. The parameter space is defined considering each parameter has a uniform probability distribution in a range chosen to span several orders of magnitude both below and above that of the baseline parameter value. These ranges are specified in Table 3 for the parameters of the full model, and for \bar{c}_d we consider values in the range $[10^{-7}, 10^{-3}]$.

3.2.2 Sensitivity analysis of the full model

We perform GSA on the full model (2.1)–(2.13), by analysing separately two parameters sets:

Parameter	Lower bound	Upper bound	Parameter	Lower bound	Upper bound
k_0	0.02	200	γ	2.36×10^{-3}	23.6
k_{-0}	1×10^{-4}	1	K_M	1.357×10^{-3}	13.57
k_1	0.0271	271	r_M	6.18×10^{-6}	6.18×10^{-2}
k_{-1}	1×10^{-6}	0.01	ρ_0	10	10000
k_2	0.0014	14	α_m	5×10^{-6}	0.05
k_{-2}	1×10^{-6}	0.01	D_t	1.29×10^{-8}	1.29×10^{-4}
k_3	2×10^{-4}	2	D_p	1.29×10^{-8}	1.29×10^{-4}
β_t	4.45×10^{-7}	4.45×10^{-3}	κ_t	1.935×10^{-8}	1.935×10^{-4}
β_p	6.08×10^{-6}	6.08×10^{-2}	κ_p	1.935×10^{-8}	1.935×10^{-4}
β_a	1.29×10^{-8}	1.29×10^{-4}	s_t^{ph}	4.272×10^{-6}	4.272×10^{-2}
β_m	3.85×10^{-4}	3.85	s_p^{ph}	1.0944×10^{-4}	1.0944
β_d	3.85×10^{-4}	3.85	r_t	2.22×10^{-8}	2.22×10^{-4}
β_{tp}	0.036	360	r_p	8.28×10^{-6}	8.28×10^{-2}
β_{ta}	3.5×10^{-4}	3.5	x_1^{SF}	0	0.1

Table 3: Lower and upper bounds of the parameter values considered in the GSA of the full model, sorted in parameter Set 1 (left) and Set 2 (right). The unit of measurement of each parameter is given in Table 1.

576 *Set 1:* The biochemical reaction coefficients ($k_0, k_{-0}, k_1, k_{-1}, k_2, k_{-2}, k_3$) and the molecular decay coeffi-
577 cients ($\beta_t, \beta_p, \beta_a, \beta_m, \beta_d, \beta_{tp}, \beta_{ta}$);

578 *Set 2:* The parameters related to the BM degradation and production (γ, K_M, r_M), the cancer cells and
579 their MT1-MMP expression (ρ_0, α_m), the production and diffusion of TIMP-2 and proMMP-2 in
580 CT ($s_t^{\text{ph}}, s_p^{\text{ph}}, r_t, r_p, D_p, D_t$) and their transmission to the BM (κ_t, κ_p), the position of the SF (x_1^{SF}).

581 **Remark 2.** We emphasize that variations of the parameter β_d affect Equation (2.3) and Equations (2.7)–
582 (2.9) as $\beta_d = \beta_1 = \beta_2 = \beta_3$. Similarly, variations of κ_i ($i = \{p, t\}$) affect Equations (2.18)–(2.19), but
583 also Equations (2.4)–(2.5) via definition (2.14) as $\hat{\kappa}_i = \kappa_i/\varepsilon$ (see (A.16)).

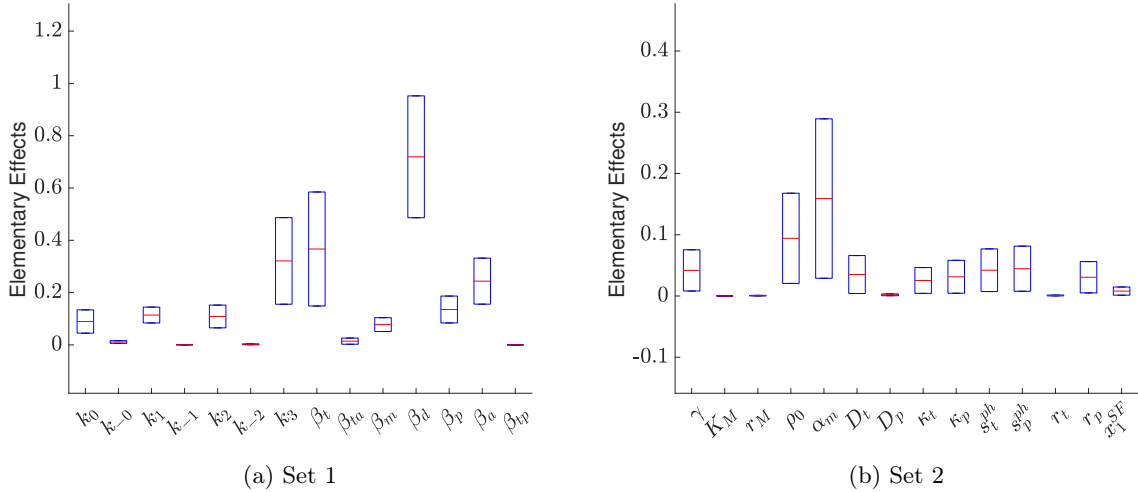


Figure 7: **GSA highlights the most influential parameters of the full model (2.1)–(2.13) on the speed of BM digestion.** Using Morris' method, we quantify the impact of changes in parameter values on the time evolution of the BM density. The boxplots display mean and standard deviation of the EEs of each parameter in Set 1 (a) and Set 2 (b), as prescribed in Section 3.2.2, on the output Y defined in (3.1) (see Section 3.2.1 for details on the methodology). The most influential parameters are the decay rates of MT1-MMP dimers β_d and TIMP-2 β_t , the activation rate of MMP-2 k_3 , the rate of MT1-MMP monomer expression by cancer cells α_m and the tumor cell density ρ_0 . Changes of these parameters lead to large linear and nonlinear effects on the output.

584 Figure 7 summarizes the results of the GSA of the full model. We observe that, for parameter Set 1
585 (Figure 7a), the most important parameter is the decay rate β_d . This is explained by the fact that changes

586 in this value not only affect the concentration of MT1-MMP dimers, which is crucial in the activation
 587 process, but also that of all complexes involving this compound (cf. Remark 2), resulting in an amplified
 588 effect of this parameter. Changes in the TIMP-2 decay rate β_t also lead to large variations in the output,
 589 visibly larger than those observed for the decay rates of proMMP-2 and MMP-2. As this parameter directly
 590 affects the amount of TIMP-2, this result further highlights the importance of the dual role of TIMP-2 as
 591 both activator and inhibitor of MMP-2. The parameter with third largest impact on the model output is
 592 k_3 , the rate of MMP-2 activation at the end of the activation cascade, which directly impacts the amount
 593 of active MMP-2. The larger effect of this parameter, compared to those of the association coefficients
 594 involved in the activation process k_0 , k_1 and k_2 , could be attributed to the irreversibility of the reaction
 595 it relates to. On the other hand, the dissociation rates k_{-i} ($i = \{0, 1, 2\}$) and decay rates of TIMP-bound
 596 active and inactive MMP-2 appear to have a negligible effect. In parameter Set 2 (Figure 7b), we notice
 597 that the MT1-MMP expression rate by cancer cells α_m has the largest effect on the outcome, immediately
 598 followed by the cancer cell density ρ_0 . This re-stresses the importance for BM digestion of MT1-MMP
 599 production on the surface of cancer cells, indeed one of the corner stones of MMP-2 activation. We note
 600 that the Michaelis-Menten constant of BM proteolytic degradation K_M , the BM production rate r_M and
 601 TIMP-2 production rate by the SF r_t appear to have negligible effect, likely due to the relatively small
 602 value of these parameters. Last, but not least, we remark that all most influential parameters induce
 603 both linear and non-linear effects. This means that the influence of an individual change of any of these
 604 parameters lead to an important variation in the output but also that changing two or more of these
 605 influential parameters at the same time results in an even larger variation of the output due to cumulative
 606 effects.

607 3.2.3 Global sensitivity analysis of the reduced system

608 We perform GSA on the reduced system (2.24)–(2.27) with (2.12)–(2.13), considering two sets of parame-
 609 ters:

610 *Set 1:* The biochemical reaction coefficients ($k_1, k_{-1}, k_2, k_{-2}, k_3$) and the fixed concentration of free
 611 dimeric MT1-MMPs (\bar{c}_d).

612 *Set 2:* The proMMP-2 and TIMP-2 decay rates (β_p, β_t), their production and diffusion rates in the CT
 613 ($s_t^{ph}, s_p^{ph}, r_t, r_p, D_p, D_t$), their transmission to the BM (κ_t, κ_p), the parameters related to the digestion
 614 and the production of the BM (γ, r_M, K_M), and the position of the SF in the CT (x_1^{SF}).

615 Figure 8 summarizes the results of the GSA of the reduced model. The main observation is that the
 616 value of \bar{c}_d (Figure 8a), *i.e.* the fixed concentration of free dimeric MT1-MMPs, is crucial for the output
 617 of the reduced system, with EEs mean notably larger than those obtained for the full system. Indeed this
 618 parameter encapsulates the effect of MT1-MMP expression and internalisation by cancer cells, and that of
 619 MT1-MMP dimerisation and de-dimerisation, *i.e.* it includes the effect of ρ_0 , α_m and β_d which were among
 620 the most influential parameters in the full model. Notably, the MMP-2 activation rate k_3 appears to have
 621 negligible effects in the reduced system, as opposed to its strong impact in the full model. This might result
 622 from the quasi steady-state assumption on the activation complexes imposed during model reduction –
 623 mathematically, this is explained by the fact that k_3 appears at the nominator and denominator of the same
 624 fraction in equations (2.26) and (2.27). The reduced impact of k_3 likely favours the striking effect of \bar{c}_d .
 625 Another parameter that has a remarkably larger EEs mean in the GSA of the reduced model, compared
 626 to that found for the full model, is the BM degradation rate γ (Figure 8b). Interestingly, we observe
 627 that the parameters in Set 2 relating to proMMP-2 dynamics appear to have consistently larger effects
 628 on the output than the analogous TIMP-2 related parameters, with the physiological production rate
 629 of proMMP-2 s_p^{ph} having gained significant importance. While the model’s sensitivity to uncertainty in
 630 these inputs has changed upon model reduction, the negligible effect of K_M , r_M and r_t remains consistent
 631 across models. Finally, we again have that all most influential parameters induce both linear and non-
 632 linear effects, yet with a stronger impact than those identified for the full system, indicating an increased
 633 sensitivity upon model reduction.

634 4 Discussion

635 It is now widely recognised that cells in the stroma may play major roles in tumour progression. Our
 636 goal is to develop a mathematical model which can implement empirical data and suggest promising
 637 experimental investigations, in order to reduce the cost and timeline of the empirical work necessary

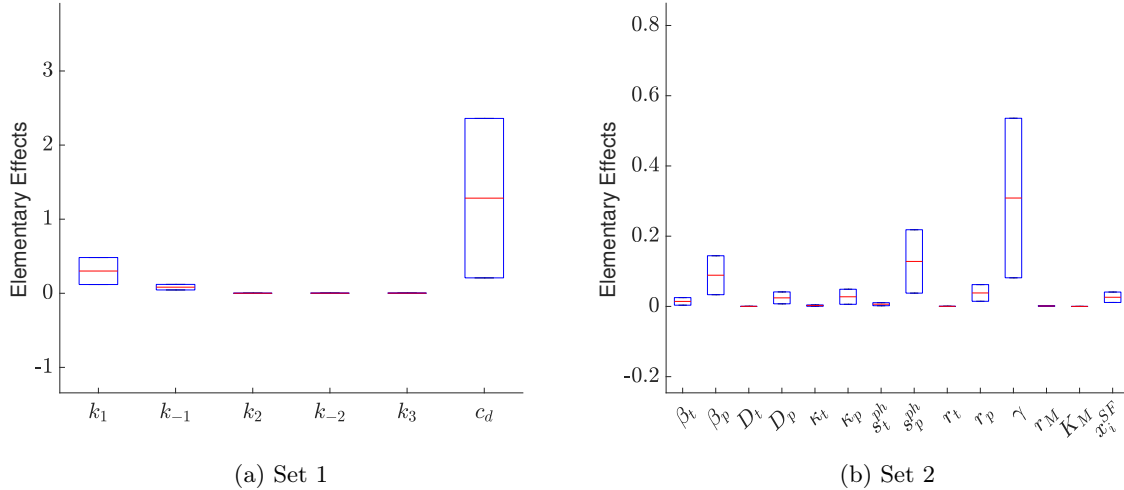


Figure 8: **GSA indicates that the reduced model (2.24)-(2.27) with (2.12)-(2.13) is more sensitive to uncertainty in the most influential parameters compared to the full model.** Using Morris' method, we quantify the impact of changes in parameter values on the time evolution of the BM density. The boxplots display mean and standard deviation of the EEs of each parameter in Set 1 (a) and Set 2 (b), as prescribed in Section 3.2.3, on the output Y defined in (3.1) (see Section 3.2.1 for details on the methodology). The most influential parameter in the reduced system is the fixed concentration of free dimeric MT1-MMPs \bar{c}_d , followed by the BM degradation rate γ and the proMMP-2 physiological production rate s_p^{ph} . EEs means and standard deviation of the most influential parameters of the reduced system are larger than those of the full system, indicating increased sensitivity of the reduced model.

638 to promote therapeutic strategies targeting SFs against carcinoma progression. We presented in this
 639 article the results of our initial modelling efforts, which focus on the first step of the invasion cascade:
 640 the rupture of the BM. We proposed a tractable and detailed model of BM digestion by cancer cells
 641 involving the contribution of SFs located in the CT, which builds on the current biological knowledge of
 642 this phenomenon.

643 4.1 Summary of modelling efforts and key results

644 **Our model contains several elements of novelty which ensure that various aspects of biological complexity relevant to carcinoma invasion are captured within the same framework.** To
 645 the best of our knowledge, the present work is the first to mathematically represent tumor cells mediated
 646 rupture of the BM aided by SF secretome. Remarkable modelling progress to capture cancer invasion
 647 following BM digestion was achieved by Gallinato *et al.* [41], and following extensions [19]. However, in
 648 these works the BM digestion was modelled as the result of the activity of degrading enzymes secreted only
 649 by the tumor. Our model captures the diffusion of the SF secretome inside the CT and its transmission to
 650 the BM, at the other end of which these enzymes may interact with MT1-MMP located on the membrane
 651 of tumor cells, and activate MMP-2. The inclusion of these dynamics in the mathematical model enables
 652 the study of the partnerships that exist between tumor cells and helping cells in the stroma, which are
 653 nowadays well known to aid cancer invasion. While this framework, including fibroblast facilitating ECM
 654 degradation by cancer cells, was partially considered in [66] for a Tumour Chamber Invasion Assay, our
 655 model captures better the dimensionality of the problem by considering the BM to be a $d - 1$ dimensional
 656 domain, where d is the dimension of the CT, as similarly done in [41]. Altogether, our model allows for a
 657 more complete and biophysically consistent representation of the phenomenon, and the results of numerical
 658 simulations highlight the importance of considering these pro-tumour cells located in the stroma, as
 659 the digestion of the BM appears faster closer to a SF rich CT area.

660 Compared to the aforementioned works and previous mathematical models of tumor invasion (see
 661 *e.g.* [17, 18, 61, 88]), our model also comprises a comprehensive description of the biochemical reactions
 662 regulating the activation and inhibition of MMP-2, capturing the dual role of TIMP-2 as only previously
 663 seen in dedicated studies ignoring spatial dynamics [62, 98]. We remark that such dual role of TIMP-2 is
 664 still captured in the reduced model that we derived using typical simplifying assumptions, as demonstrated
 665 by the results of our steady state analysis, summarised in Figure 3.
 666

667 Moreover, additional efforts were made in this work to extract parameter values from the literature,
668 deriving several missing ones from steady state assumptions and reference enzyme concentrations reported
669 in empirical studies. Hence, except for 2 of them (the production rates of enzymes by SF, *i.e.* r_p, r_i), most
670 of the parameters are directly found from experimental studies or previous modelling works that fit these
671 parameters using experimental data. The remaining parameters are obtained from simple computations:
672 starting from empirical measurements of physiological enzyme concentrations, we compute the remaining
673 parameters assuming that the physiological conditions correspond to steady-states in the reaction-diffusion
674 equations. This procedure allowed us to find biologically relevant parameter values. We conducted a
675 sensitivity analysis to estimate how errors on these parameter values could influence the output of the
676 model and that of a reduced model obtained under typical simplifying assumptions. This latter part of
677 the work is crucial, as it also highlights changes in the model's sensitivity upon reduction, which is not
678 very often considered for invasion models.

679 **The results of numerical simulations are in good qualitative agreement with the current**
680 **biological understanding of the phenomenon.** The flexibility of the model allowed us to explore
681 the behavior of the system on the relevant test cases, reproducible under different parameter sets, via
682 numerical simulations. The model predicts that the presence of an epithelial tumour may result in slow
683 BM digestion at the tumour location, as opposed to the case of a healthy tissue where the BM remains
684 intact, thanks to the presence of MT1-MMPs on the surface of tumour cells which initiate the MMP-2
685 activation cascade. Moreover, our results clarify that SF secretome may aggravate the imbalance between
686 the activation and inhibition dynamics of MMP-2, boosting cancer invasion. In fact, the inclusion of SFs
687 in the CT results in the emergence of more accurate gradients of proMMP-2 in the CT, extending radially
688 from the position of the SF, and faster digestion of the BM localized at the points closest to the SF. It is
689 at this point that we expect to first observe BM rupture, *i.e.* the decrease of BM density below a threshold
690 allowing cells to pass through the BM, and the initiation of cancer invasion. Our results also highlight
691 that the possibility of observing BM rupture within a given time frame increases as the distance between
692 the SF and the BM decreases, as the rate of proMMP-2 secretion by the SF increases and as its TIMP-2
693 secretion rate decreases. These secretion rates are hard to estimate as they may vary across experimental
694 conditions, tissue samples and among SF population.

695 While these results are in good qualitative agreement with the current biological understanding of
696 the phenomenon, we remark that the amount of time after which the model predicts BM rupture may
697 not accurately convey the empirical timescale of this phenomenon, which may be faster. First of all,
698 the critical BM density for cancer invasion, which we arbitrarily set to half the carrying capacity, may
699 be higher. Secondly, we considered the presence of only one SF in the CT for illustrative purposes –
700 although the model is flexible enough to represent numerous SFs in different locations within the CT –
701 and *in vivo* the number of SFs may be significantly larger, yielding an enhanced effect of combined SFs'
702 secretome. Lastly, despite the great efforts made in identifying appropriate parameter values, these are
703 taken or estimated from a variety of works in the literature, and model calibration with experimental data
704 is necessary to ensure a wholly coherent parameter set.

705 **Sensitivity analysis reveals that model prediction accuracy depends on knowledge of the**
706 **amount of MT1-MMPs that epithelial tumor cell express at the invadopodia, especially**
707 **after model reduction.** Given the large number of parameters in the full model, we derived a reduced
708 version of the model under biologically motivated simplifying assumptions on the relative scales of the
709 dynamics prescribed within the MMP-2 activation cascade. We remark that these assumptions were
710 further justified by the results of numerical simulations, during which concentrations of soluble molecules
711 reached equilibrium much faster than the BM density. Model reduction not only lowers the degrees of
712 freedom of the system, facilitating future experimental calibration of the model, but also allows us to
713 draw analytical conclusions on the equilibrium of the system and necessary conditions for sustained BM
714 rupture. Moreover, it allows for a comparison with previous cancer invasion mathematical models that
715 included some MMP-2 activation or inhibition dynamics under similar assumptions.

716 In view of this calibration, we performed GSA to investigate the models' robustness to uncertainty
717 in the parameter values and identify the most influential parameters on the speed of BM digestion by
718 cancer cells in the presence of a SF in the CT. The most influential parameters of both versions of the
719 model displayed both linear and non-linear effects, indicating uncertainty in these inputs may influence the
720 model output also through its interaction with other parameters, as expected given the complexity of the
721 equations and dynamics prescribed in the model. Notably, we found that the most influential parameters
722 of the full model have lower EEs mean and standard variation than those of the reduced model. This

723 suggests that the predictive capability of the full model is more robust to uncertainty of parameter values
724 than the reduced one, and it is therefore better suited for *in silico* investigations when the parameters are
725 not accurately measured, despite the higher computational cost.

726 From the GSA we found that uncertainty in the parameters associated with the amount of MT1-MMPs
727 available on the surface of cancer cells – *i.e.* tumour cell number, MT1-MMP expression rate by tumour
728 cells, internalisation rate of MT1-MMP dimers and complexes involving it – has the largest impact on the
729 output of the full model. This was followed by an important role played by the rate of the irreversible
730 reaction at the end of the MMP-2 activation cascade. Interestingly, we found that this latter parameter
731 had negligible effect on the output of the reduced model, which may be an advantage in the absence of
732 accurate estimates for this rate. However, this advantage is counterbalanced by the intensified effect of
733 the parameter modelling the fixed concentration of free dimeric MT1-MMPs, which only appears in the
734 reduced model capturing the collective effect of the MT1-MMP dynamics on the surface of cancer cells.
735 Such simplification is the main drawback of the reduced model, as enormous importance is given to a
736 parameter which is even more difficult to measure empirically.

737 4.2 Modelling and interdisciplinary perspectives

738 **Mathematical modelling perspectives.** In this work we use mathematical modelling to represent and
739 study the contribution of SF secretome in initial cancerous progression of carcinoma toward BM rupture
740 and invasion. In particular, we investigate the potential impact of this partnership on the digestion of the
741 BM, which is the first step of carcinoma invasion. While our model is able to capture numerous biological
742 effects, there are several planned extensions that would allow the inclusion of additional biologically
743 relevant features.

744 The transmission coefficient κ_i ($i = t, p$) models the rate at which proteins from the CT are transmitted
745 to and across the BM. It is computed using the diffusion coefficient D_i of the protein and the width of
746 the BM. In particular, we assumed that the diffusivity of each protein in the BM is 10^{-6} smaller than
747 in the CT (see Appendix B), a coarse assumption explained by the fact that the BM is a dense sheet
748 of collagen fibers. A more accurate description of the protein diffusivity in the BM could be achieved
749 integrating information on the physical properties of the BM in this parameter. Specifically, it would be
750 relevant to use a diffusion coefficient dependent on the tortuosity of the BM, which is related to the pore
751 sizes of the ECM network within the BM, estimated to be between 10 and 130 nm in diameter [59]. This
752 is particularly relevant in our modelling framework because as the BM is degraded, the size of the pores
753 increase, ultimately increasing the protein diffusivity within the BM. This effect could be implemented
754 in our model by considering a BM density dependent transmission coefficient $\kappa_i(M) = K_i(M) \frac{D_i}{\epsilon}$ with
755 $0 \leq K_i(M) < 1$ being the partitioning coefficient (as in [38]).

756 Secondly, in our model, MT1-MMP turnover is modelled as a combination of the production of
757 monomeric MT1-MMP by cancer cells, with rate α_m , and the internalization of monomeric, dimeric
758 and complexes involving MT1-MMPs, via decay terms with rates β_i ($i = m, d, 1, 2, 3$). While this was
759 sufficiently detailed for the purpose of this first work, it might be an overly simplified representation of
760 MT1-MMP turnover. As MT1-MMP turnover also plays an important role in subsequent steps of invasion
761 in the CT, it might be relevant to adapt the model proposed in [55] to our setting.

762 In the present work, we only consider the digestion of the BM by MMP-2 enriched in SF secretome and
763 activated by tumor cells. Nonetheless, degradation of the BM may also be mediated by MT1-MMPs or by
764 other MMPs directly produced by tumor cells. This process was neglected for the moment to discriminate
765 the effect of SFs located in the CT in the digestion of the BM. The addition of a source term of proMMP,
766 of the form of $\alpha_p \rho_0$ (α_p corresponding to the rate of production of proMMP by the tumor cells, having unit
767 nmol/cell/s) in the equation for the proMMP-2 in the BM may be sufficient to include this phenomenon.

768 Furthermore, while we only consider the action of MMP-2 in this work, it may be relevant to extend
769 this framework to include the dynamics of other MMP subtypes. For instance, MMP-9 may play an
770 important role in the digestion of the BM and the invasion process (see [57] and references therein), even
771 though no relevant amount of MMP-9 was measured in SF secretome in [81]. In this natural extension
772 of our work, MMP-9 dynamics may be captured with a modelling strategy analogous to that used for
773 MMP-2.

774 Finally, as already demonstrated by experimental observations, SFs' secretome plays a role not only
775 in the digestion of the BM, but also in the subsequent invasion of carcinoma cells in the CT [81]. It may,
776 in particular, promote epithelial-to-mesenchymal transition of carcinoma cells, enhancing their motility
777 capabilities. Our next efforts will be devoted to the development of a model of invasion of carcinoma cells
778 inside the CT, and we will focus on capturing the cancer cell motility-boosting effect of SF secretome.

779 Coupling a model for invasion inside the CT and the present model will lead to a complete mathematical
780 representation of the partnership between carcinoma cells and the SFs during invasion.

781 **Interdisciplinary perspectives.** A limitation of our work was our ability to find precise parameter
782 values that correspond to the specific pathophysiological context under study. Although a thorough
783 calibration from the literature was conducted, some parameters are not found in the current literature or
784 originate from different contexts, not specifically measured using epithelial samples. For example, reference
785 enzyme concentrations used in this work were measured in plasma serum, due to a lack of measurements in
786 tissues. Most probably, concentrations differ from one tissue to another. The importance of this limitation
787 is highlighted by the results of our sensitivity analysis, which demonstrate that uncertainties on limited
788 parameter values could tremendously impact the simulations' outputs. This will be a crucial point for our
789 future work, where we will compare our model's numerical results to the results of biological experiments.
790 We aim to accurately replicate the experimental setup *in silico* to achieve quantitative comparisons.

791 Therefore our numerical model needs to be fed by data gathered from biological models mimicking
792 skin carcinoma progression, which will allow us to harvest critical information on specific factors involved
793 in early cancer progression. Specifically, organotypic 3D models of skin carcinoma progression are being
794 developed to allow us to gather data on the impact of cellular and matricial densities, proximity of stroma
795 cells and their secretory activity in the senescent context. Moreover, data on protein concentrations and
796 gradients analyzed in human biopsy specimen from the clinic will also be relevant, in order to identify the
797 histological expression patterns of critical molecules associated with different stages of cancer progression
798 and invasion features, or in samples from patients of different ages.

799 Data from these experiments, and from patients, will nourish the mathematical model with quan-
800 titative information that will improve the quality and specificity of parameter values upon empirical
801 calibration. Therefore, the concentrations of critical actors identified in the model from the sensitivity
802 analysis will be measured in the biological model in order to replace those inferred from related literature.
803 This will help improve the predictive capability of the model and allow the simulation of scenarii in which
804 molecules or processes are targeted to interfere with cancer progression. In summary, the mathematical
805 and biological model will mutually feed one another, in a synergistic numerical and experimental approach.

806 Carcinoma invasive growth also comprises other factors such as inflammation, collective and individual
807 migration of tumor cells, mechanical effects such as pressure, stiffening of the tissue, and partnerships
808 existing with other cells of the stroma (*e.g.* macrophages, cancer-associated fibroblasts, . . .). The ultimate
809 goal of our work will be to progressively add new cellular contributions to build a complete model of
810 carcinoma invasion that comprises more of the previously mentioned effects. Even though such a model
811 will be highly complex, the present work demonstrates that designing and simulating an already complex
812 subsystem, as well as characterizing a large parameter set using the literature, is manageable.

Acronym	Meaning	Acronym	Meaning
BM	Basement Membrane	ODE	Ordinary Differential Equation
CAF	Cancer-Associated Fibroblast	proMMP	MMP precursor
CT	Conjunctive Tissue	PDE	Partial Differential Equation
ECM	Extracellular Matrix	SF	Senescent Fibroblast
GSA	Global Sensitivity Analysis	TAM	Tumour-Associated Macrophages
MMP	Matrix MetalloProteinases	TIMP	Tissue-Inhibitor of MMP
MT1-MMP	Membrane-Type MMP	TME	Tumour Microenvironment

Table 4: List of frequently used acronyms.

813 Acknowledgements

814 This project has received funding from the European Union's Horizon 2020 research and innovation pro-
815 gramme under the Marie Skłodowska-Curie grant agreement No 945298-ParisRegionFP. C.V. is a Fellow
816 of the Paris Region Fellowship Programme, supported by the Paris Region. A.P. acknowledges support
817 from the Labex CEMPI (ANR-11-LABX-0007-01). This work has been partially funded by the PEPS
818 JCJC project "Conservative numerical schemes for novel structured PDE models of cancer invasion" from
819 INSMI - CNRS.

References

- [1] N. J. AHERNE, A. DHAWAN, J. G. SCOTT, AND H. ENDERLING, *Mathematical oncology and its application in non melanoma skin cancer—a primer for radiation oncology professionals*, Oral oncology, 103 (2020), p. 104473.
- [2] A. ALBINI, Y. IWAMOTO, H. KLEINMAN, G. MARTIN, S. AARONSON, J. KOZLOWSKI, AND R. MCEWAN, *A rapid in vitro assay for quantitating the invasive potential of tumor cells*, Cancer research, 47 (1987), pp. 3239–3245.
- [3] P. M. ALTROCK, L. L. LIU, AND F. MICHOR, *The mathematics of cancer: integrating quantitative models*, Nature Reviews Cancer, 15 (2015), pp. 730–745.
- [4] T.-M. ANNE, T.-H. TAINA, ET AL., *Levels of circulating timp-2 and mmp2-timp2 complex are decreased in squamous cervical carcinoma*, Obstetrics and Gynecology International, 2010 (2010).
- [5] P. J. ASIF, C. LONGOBARDI, M. HAHNE, AND J. P. MEDEMA, *The role of cancer-associated fibroblasts in cancer invasion and metastasis*, Cancers, 13 (2021).
- [6] D. J. BAKER, T. WIJSHAKE, T. TCHKONIA, N. K. LEBRASSEUR, B. G. CHILDS, B. VAN DE SLUIS, J. L. KIRKLAND, AND J. M. VAN DEURSEN, *Clearance of p16ink4a-positive senescent cells delays ageing-associated disorders*, Nature, 479 (2011), p. 232–236.
- [7] P. BALUK, S. MORIKAWA, A. HASKELL, M. MANCUSO, AND D. M. McDONALD, *Abnormalities of basement membrane on blood vessels and endothelial sprouts in tumors*, The American journal of pathology, 163 (2003), pp. 1801–1815.
- [8] D. BARBOLOSI, J. CICCOLINI, B. LACARELLE, F. BARLÉSI, AND N. ANDRÉ, *Computational oncology—mathematical modelling of drug regimens for precision medicine*, Nature reviews Clinical oncology, 13 (2016), pp. 242–254.
- [9] L. BARTHA AND R. EFTIMIE, *Mathematical investigation into the role of macrophage heterogeneity on the temporal and spatio-temporal dynamics of non-small cell lung cancers*, Journal of Theoretical Biology, 549 (2022), p. 111207.
- [10] S. BEKISZ AND L. GERIS, *Cancer modeling: From mechanistic to data-driven approaches, and from fundamental insights to clinical applications*, Journal of Computational Science, 46 (2020), p. 101198. 20 years of computational science.
- [11] I. BEN-PORATH AND R. A. WEINBERG, *When cells get stressed: an integrative view of cellular senescence*, The Journal of Clinical Investigation, 113 (2004), pp. 8–13.
- [12] L. BERBEN, G. FLORIS, H. WILDIERS, AND S. HATSE, *Cancer and aging: Two tightly interconnected biological processes*, Cancers, 13 (2021).
- [13] J. A. BULL AND H. M. BYRNE, *The hallmarks of mathematical oncology*, Proceedings of the IEEE, 110 (2022), pp. 523–540.
- [14] G. A. CABRAL-PACHECO, I. GARZA-VELOZ, C. CASTRUITA-DE LA ROSA, J. M. RAMIREZ-ACUÑA, B. A. PEREZ-ROMERO, J. F. GUERRERO-RODRIGUEZ, N. MARTINEZ-AVILA, AND M. L. MARTINEZ-FIERRO, *The roles of matrix metalloproteinases and their inhibitors in human diseases*, International Journal of Molecular Sciences, 21 (2020), p. 9739.
- [15] J. M. CASTELLANO, K. I. MOSHER, R. J. ABBEY, A. A. MCBRIDE, M. L. JAMES, D. BERDNIK, J. C. SHEN, B. ZOU, X. S. XIE, M. TINGLE, ET AL., *Human umbilical cord plasma proteins revitalize hippocampal function in aged mice*, Nature, 544 (2017), pp. 488–492.
- [16] M. A. CEPEDA, J. J. PELLING, C. L. EVERED, K. C. WILLIAMS, Z. FREEDMAN, I. STAN, J. A. WILLSON, H. S. LEONG, AND S. DAMJANOVSKI, *Less is more: low expression of mt1-mmp is optimal to promote migration and tumorigenesis of breast cancer cells*, Molecular cancer, 15 (2016), pp. 1–27.
- [17] M. CHAPLAIN AND N. DEAKIN, *Mathematical modeling of cancer invasion: The role of membrane-bound matrix metalloproteinases*, Frontiers in Oncology, 3 (2013).

- 867 [18] M. CHAPLAIN AND G. LOLAS, *Mathematical modelling of cancer invasion of tissue: dynamic het-*
868 *erogeneity*, Networks and Heterogeneous Media, 1 (2006), pp. 399–439.
- 869 [19] M. A. CHAPLAIN, C. GIVERSO, T. LORENZI, AND L. PREZIOSI, *Derivation and application of effec-*
870 *tive interface conditions for continuum mechanical models of cell invasion through thin membranes*,
871 SIAM Journal on Applied Mathematics, 79 (2019), pp. 2011–2031.
- 872 [20] M. A. CHELLAIAH, T. MA, ET AL., *Membrane localization of membrane type 1 matrix metallo-*
873 *proteinase by cd44 regulates the activation of pro-matrix metalloproteinase 9 in osteoclasts*, BioMed
874 Research International, 2013 (2013).
- 875 [21] G. CIAVOLELLA, N. DAVID, AND A. POULAIN, *Effective interface conditions for a porous medium*
876 *type problem*, Interfaces Free Bound., (2024).
- 877 [22] I. E. COLLIER, W. LEGANT, B. MARMER, O. LUBMAN, S. SAFFARIAN, T. WAKATSUKI, E. EL-
878 *SON*, AND G. I. GOLDBERG, *Diffusion of mmps on the surface of collagen fibrils: the mobile cell*
879 *surface-collagen substratum interface*, PloS one, 6 (2011), p. e24029.
- 880 [23] J.-P. COPPE, M. BOYSEN, C. H. SUN, B. J. WONG, M. K. KANG, N.-H. PARK, P.-Y. DESPREZ,
881 J. CAMPISI, AND A. KRTOLICA, *A Role for Fibroblasts in Mediating the Effects of Tobacco-Induced*
882 *Epithelial Cell Growth and Invasion*, Molecular Cancer Research, 6 (2008), pp. 1085–1098.
- 883 [24] J.-P. COPPÉ, P.-Y. DESPREZ, A. KRTOLICA, AND J. CAMPISI, *The senescence-associated secre-*
884 *tory phenotype: The dark side of tumor suppression*, Annual Review of Pathology: Mechanisms of
885 Disease, 5 (2010), pp. 99–118. PMID: 20078217.
- 886 [25] M. DEMESTRE, G. PARKIN-SMITH, A. PETZOLD, AND A. PULLEN, *The pro and the active form*
887 *of matrix metalloproteinase-9 is increased in serum of patients with amyotrophic lateral sclerosis*,
888 Journal of neuroimmunology, 159 (2005), pp. 146–154.
- 889 [26] E. I. DERYUGINA, M. A. BOURDON, K. JUNGWIRTH, J. W. SMITH, AND A. Y. STRONGIN,
890 *Functional activation of integrin $\alpha v \beta 3$ in tumor cells expressing membrane-type 1 matrix metallo-*
891 *proteinase*, International journal of cancer, 86 (2000), pp. 15–23.
- 892 [27] E. I. DERYUGINA AND J. P. QUIGLEY, *Matrix metalloproteinases and tumor metastasis*, Cancer
893 and metastasis reviews, 25 (2006), pp. 9–34.
- 894 [28] G. P. DIMRI, X. LEE, G. BASILE, M. ACOSTA, G. SCOTT, C. ROSKELLEY, E. E. MEDRANO,
895 M. LINSKENS, I. RUBELJ, AND O. PEREIRA-SMITH, *A biomarker that identifies senescent human*
896 *cells in culture and in aging skin in vivo.*, Proceedings of the National Academy of Sciences, 92
897 (1995), pp. 9363–9367.
- 898 [29] P. DOMSCHKE, D. TRUCU, A. GERISCH, AND M. A. J. CHAPLAIN, *Mathematical modelling of*
899 *cancer invasion: Implications of cell adhesion variability for tumour infiltrative growth patterns*,
900 Journal of Theoretical Biology, 361 (2014), pp. 41–60.
- 901 [30] A. DONZÉ, E. FANCHON, L. M. GATTEPAILLE, O. MALER, AND P. TRACQUI, *Robustness analysis*
902 *and behavior discrimination in enzymatic reaction networks*, PloS one, 6 (2011), p. e24246.
- 903 [31] R. EFTIMIE AND L. GIBELLI, *A kinetic theory approach for modelling tumour and macrophages*
904 *heterogeneity and plasticity during cancer progression*, Mathematical Models and Methods in Applied
905 Sciences, 30 (2020), pp. 659–683.
- 906 [32] H. EMONARD, G. BELLON, L. TROEBERG, A. BERTON, A. ROBINET, P. HENRIET, E. MARBAIX,
907 K. KIRKEGAARD, L. PATTHY, Y. EECKHOUT, ET AL., *Low density lipoprotein receptor-related*
908 *protein mediates endocytic clearance of pro-mmp-2- timp-2 complex through a thrombospondin-*
909 *independent mechanism*, Journal of Biological Chemistry, 279 (2004), pp. 54944–54951.
- 910 [33] H. ENDERLING AND M. AJ CHAPLAIN, *Mathematical modeling of tumor growth and treatment*,
911 Current pharmaceutical design, 20 (2014), pp. 4934–4940.
- 912 [34] R. EYMARD, T. GALLOUËT, AND R. HERBIN, *Finite volume methods*, in Handbook of numerical
913 analysis, Vol. VII, vol. VII of Handb. Numer. Anal., North-Holland, Amsterdam, 2000, pp. 713–1020.
- 914 [35] D. FABIAN AND T. FLATT, *The evolution of aging*, Nature Education Knowledge, 3 (2011), pp. 1–10.

- 915 [36] M. FANE AND A. T. WEERARATNA, *How the ageing microenvironment influences tumour progres-*
916 *sion*, Nature Reviews Cancer, 20 (2020), p. 89–106.
- 917 [37] J. FERLAY, M. ERVIK, F. LAM, M. LAVERSANNE, M. COLOMBET, L. MERY, M. PIÑEROS,
918 A. ZNAOR, I. SOERJOMATARAM, AND F. BRAY, *Global cancer observatory: Cancer today (version*
919 *1.1)*, 2024. Lyon, France: International Agency for Research on Cancer. Available from: <https://gco.iarc.who.int/today>,
920 accessed: (22/03/2024).
- 921 [38] W. H. FISSELL, C. L. HOFMANN, N. FERRELL, L. SCHNELL, A. DUBNISHEVA, A. L. ZYD-
922 NEY, P. D. YURCHENCO, AND S. ROY, *Solute partitioning and filtration by extracellular matrices*,
923 American Journal of Physiology-Renal Physiology, 297 (2009), pp. F1092–F1100.
- 924 [39] C. FRANTZ, K. M. STEWART, AND V. M. WEAVER, *The extracellular matrix at a glance*, Journal
925 of Cell Science, 123 (2010), pp. 4195–4200.
- 926 [40] A. FRIEDMAN, C. HUANG, AND J. YONG, *Effective permeability of the boundary of a domain*,
927 Communications in Partial Differential Equations, 20 (1995), pp. 59–102.
- 928 [41] O. GALLINATO, T. COLIN, O. SAUT, AND C. POIGNARD, *Tumor growth model of ductal carcinoma:*
929 *from in situ phase to stroma invasion*, Journal of Theoretical Biology, 429 (2017), pp. 253–266.
- 930 [42] R. A. GATENBY AND E. T. GAWLINSKI, *A reaction-diffusion model of cancer invasion*, Cancer
931 research, 56 (1996), pp. 5745–5753.
- 932 [43] J. GIROUD, I. BOURIEZ, H. PAULUS, A. POURTIER, F. DEBACQ-CHAINIAUX, AND O. PLUQUET,
933 *Exploring the communication of the sasp: Dynamic, interactive, and adaptive effects on the mi-*
934 *croenvironment*, International Journal of Molecular Sciences, 24 (2023).
- 935 [44] C. GIVERSO, T. LORENZI, AND L. PREZIOSI, *Effective interface conditions for continuum mechan-*
936 *ical models describing the invasion of multiple cell populations through thin membranes*, Applied
937 Mathematics Letters, 125 (2022), p. 107708.
- 938 [45] L. GROSSE, N. WAGNER, A. EMELYANOV, C. MOLINA, S. LACAS-GERVAIS, K.-D. WAGNER, AND
939 D. V. BULAVIN, *Defined p16high senescent cell types are indispensable for mouse healthspan*, Cell
940 Metabolism, 32 (2020), pp. 87–99.e6.
- 941 [46] D. HANAHAN, *Hallmarks of cancer: new dimensions*, Cancer discovery, 12 (2022), pp. 31–46.
- 942 [47] D. HANAHAN AND R. A. WEINBERG, *The hallmarks of cancer*, cell, 100 (2000), pp. 57–70.
- 943 [48] ———, *Hallmarks of cancer: the next generation*, cell, 144 (2011), pp. 646–674.
- 944 [49] Y. HASSONA, N. CIRILLO, K. HEESOM, E. PARKINSON, AND S. S. PRIME, *Senescent cancer-*
945 *associated fibroblasts secrete active mmp-2 that promotes keratinocyte dis-cohesion and invasion*,
946 British journal of cancer, 111 (2014), pp. 1230–1237.
- 947 [50] Z. HEIDARY, J. GHASARI, S. MOEIN, AND S. HAGHJOY JAVANMARD, *The double-edged sword*
948 *role of fibroblasts in the interaction with cancer cells; an agent-based modeling approach*, PloS one,
949 15 (2020), p. e0232965.
- 950 [51] P. HENRIET AND H. EMONARD, *Matrix metalloproteinase-2: Not (just) a “hero” of the past*,
951 Biochimie, 166 (2019), p. 223–232.
- 952 [52] T. HERNANDEZ-BOUSSARD, P. MACKLIN, E. J. GREENSPAN, A. L. GRYSHUK, E. STAHLBERG,
953 T. SYEDA-MAHMOOD, AND I. SHMULEVICH, *Digital twins for predictive oncology will be a paradigm*
954 *shift for precision cancer care*, Nature medicine, 27 (2021), pp. 2065–2066.
- 955 [53] F. HILLEN AND A. W. GRIFFIOEN, *Tumour vascularization: sprouting angiogenesis and beyond*,
956 Cancer and Metastasis Reviews, 26 (2007), pp. 489–502.
- 957 [54] U. B. HOFMANN, J. R. WESTPHAL, G. N. VAN MUIJEN, AND D. J. RUITER, *Matrix metallopro-*
958 *teinases in human melanoma*, Journal of Investigative Dermatology, 115 (2000), pp. 337–344.
- 959 [55] D. HOSHINO, N. KOSHIKAWA, T. SUZUKI, V. QUARANTA, A. M. WEAVER, M. SEIKI, AND
960 K. ICHIKAWA, *Establishment and validation of computational model for mt1-mmp dependent ecm*
961 *degradation and intervention strategies*, PLoS computational biology, 8 (2012), p. e1002479.

- 962 [56] W. HU, L. FANG, R. NI, H. ZHANG, AND G. PAN, *Changing trends in the disease burden of non-*
963 *melanoma skin cancer globally from 1990 to 2019 and its predicted level in 25 years*, BMC Cancer,
964 22 (2022).
- 965 [57] H. HUANG, *Matrix metalloproteinase-9 (mmp-9) as a cancer biomarker and mmp-9 biosensors:*
966 *Recent advances*, Sensors, 18 (2018).
- 967 [58] B. IOOSS AND P. LEMAÎTRE, *A review on global sensitivity analysis methods*, in Uncertainty Man-
968 *agement in Simulation-Optimization of Complex Systems: Algorithms and Applications*, G. Dellino
969 and C. Meloni, eds., Springer US, Boston, MA, 2015, pp. 101–122.
- 970 [59] R. JAYADEV AND D. R. SHERWOOD, *Basement membranes*, Current Biology, 27 (2017), pp. R207–
971 R211.
- 972 [60] A. JIANG, K. LEHTI, X. WANG, S. J. WEISS, J. KESKI-OJA, AND D. PEI, *Regulation of*
973 *membrane-type matrix metalloproteinase 1 activity by dynamin-mediated endocytosis*, Proceedings
974 of the National Academy of Sciences, 98 (2001), pp. 13693–13698.
- 975 [61] J. JOSHI, M. D. ABNAVI, AND C. R. KOTHAPALLI, *Synthesis and secretome release by human bone*
976 *marrow mesenchymal stem cell spheroids within three-dimensional collagen hydrogels: Integrating*
977 *experiments and modelling*, Journal of Tissue Engineering and Regenerative Medicine, 13 (2019),
978 pp. 1923–1937.
- 979 [62] E. D. KARAGIANNIS AND A. S. POPEL, *A theoretical model of type i collagen proteolysis by ma-*
980 *trix metalloproteinase (mmp) 2 and membrane type 1 mmp in the presence of tissue inhibitor of*
981 *metalloproteinase 2*, Journal of Biological Chemistry, 279 (2004), pp. 39105–39114.
- 982 [63] O. KEDEM AND A. KATCHALSKY, *Thermodynamic analysis of the permeability of biological mem-*
983 *branes to non-electrolytes*, Biochimica et biophysica Acta, 27 (1958), pp. 229–246.
- 984 [64] E. KIM, V. REBECCA, I. V. FEDORENKO, J. L. MESSINA, R. MATHEW, S. S. MARIA-ENGLER,
985 D. BASANTA, K. S. SMALLEY, AND A. R. ANDERSON, *Senescent fibroblasts in melanoma initiation*
986 *and progression: an integrated theoretical, experimental, and clinical approach*, Cancer research, 73
987 (2013), pp. 6874–6885.
- 988 [65] Y. KIM AND A. FRIEDMAN, *Interaction of tumor with its micro-environment: A mathematical*
989 *model*, Bulletin of mathematical biology, 72 (2010), pp. 1029–1068.
- 990 [66] Y. KIM, J. WALLACE, F. LI, M. OSTROWSKI, AND A. FRIEDMAN, *Transformed epithelial cells*
991 *and fibroblasts/myofibroblasts interaction in breast tumor: a mathematical model and experiments*,
992 Journal of mathematical biology, 61 (2010), pp. 401–421.
- 993 [67] F. KLEINHANS, *Membrane permeability modeling: Kedem–katchalsky vs a two-parameter formalism*,
994 Cryobiology, 37 (1998), pp. 271–289.
- 995 [68] H. KNÚTSDÓTTIR, E. PÁLSSON, AND L. EDELSTEIN-KESHET, *Mathematical model of macrophage-*
996 *facilitated breast cancer cells invasion*, Journal of theoretical biology, 357 (2014), pp. 184–199.
- 997 [69] A. KRTOŁICA, S. PARRINELLO, S. LOCKETT, P.-Y. DESPREZ, AND J. CAMPISI, *Senescent fibrob-*
998 *lasts promote epithelial cell growth and tumorigenesis: A link between cancer and aging*, Proceedings
999 of the National Academy of Sciences, 98 (2001), pp. 12072–12077.
- 1000 [70] J. K. KULAR, S. BASU, AND R. I. SHARMA, *The extracellular matrix: Structure, composition,*
1001 *age-related differences, tools for analysis and applications for tissue engineering*, Journal of Tissue
1002 Engineering, 5 (2014), p. 204173141455711.
- 1003 [71] E. LACONI, F. MARONGIU, AND J. DEGREGORI, *Cancer as a disease of old age: changing muta-*
1004 *tional and microenvironmental landscapes*, British journal of cancer, 122 (2020), pp. 943–952.
- 1005 [72] H. LARONHA AND J. CALDEIRA, *Structure and function of human matrix metalloproteinases*, Cells,
1006 9 (2020), p. 1076.
- 1007 [73] P. LAUDAŃSKI, J. SWIATECKA, L. KOZŁOWSKI, M. LEŚNIEWSKA, M. WOJTUKIEWICZ, AND
1008 S. WOŁCZYŃSKI, *Increased serum level of membrane type 1-matrix metalloproteinase (mt1-*
1009 *mmp/mmp-14) in patients with breast cancer.*, Folia histochemica et cytobiologica, 48 (2010),
1010 pp. 101–103.

- 1011 [74] F. LAURINO AND P. ZUNINO, *Derivation and analysis of coupled PDEs on manifolds with high*
1012 *dimensionality gap arising from topological model reduction*, ESAIM Math. Model. Numer. Anal.,
1013 53 (2019), pp. 2047–2080.
- 1014 [75] A. LEINONEN, M. MARIYAMA, T. MOCHIZUKI, K. TRYGGVASON, AND S. T. REEDERS, *Complete*
1015 *primary structure of the human type iv collagen alpha 4(iv) chain. comparison with structure and*
1016 *expression of the other alpha (iv) chains*, Journal of Biological Chemistry, 269 (1994), pp. 26172–
1017 26177.
- 1018 [76] Z. LIAO, H. L. YEO, S. W. WONG, AND Y. ZHAO, *Cellular senescence: Mechanisms and thera-*
1019 *peutic potential*, Biomedicines, 9 (2021).
- 1020 [77] K. V. LU, K. A. JONG, A. K. RAJASEKARAN, T. F. CLOUGHESY, AND P. S. MISCHEL, *Upregu-*
1021 *lation of tissue inhibitor of metalloproteinases (timp)-2 promotes matrix metalloproteinase (mmp)-2*
1022 *activation and cell invasion in a human glioblastoma cell line*, Laboratory investigation, 84 (2004),
1023 pp. 8–20.
- 1024 [78] I. LÜHR, A. FRIEDL, T. OVERATH, A. THOLEY, T. KUNZE, F. HILPERT, S. SEBENS, N. ARNOLD,
1025 F. RÖSEL, H.-H. OBERG, N. MAASS, C. MUNDHENKE, W. JONAT, AND M. BAUER, *Mammary*
1026 *fibroblasts regulate morphogenesis of normal and tumorigenic breast epithelial cells by mechanical*
1027 *and paracrine signals*, Cancer Letters, 325 (2012), pp. 175–188.
- 1028 [79] G. MAHLBACHER, L. T. CURTIS, J. LOWENGRUB, AND H. B. FRIEBOES, *Mathematical mod-*
1029 *eling of tumor-associated macrophage interactions with the cancer microenvironment*, Journal for
1030 immunotherapy of cancer, 6 (2018), pp. 1–17.
- 1031 [80] K. M. MAK AND R. MEI, *Basement membrane type iv collagen and laminin: An overview of*
1032 *their biology and value as fibrosis biomarkers of liver disease*, The Anatomical Record, 300 (2017),
1033 pp. 1371–1390.
- 1034 [81] N. MALAQUIN, C. VERCAMER, F. BOUALI, S. MARTIEN, E. DERUY, N. WERNERT, M. CHWASTY-
1035 NIAK, F. PINET, C. ABBADIE, AND A. POURTIER, *Senescent fibroblasts enhance early skin car-*
1036 *cinogenic events via a paracrine mmp-par-1 axis*, PLOS ONE, 8 (2013), pp. 1–17.
- 1037 [82] S. MARUŠIĆ AND E. MARUŠIĆ-PALOKA, *Two-scale convergence for thin domains and its applications*
1038 *to some lower-dimensional models in fluid mechanics*, Asymptot. Anal., 23 (2000), pp. 23–57.
- 1039 [83] S. MOMI, E. FALCINELLI, S. GIANNINI, L. RUGGERI, L. CECCHETTI, T. CORAZZI, C. LIBERT,
1040 AND P. GRESELE, *Loss of matrix metalloproteinase 2 in platelets reduces arterial thrombosis in vivo*,
1041 Journal of Experimental Medicine, 206 (2009), pp. 2365–2379.
- 1042 [84] M. D. MORRIS, *Factorial sampling plans for preliminary computational experiments*, Technometrics,
1043 33 (1991), pp. 161–174.
- 1044 [85] G. MURPHY, *Tissue inhibitors of metalloproteinases*, Genome biology, 12 (2011), pp. 1–7.
- 1045 [86] M. W. OLSON, D. C. GERVAZI, S. MOBASHERY, AND R. FRIDMAN, *Kinetic analysis of the binding*
1046 *of human matrix metalloproteinase-2 and -9 to tissue inhibitor of metalloproteinase (timp)-1 and*
1047 *timp-2*, The Journal of Biological Chemistry, 272 (1997), p. 29975–29983.
- 1048 [87] M. R. OWEN AND J. A. SHERRATT, *Mathematical modelling of macrophage dynamics in tumours*,
1049 Mathematical Models and Methods in Applied Sciences, 9 (1999), pp. 513–539.
- 1050 [88] T. K. PALANIAPPAN, L. ŠLEKIENĖ, A.-K. JONASSON, J. GILTHORPE, AND L. GUNHAGA, *Cam-*
1051 *delam: an in vivo approach to visualize and quantify the delamination and invasion capacity of*
1052 *human cancer cells*, Scientific Reports, 10 (2020), p. 10472.
- 1053 [89] J. PANOVSKA AND G. PETTET, *Mathematical model for glioma cell invasion*. Unpublished, 2007.
- 1054 [90] K. PAULA, T.-M. ANNE, AND T.-H. TAINA, *The sample type used affects the levels of gelatinases*
1055 *(mmp-2 and -9) and their inhibitors (timp-1 and -2) in circulating blood of healthy controls and*
1056 *breast cancer patients*, Biomarker Insights, 2 (2007), p. 117–127.

- 1057 [91] F. PIANOSI, K. BEVEN, J. FREER, J. W. HALL, J. ROUGIER, D. B. STEPHENSON, AND T. WA-
 1058 GENER, *Sensitivity analysis of environmental models: A systematic review with practical workflow*,
 1059 *Environmental Modelling & Software*, 79 (2016), pp. 214–232.
- 1060 [92] F. PIANOSI, F. SARRAZIN, AND T. WAGENER, *A matlab toolbox for global sensitivity analysis*,
 1061 *Environmental Modelling & Software*, 70 (2015), pp. 80–85.
- 1062 [93] M. PIIPPONEN, P. RIIHILÄ, L. NISSINEN, AND V.-M. KÄHÄRI, *The role of p53 in progression of*
 1063 *cutaneous squamous cell carcinoma*, *Cancers*, 13 (2021), p. 4507.
- 1064 [94] B. RIBBA, O. SAUT, T. COLIN, D. BRESCH, E. GRENIER, AND J. P. BOISSEL, *A multiscale*
 1065 *mathematical model of avascular tumor growth to investigate the therapeutic benefit of anti-invasive*
 1066 *agents*, *J. Theoret. Biol.*, 243 (2006), pp. 532–541.
- 1067 [95] R. C. ROCKNE, A. HAWKINS-DAARUD, K. R. SWANSON, J. P. SLUKA, J. A. GLAZIER, P. MACK-
 1068 LIN, D. A. HORMUTH, A. M. JARRETT, E. A. LIMA, J. T. ODEN, ET AL., *The 2019 mathematical*
 1069 *oncology roadmap*, *Physical biology*, 16 (2019), p. 041005.
- 1070 [96] E. ROIG-ROSELLO AND P. ROUSSELLE, *The human epidermal basement membrane: a shaped and*
 1071 *cell instructive platform that aging slowly alters*, *Biomolecules*, 10 (2020), p. 1607.
- 1072 [97] M. ROSE, *Evolutionary Biology of Aging*, Oxford University Press, 1994.
- 1073 [98] T. SAITOU, K. ITANO, D. HOSHINO, N. KOSHIKAWA, M. SEIKI, K. ICHIKAWA, AND T. SUZUKI,
 1074 *Control and inhibition analysis of complex formation processes*, *Theoretical Biology and Medical*
 1075 *Modelling*, 9 (2012), pp. 1–18.
- 1076 [99] N. SFAKIANAKIS AND M. A. J. CHAPLAIN, *Mathematical modelling of cancer invasion: A review*,
 1077 in *Methods of Mathematical Oncology*, T. Suzuki, C. Poignard, M. Chaplain, and V. Quaranta,
 1078 eds., vol. 370, Springer Singapore, Singapore, 2021, p. 153–172.
- 1079 [100] L. F. SHAMPINE AND M. W. REICHELDT, *The matlab ode suite*, *SIAM Journal on Scientific Com-*
 1080 *puting*, 18 (1997), pp. 1–22.
- 1081 [101] K.-I. SHIMOKAWA, M. KATAYAMA, Y. MATSUDA, H. TAKAHASHI, I. HARA, H. SATO, AND
 1082 S. KANEKO, *Matrix metalloproteinase (MMP)-2 and MMP-9 activities in human seminal plasma*,
 1083 *Molecular Human Reproduction*, 8 (2002), pp. 32–36.
- 1084 [102] W. G. STETLER-STEVENSON, *The tumor microenvironment: regulation by mmp-independent effects*
 1085 *of tissue inhibitor of metalloproteinases-2*, *Cancer and Metastasis Reviews*, 27 (2008), pp. 57–66.
- 1086 [103] S. SUVEGES, R. EFTIMIE, AND D. TRUCU, *Directionality of macrophages movement in tumour*
 1087 *invasion: A multiscale moving-boundary approach*, *Bulletin of Mathematical Biology*, 82 (2020),
 1088 pp. 1–50.
- 1089 [104] M. TAURO AND C. C. LYNCH, *Cutting to the chase: how matrix metalloproteinase-2 activity controls*
 1090 *breast-cancer-to-bone metastasis*, *Cancers*, 10 (2018), p. 185.
- 1091 [105] M. TOTH, M. M. BERNARDO, D. C. GERVAZI, P. D. SOLOWAY, Z. WANG, H. F. BIGG, C. M.
 1092 OVERALL, Y. A. DECLERCK, H. TSCHESCHE, M. L. CHER, ET AL., *Tissue inhibitor of metal-*
 1093 *loproteinase (timp)-2 acts synergistically with synthetic matrix metalloproteinase (mmp) inhibitors*
 1094 *but not with timp-4 to enhance the (membrane type 1)-mmp-dependent activation of pro-mmp-2*,
 1095 *Journal of Biological Chemistry*, 275 (2000), pp. 41415–41423.
- 1096 [106] T. H. VU AND Z. WERB, *Matrix metalloproteinases: effectors of development and normal physiol-*
 1097 *ogy*, *Genes & development*, 14 (2000), pp. 2123–2133.
- 1098 [107] T. WANG, F. NOTTA, R. NAVAB, J. JOSEPH, E. IBRAHIMOV, J. XU, C.-Q. ZHU, A. BORGIDA,
 1099 S. GALLINGER, AND M.-S. TSAO, *Senescent Carcinoma-Associated Fibroblasts Upregulate IL8 to*
 1100 *Enhance Prometastatic Phenotypes*, *Molecular Cancer Research*, 15 (2017), pp. 3–14.
- 1101 [108] H. E. V. WART AND H. BIRKEDAL-HANSEN, *The cysteine switch: a principle of regulation of*
 1102 *metalloproteinase activity with potential applicability to the entire matrix metalloproteinase gene*
 1103 *family.*, *Proceedings of the National Academy of Sciences*, 87 (1990), pp. 5578–5582.

- 1104 [109] A. WATANABE, D. HOSINO, N. KOSHIKAWA, M. SEIKI, T. SUZUKI, AND K. ICHIKAWA, *Critical*
1105 *role of transient activity of mt1-mmp for ecm degradation in invadopodia*, PLOS Computational
1106 Biology, 9 (2013), pp. 1–13.
- 1107 [110] M. C. WHITE, D. M. HOLMAN, J. E. BOEHM, L. A. PEIPINS, M. GROSSMAN, AND S. J. HENLEY,
1108 *Age and cancer risk: a potentially modifiable relationship*, American journal of preventive medicine,
1109 46 (2014), pp. S7–S15.
- 1110 [111] E. C. WOENNE, W. LEDERLE, S. ZWICK, M. PALMOWSKI, H. KRELL, W. SEMMLER, M. M.
1111 MUELLER, AND F. KIESSLING, *Mmp inhibition blocks fibroblast-dependent skin cancer invasion,*
1112 *reduces vascularization and alters vegf-a and pdgf-bb expression*, Anticancer Research, 30 (2010),
1113 pp. 703–711.
- 1114 [112] C. WU, G. LORENZO, D. A. HORMUTH, E. A. B. F. LIMA, K. P. SLAVKOVA, J. C. DI-
1115 CARLO, J. VIROSTKO, C. M. PHILLIPS, D. PATT, C. CHUNG, AND T. E. YANKEELOV, *Integrating*
1116 *mechanism-based modeling with biomedical imaging to build practical digital twins for clinical oncol-*
1117 *ogy*, Biophysics Reviews, 3 (2022), p. 021304.

1118 A Mathematical notation and derivation of the model

1119 A.1 Original system

1120 **Notation.** We consider a general function $u(x, t)$ depending on space $x \in \mathbb{R}^d$ ($d = 1, 2, 3$, we choose
1121 $d = 3$ in this section) and time $t \in [0, T]$ ($T > 0$ a positive finite time horizon). We denote by $\partial_t u$ the
1122 partial derivative of u with respect to time and $\nabla u = (\partial_{x_1} u, \partial_{x_2} u, \partial_{x_3} u)$ the gradient of u in space. We
1123 denote by $\Delta u = \text{div}(\nabla u) = \partial_{x_1 x_1}^2 u + \partial_{x_2 x_2}^2 u + \partial_{x_3 x_3}^2 u$ the laplacian of u , with $\text{div}(\vec{v}) = \partial_{x_1} v_1 + \partial_{x_2} v_2 + \partial_{x_3} v_3$
1124 the divergence of the vector field $\vec{v} = (v_1, v_2, v_3)$.

1125 **Full system.** In this section, we introduce the mathematical model comprising a system of PDEs describ-
1126 ing the dynamics of the SFs’ secretome in the CT, with boundary conditions modelling the transmission
1127 of these concentrations to the BM, and a system of PDEs describing the activation and degradation dy-
1128 namics in the BM. Details about the modelling assumptions and the notations for the different unknowns
1129 can be found in Section 2.

1130 We start with two domains, *i.e.* smooth bounded open subsets, $\Omega_{\text{CT}}, \Omega_{\text{BM}} \subset \mathbb{R}^d$, separated by a “mem-
1131 brane” denoted by Γ . We highlight that Γ simply models the boundary separating the two domains and
1132 not a real physical membrane with a positive thickness. We have the following system of equations

$$\partial_t \bar{c}_t = \bar{D}_t \Delta \bar{c}_t + \bar{S}_t(x) - \beta_t \bar{c}_t, \quad \text{in } \Omega_{\text{CT}} \times (0, T), \quad (\text{A.1})$$

$$\partial_t \bar{c}_p = \bar{D}_p \Delta \bar{c}_p + \bar{S}_p(x) - \beta_p \bar{c}_p, \quad \text{in } \Omega_{\text{CT}} \times (0, T), \quad (\text{A.2})$$

$$\bar{c}_t = c_t, \quad \text{on } \Gamma \times (0, T), \quad (\text{A.3})$$

$$\bar{c}_p = c_p, \quad \text{on } \Gamma \times (0, T), \quad (\text{A.4})$$

$$\bar{D}_t \nabla \bar{c}_t \cdot \nu = D_t^{\text{BM}} \nabla c_t \cdot \nu, \quad \text{on } \Gamma \times (0, T), \quad (\text{A.5})$$

$$\bar{D}_p \nabla \bar{c}_p \cdot \nu = D_p^{\text{BM}} \nabla c_p \cdot \nu, \quad \text{on } \Gamma \times (0, T), \quad (\text{A.6})$$

$$\partial_t c_t = D_t^{\text{BM}} \Delta c_t + R_t(x, t) - \beta_t c_t, \quad \text{in } \Omega_{\text{BM}} \times (0, T), \quad (\text{A.7})$$

$$\partial_t c_p = D_p^{\text{BM}} \Delta c_p + R_p(x, t) - \beta_p c_p, \quad \text{in } \Omega_{\text{BM}} \times (0, T), \quad (\text{A.8})$$

1133 with ν the unit normal vector to Γ that points from the BM to the CT. The rest of the boundary conditions
1134 on $\partial\Omega_{\text{CT}} \setminus \Gamma \times (0, T)$ and $\partial\Omega_{\text{BM}} \setminus \Gamma \times (0, T)$ are set to zero-flux boundary conditions.

1135 Equations (A.3)–(A.6) are transmission conditions modeling the diffusion of TIMP-2 and proMMP-2
1136 between the CT and the BM. In particular, Equations (A.3)–(A.4) model continuity of the concentration
1137 at the border between the two domains, and equations (A.5)–(A.6) model the continuity of the flux across
1138 this interface. Moreover, while the terms $\bar{S}_t(x)$ and $\bar{S}_p(x)$ in equations (A.1)–(A.2) are as defined in (2.15),
1139 the terms $R_t(x, t)$ and $R_p(x, t)$ in equations (A.7)–(A.8) include the biochemical reactions terms. Namely,
1140 we have

$$R_t(x, t) = -c_t[k_1(c_d + c_1) + k_2(c_p + c_a)] + k_{-1}(c_1 + c_3) + k_{-2}(c_{tp} + c_{ta}), \quad (\text{A.9})$$

$$R_p(x, t) = -k_2 c_p(c_t + c_1) + k_{-2}(c_{tp} + c_2). \quad (\text{A.10})$$

1141 Equations (A.1)-(A.8) are coupled, via the reaction terms $R_i(t, x)$, $i = \{t, p\}$, with the rest of the
 1142 system modelling proMMP-2 activation, BM digestion and TIMP-mediated MMP inhibition: assuming
 1143 the diffusion of the rest of the components is negligible, we have

$$\begin{aligned}
 \partial_t M &= -\gamma c_a \frac{M}{K_m + M} + r_M \left(1 - \frac{M}{M_{\max}}\right)_+, & \text{in } \Omega_{\text{BM}} \times (0, T), \\
 \partial_t c_m &= \alpha_m \rho^0 - k_0 c_m^2 + k_{-0} c_d - \beta_m c_m, & \text{in } \Omega_{\text{BM}} \times (0, T), \\
 \partial_t c_d &= k_0 c_m^2 - k_{-0} c_d - k_1 c_d c_t + k_{-1} c_1 - \beta_d c_d, & \text{in } \Omega_{\text{BM}} \times (0, T), \\
 \partial_t c_a &= k_3 c_2 - k_2 c_t c_a + k_{-2} c_{ta} - \beta_a c_a, & \text{in } \Omega_{\text{BM}} \times (0, T), \\
 \partial_t c_1 &= k_1 c_d c_t - c_1 [k_1 c_t + k_2 c_p] + k_{-1} (c_3 - c_1) + (k_{-2} + k_3) c_2 - \beta_1 c_1, & \text{in } \Omega_{\text{BM}} \times (0, T), \\
 \partial_t c_2 &= k_2 c_1 c_p - (k_{-2} + k_3) c_2 - \beta_2 c_2, & \text{in } \Omega_{\text{BM}} \times (0, T), \\
 \partial_t c_3 &= k_1 c_1 c_t - k_{-1} c_3 - \beta_3 c_2, & \text{in } \Omega_{\text{BM}} \times (0, T), \\
 \partial_t c_{tp} &= k_2 c_t c_p - k_{-2} c_{tp} - \beta_{tp} c_{tp}, & \text{in } \Omega_{\text{BM}} \times (0, T), \\
 \partial_t c_{ta} &= k_2 c_t c_a - k_{-2} c_{ta} - \beta_{ta} c_{ta}, & \text{in } \Omega_{\text{BM}} \times (0, T).
 \end{aligned}$$

1144 A.2 Dimension reduction of the BM

1145 In order to improve computational tractability of our model, as the BM is a very thin structure compared
 1146 to the rest of the tissue [7], we reduce the dimension of Ω_{BM} , which then becomes a subset of \mathbb{R}^{d-1}
 1147 (whereas $\Omega_{\text{CT}} \subset \mathbb{R}^d$). We do this following a simple and formal dimension reduction procedure, inspired
 1148 by ideas from [74] to derive 1D-3D coupled problems.

1149 **Smallness assumptions and decomposition.** We introduce a small parameter $0 < \varepsilon \ll 1$ describing
 1150 the thickness of the BM, *i.e.* $\bar{\Omega}_{\text{BM}} = \Gamma \times [0, \varepsilon]$. Assuming Γ is a flat surface, we consider that $\forall x \in \bar{\Omega}_{\text{BM}}$, x
 1151 is defined by $x := (x_1, x_2, x_3)$ with $(x_1, x_3) \in \Gamma$ and $x_2 = \varepsilon \bar{x}_2$, ($\bar{x}_2 \in (0, 1)$), coherently with the coordinate
 1152 system adopted in Section 2 and illustrated in Figure 2. We decompose the concentrations c_i as

$$c_i(x_1, x_2, x_3, t) = \hat{c}_i(x_1, x_3, t) + \tilde{c}_i(x_1, x_2, x_3, t) \quad \text{for } i = \{t, p, d, tp, ta, 1, 2, 3\}, \quad (\text{A.11})$$

1153 where $\hat{c}_i(x_1, x_3, t)$ corresponds to the average of the concentration in the x_2 direction, *i.e.*

$$\hat{c}_i = \frac{1}{\varepsilon} \int_0^\varepsilon c_i \, dx_2 = \int_0^1 c_i(\varepsilon \bar{x}_2) \, d\bar{x}_2, \quad (\text{A.12})$$

1154 and $\tilde{c}_i(x_1, x_2, x_3, t)$ is a fluctuation around this average. Integrating both sides of the decomposition (A.11)
 1155 along the width of the BM (*i.e.* the x_2 direction) and using the definition (A.12) of the average \hat{c}_i , we
 1156 obtain that the fluctuation must satisfy

$$\int_0^\varepsilon \tilde{c}_i \, dx_2 = 0.$$

1157 We assume that the fluctuations are small and that the concentration fields evolve smoothly within the
 1158 BM, *i.e.* spatial derivatives of the fluctuations in the BM are small.

1159 Under assumption (A.11) and definitions (A.9)-(A.10), we have that both sources R_i ($i = \{t, p\}$)
 1160 in (A.7) and (A.8) also admit a decomposition in the form (A.11).

1161 **Simplified dynamics in the BM.** Since we assumed that the fluctuation of the concentrations within
 1162 the BM – *i.e.* \tilde{c}_i in (A.11) – are small, we simplify the dynamics in the BM by focusing on the evolution of
 1163 the averages of the concentration fields in the BM along the x_2 direction (*i.e.* along the width of the BM)
 1164 – *i.e.* \hat{c}_i defined in (A.12). This will allow us to drop the dependency on x_2 of the dynamics, providing
 1165 an approximation that is well suited for a model in which the dimensionality of the BM is reduced to
 1166 $d - 1$. Given that the thickness of the BM is very small, we expect that the diffusion of the enzymes in
 1167 the x_2 direction will have a strong impact on the average concentration \hat{c}_i , while we assume diffusion in
 1168 the (x_1, x_3) plane (*i.e.* tangential to Γ) is negligible.

1169 Integrating Equations (A.7)-(A.8) with respect to x_2 , dividing by ε , and neglecting the diffusion in
 1170 the tangential plane (x_1, x_3) , we obtain for any $(x_1, x_3) \in \Gamma$ and $t \in (0, T)$

$$\frac{1}{\varepsilon} \int_0^\varepsilon \partial_t c_i \, dx_2 - \frac{D_i^{\text{BM}}}{\varepsilon} \left[\nabla c_i \cdot \nu \Big|_{x_2=\varepsilon} - \nabla c_i \cdot \nu \Big|_{x_2=0} \right] = \frac{1}{\varepsilon} \int_0^\varepsilon R_i - \beta_i c_i \, dx_2,$$

1171 where we used the divergence theorem, with ν being the outward normal to $\partial\Omega_{\text{BM}}$. Since we assumed
 1172 zero-flux boundary conditions on $\partial\Omega_{\text{BM}} \setminus \Gamma \times (0, T)$ and using the definition (A.12), we have

$$\partial_t \hat{c}_i + \frac{D_i^{\text{BM}}}{\varepsilon} \partial_{x_2} c_i(x_1, 0, x_3, t) \cdot \nu = \hat{R}_i - \beta_i \hat{c}_i, \quad (\text{A.13})$$

1173 for $i = \{t, p\}$. We note that the directional derivative $\partial_{x_2} c_i(x_1, 0, x_3, t) \cdot \nu$ also appears on the right-hand-
 1174 side of (A.5)–(A.6).

1175 **Approximation of concentration gradients at the interface.** We now construct an approximation
 1176 of $\partial_{x_2} c_i(x_1, 0, x_3, t)$ for $i = \{t, p\}$. Since ε is small, assuming c_i is sufficiently smooth to allow a Taylor
 1177 series approximation, we consider the following expansion around $x_2 = 0$

$$c_i(x_1, \varepsilon, x_3, t) = c_i(x_1, 0, x_3, t) + \varepsilon \partial_{x_2} c_i(x_1, 0, x_3, t) + \mathcal{O}(\varepsilon^2).$$

1178 Using this, we know that the following holds

$$\partial_{x_2} c_i(x_1, 0, x_3, t) = \frac{c_i(x_1, \varepsilon, x_3, t) - c_i(x_1, 0, x_3, t)}{\varepsilon} + \mathcal{O}(\varepsilon).$$

1179 Using the continuity of concentrations (A.3)–(A.4) at the interface Γ , and the decomposition (A.11) at
 1180 $x_2 = \varepsilon$, we rewrite this as

$$\partial_{x_2} c_i(x_1, 0, x_3, t) = \frac{\hat{c}_i(x_1, x_3, t) - \bar{c}_i(x_1, 0, x_3, t)}{\varepsilon} + \frac{\tilde{c}_i(x_1, \varepsilon, x_3, t)}{\varepsilon} + \mathcal{O}(\varepsilon).$$

1181 We approximate $\tilde{c}_i(x_1, \varepsilon, x_3, t)$ as

$$\tilde{c}_i(x_1, \varepsilon, x_3, t) = (C_\varepsilon^i - 1)(\hat{c}_i(x_1, x_3, t) - \bar{c}_i(x_1, 0, x_3, t)),$$

1182 with constant $C_\varepsilon^i > 0$ for $\varepsilon > 0$. Thus, for ε small, we have

$$\partial_{x_2} c_i(x_1, 0, x_3) \approx C_\varepsilon^i \frac{\hat{c}_i(x_1, x_3) - \bar{c}_i(x_1, 0, x_3)}{\varepsilon} \quad \text{for } i = \{t, p\}. \quad (\text{A.14})$$

1183 This approximation is justified by the fact that the c_i ($i = \{t, p\}$) satisfy a reaction-diffusion equation in a
 1184 thin domain, with Dirichlet boundary conditions on Γ and zero-flux boundary conditions at the other end
 1185 of the domain. At equilibrium, this leads to a concentration profile along the x_2 direction analogous to
 1186 the one shown in Figure 9, where we simulated this scenario in 1D (with Γ the left boundary) and tested
 1187 the approximation (A.14) for different values of C_ε^i . We clearly have that $C_\varepsilon^i > 0$ for $\varepsilon > 0$ (analogous
 1188 profiles were obtained for decreasing values of the domain size).

1189 **Dimension reduction.** Substituting the approximation (A.14) in (A.13), we obtain the equations for
 1190 the evolution of the average quantities

$$\partial_t \hat{c}_i + \frac{D_i^{\text{BM}}}{\varepsilon^2} C_\varepsilon^i (\hat{c}_i - \bar{c}_i(x_1, 0, x_3)) = \hat{R}_i - \beta_i \hat{c}_i, \quad (\text{A.15})$$

1191 with $i = \{t, p\}$. Analogously, approximation (A.14) can be introduced in (A.5) and (A.6).

1192 As this quantity is constant along the x_2 axis and its computation only involves the knowledge of the
 1193 concentrations on Γ , we can reduce the dimension of Ω_{BM} and use only Γ as the "BM" domain.

1194 **Physical considerations and transmission coefficients.** While in a rigorous dimension reduction
 1195 procedure one needs to consider the limit $\varepsilon \rightarrow 0$, we keep the ε -dependency in (A.15) in order to incorporate
 1196 information on the thickness of the BM into the rates at which different enzymes cross this membrane.

1197 We consider a BM width $\varepsilon = 2 \times 10^{-6}$ dm, the average value measured by new experimental techniques
 1198 as reported in [96]. The diffusion coefficients of TIMP-2 and proMMP-2 within the ECM of the CT, *i.e.* \bar{D}_i ,
 1199 estimated in [22] are of about 1.29×10^{-6} dm²/s. In the absence of empirical measurements or estimation
 1200 of the diffusivity of these molecules within the BM, we consider that the much higher density of ECM in
 1201 the BM compared to that in the CT drastically reduces molecular diffusion rates of these molecules in the
 1202 BM, and we assume that $D_i^{\text{BM}} \approx \mathcal{O}(\varepsilon^2/s)$.

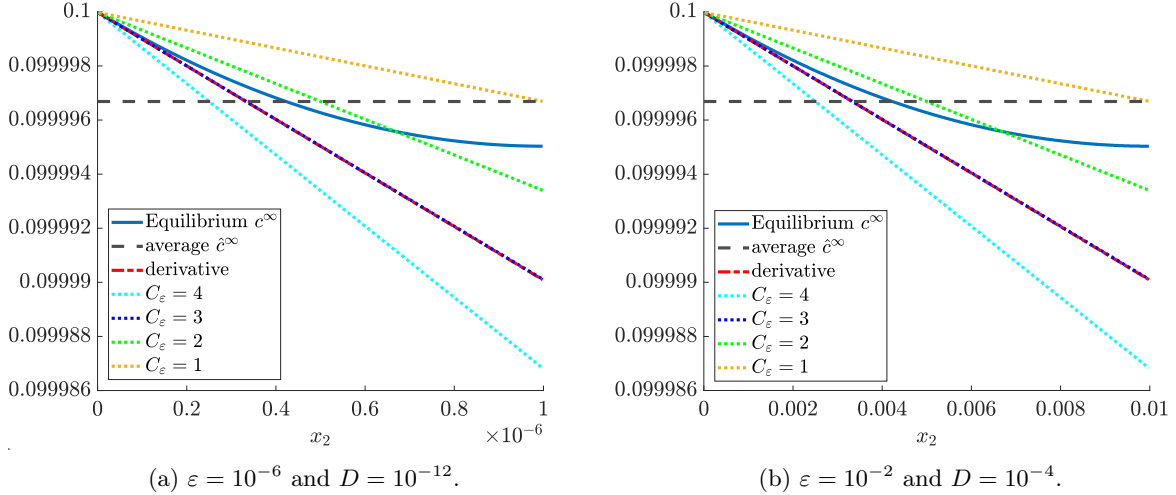


Figure 9: **Illustration of the best C_ε to approximate the derivative.** We compute the analytical solution of the equation $\partial_t c = D\Delta c - \beta c$ in the 1D domain $[0, \varepsilon]$ at steady-state, with $\beta = 10^{-4}$ and $D = \varepsilon^2$, using $\varepsilon = 10^{-6}$ (a, left) and $\varepsilon = 10^{-2}$ (b, right). The equation is supplemented with Dirichlet boundary condition on the left boundary $c(t, 0) = \bar{c} = 0.1$ and zero-flux boundary condition on the right boundary. The steady state of the problem, *i.e.* $c^\infty(x_2)$ satisfying $D\Delta c^\infty = \beta c^\infty$, is plotted in a solid blue line. The dashed black line marks \hat{c}^∞ , *i.e.* the average of c^∞ in the domain. The red dashed-dotted line corresponds to the derivative of c^∞ at $x_2 = 0$. The colored dashed lines display different approximations of this derivative using the formula $\partial_{x_2} c^\infty(0) \approx C_\varepsilon(\hat{c}^\infty - \bar{c})/\varepsilon$, *i.e.* the equivalent of (A.14), for different values of C_ε : $C_\varepsilon = 1$ (yellow dotted line), $C_\varepsilon = 2$ (green dotted line), $C_\varepsilon = 3$ (blue dotted line), and $C_\varepsilon = 4$ (cyan dotted line). Analogous results were obtained varying the grid size, the parameter \bar{c} , and ε maintaining the relation $D = \varepsilon^2$. Similar results were obtained varying $\beta \in [0, 10^{-3}]$, although larger values deteriorate the quality of the derivative approximation with $C_\varepsilon = 3$. This deterioration is also observed varying ε or D independently of each other, hence breaking the proportionality relation $D \propto \varepsilon^2$.

We note that while the value of C_ε^i may vary as ε or D_i^{BM} vary independently, varying ε while maintaining the proportionality relation $D_i^{\text{BM}} \propto \varepsilon^2$ does not change the value of C_ε^i providing the best approximation using (A.14) (cf. Figure 9, for which up to 16 orders of magnitude were tested for ε).

We introduce the following parameters: the diffusive permeability of the molecule denoted by the index i across the BM (crossing the BM in the x_2 direction) κ_i , and the corresponding transmission rate of the molecule to the BM $\hat{\kappa}_i$, defined as

$$\kappa_i = \frac{C_\varepsilon^i D_i^{\text{BM}}}{\varepsilon} \quad \text{and} \quad \hat{\kappa}_i = \frac{\kappa_i}{\varepsilon} = \frac{C_\varepsilon^i D_i^{\text{BM}}}{\varepsilon^2}, \quad i = \{t, p\}. \quad (\text{A.16})$$

Remark 3. We emphasise that our method is formal and we do not send $\varepsilon \rightarrow 0$, but only retain the dynamics of the average concentration along the direction selected for dimensionality reduction, assuming that ε , *i.e.* the BM width, is very small.

Remark 4. While we adopt a formal method for the dimension reduction of the BM, rigorous methods yielding analogous results have been developed – we refer the interested reader to the method of two-scale convergence for dimension reduction problems, *e.g.* see [82]. However, we also mention that in other models modelling the effect of thin membranes, transmission is modelled as Kedem-Katchalsky conditions, in which the flux is computed from the permeability and the concentration difference between the sides of the membrane. Here, using this formal dimension reduction, we retain an information about the average of these quantities in the BM in a simple manner.

Summary of the full reduced model. Altogether, using the bar notation to denote concentrations in the CT Ω_{CT} and the hat notation to denote the concentrations in the BM $\Omega_{\text{BM}} \equiv \Gamma$ (which in now an

1221 open subset of \mathbb{R}^{d-1}), we have the model

$$\begin{aligned}
\partial_t \bar{c}_t &= \bar{D}_t \Delta \bar{c}_t + \bar{S}_t(x) - \beta_t \bar{c}_t, & \text{in } \Omega_{\text{CT}} \times (0, T), \\
\partial_t \bar{c}_p &= \bar{D}_p \Delta \bar{c}_p + \bar{S}_p(x) - \beta_p \bar{c}_p, & \text{in } \Omega_{\text{CT}} \times (0, T), \\
-\bar{D}_t \nabla \bar{c}_t \cdot \nu &= \kappa_t (\bar{c}_t - \hat{c}_t), & \text{on } \Gamma \times (0, T), \\
-\bar{D}_p \nabla \bar{c}_p \cdot \nu &= \kappa_p (\bar{c}_p - \hat{c}_p), & \text{on } \Gamma \times (0, T), \\
\partial_t \hat{c}_t &= \hat{\kappa}_t (\bar{c}_t - \hat{c}_t) + \hat{R}_t - \beta_t \hat{c}_t, & \text{in } \Gamma \times (0, T), \\
\partial_t \hat{c}_p &= \hat{\kappa}_p (\bar{c}_p - \hat{c}_p) + \hat{R}_p - \beta_p \hat{c}_p, & \text{in } \Gamma \times (0, T), \\
\partial_t \hat{M} &= -\gamma \hat{c}_a \frac{\hat{M}}{K_m + \hat{M}} + r_M \left(1 - \frac{\hat{M}}{M_{\max}} \right)_+, & \text{in } \Gamma \times (0, T), \\
\partial_t \hat{c}_m &= \alpha_m \hat{\rho}^0 - k_0 \hat{c}_m^2 + k_{-0} \hat{c}_d - \beta_m \hat{c}_m, & \text{in } \Gamma \times (0, T), \\
\partial_t \hat{c}_d &= k_0 \hat{c}_m^2 - k_{-0} \hat{c}_d - k_1 \hat{c}_d \hat{c}_t + k_{-1} \hat{c}_1 - \beta_d \hat{c}_d, & \text{in } \Gamma \times (0, T), \\
\partial_t \hat{c}_a &= k_3 \hat{c}_2 - k_2 \hat{c}_t \hat{c}_a + k_{-2} \hat{c}_{ta} - \beta_a \hat{c}_a, & \text{in } \Gamma \times (0, T), \\
\partial_t \hat{c}_1 &= k_1 \hat{c}_d \hat{c}_t - \hat{c}_1 [k_1 \hat{c}_t + k_2 \hat{c}_p] + k_{-1} (\hat{c}_3 - \hat{c}_1) + (k_{-2} + k_3) \hat{c}_2 - \beta_1 \hat{c}_1, & \text{in } \Gamma \times (0, T), \\
\partial_t \hat{c}_2 &= k_2 \hat{c}_1 \hat{c}_p - (k_{-2} + k_3) \hat{c}_2 - \beta_2 \hat{c}_2, & \text{in } \Gamma \times (0, T), \\
\partial_t \hat{c}_3 &= k_1 \hat{c}_1 \hat{c}_t - k_{-1} \hat{c}_3 - \beta_3 \hat{c}_3, & \text{in } \Gamma \times (0, T), \\
\partial_t \hat{c}_{tp} &= k_2 \hat{c}_t \hat{c}_p - k_{-2} \hat{c}_{tp} - \beta_{tp} \hat{c}_{tp}, & \text{in } \Gamma \times (0, T), \\
\partial_t \hat{c}_{ta} &= k_2 \hat{c}_t \hat{c}_a - k_{-2} \hat{c}_{ta} - \beta_{ta} \hat{c}_{ta}, & \text{in } \Gamma \times (0, T).
\end{aligned}$$

1222 We note that in Section 2 the hat is dropped for convenience, while $\hat{\kappa}_i(\bar{c}_i - \hat{c}_i) = S_i(x, t)$ and the remaining
1223 biochemical reaction terms introduced in equations (2.4) and (2.5) are denoted by \hat{R}_i .

1224 B Computation details of biologically relevant parameter values

1225 Most baseline parameter values reported in Table 1 are found directly in the literature, short of a change
1226 of unit to fit our reference system when required. These come from experimental measurements, were
1227 computed using a computational model (different from ours), or were estimated to fit a relevant range.
1228 As we use multiple sources to find *a priori* values for the parameters, we refine our parameter set using
1229 optimization techniques to ensure that the outputs of our model are biologically consistent. Below we give
1230 details of the references used and computations performed to estimate parameter values which were not
1231 found in the literature (marked with a * in Table 1).

1232 **BM carrying capacity.** The BM carrying capacity M_{\max} represents the maximum ECM density in the
1233 BM. We consider the BM matrigel density used in *in vitro* invasion assays reported in [2], whose authors
1234 estimated a protein concentration of about 10 mg/ml. Considering a molecular weight in the typical
1235 weight range of collagen IV, the main component of the ECM found in the BM, *i.e.* about 160kDa [75],
1236 we compute

$$M_{\max} = \frac{10 \text{ mg/ml}}{160 \times 10^3 \text{ Da}} \approx 6.2510^{-5} \text{ mol/dm}^3 = 62.5 \times 10^3 \text{ nM}.$$

1237 **Physiological levels of TIMP-2, proMMP-2, active MMP-2 and TIMP-2/MMP-2 complex.**
1238 We use as reference, the serum levels reported in [90] for TIMP-2, proMMP-2, active MMP-2 and TIMP-
1239 2/MMP-2 complex, which are in good agreement with the values reported by recent studies. Knowing the
1240 molecular masses of TIMP-2 (21 kDa, see *e.g.* [102] and references therein), proMMP-2 (72 kDa [101]),
1241 active MMP-2 (67 kDa [101]), and the complex TIMP-2/MMP-2 (88kDa, sum of the two free proteins),

1242 we compute the physiological molar concentrations

$$\begin{aligned}
c_t^{\text{ph}} &= \frac{201.8 \text{ ng/cm}^3}{21 \times 10^3 \text{ Da}} \approx 9.6 \text{ nmol/dm}^3 = 9.6 \text{ nM} \\
c_p^{\text{ph}} &= \frac{1259.9 \text{ ng/cm}^3}{72 \times 10^3 \text{ Da}} \approx 18 \text{ nM}, \\
c_a^{\text{ph}} &= \frac{29.4 \text{ ng/cm}^3}{67 \times 10^3 \text{ Da}} \approx 0.44 \text{ nM}, \\
c_{ta}^{\text{ph}} &= \frac{1456.4 \text{ ng/cm}^3}{88 \times 10^3 \text{ Da}} \approx 17 \text{ nM}.
\end{aligned}$$

1243 For the level of TIMP-2/proMMP-2 c_{tp}^* , we use the value reported in [4] and obtain

$$c_{tp}^{\text{ph}} = \frac{625 \times 10^3 \text{ ng/L}}{93 \times 10^3 \text{ Da}} \approx 6.72 \text{ nM}.$$

1244 For the reduced model, detailed in Appendix A, we assume equilibrium level of MT1-MMP dimers are
1245 given. With analogous calculations to those reported above, we take this to be $\bar{c}_d = 8.55/(63 \times 10^3) \approx 0.14$
1246 nM, from normal serum concentration of MT1-MMP given in [73] and molecular mass in [20].

1247 **Remark 5.** *In the review article [51], the authors survey the different values of the level of MMP-*
1248 *2, proMMP-2, TIMP-2 and the complex TIMP-2/MMP-2. We observe that, from one study to another,*
1249 *discrepancies in serum or plasma levels of the proteins are found, which could be due to different techniques*
1250 *used to measure these quantities but also due to differences in the cohort. The chosen reference publication*
1251 *for the baseline parameter values used here ensures higher consistency in origin and measurement technique*
1252 *among these values. Moreover, as already mentioned, these values are in good agreement with those*
1253 *reported by recent studies.*

1254 **Remark 6.** *It is worth mentioning that we use measurements in blood and transpose the values to tissue*
1255 *concentrations. This may be untrue and most probably the values depend on the tissue. However, as we*
1256 *were unable to find measurements in tissue samples, we use these values for the moment.*

1257 **Physiological production rate of proMMP-2 and TIMP-2 in the CT.** We assume the physio-
1258 logical concentrations of TIMP-2 and pro-MMP2 for a healthy patient are equivalent to the equilibria c_i^*
1259 ($i = \{t, p\}$) of their dynamics in the CT (2.13)–(2.12) in the absence of SFs. This yields the relation

$$c_i^{\text{ph}} = \bar{c}_i^* = \frac{s_i^{\text{ph}}}{\beta_i}, \quad i = \{t, p\}.$$

1260 Using the values for decay rates and physiological levels reported in Table 1, we find

$$\begin{aligned}
s_p^{\text{ph}} &= 1.09 \times 10^{-2} \text{ nM/s}, \\
s_t^{\text{ph}} &= 4.28 \times 10^{-4} \text{ nM/s}.
\end{aligned}$$

1261 **Molecular decay rates.** Decay rates β_i in System (2.1)–(2.12) represent molecular natural decay, but
1262 may also capture the effect of molecule degradation and internalization by other actors, *e.g.* internalization
1263 of membrane bound MT1-MMP [60], or internalization of TIMP-2/proMMP-2 [32]. We assume the decay
1264 rates of MT1-MMP dimers and complexes match the one of MT1-MMP monomers, for which we use the
1265 rate of MT1-MMP internalization estimated in [55].

1266 We assume physiological levels of TIMP-2/proMMP-2 and TIMP-2/MMP-2 complexes correspond to
1267 their concentrations at the equilibrium of system (2.1)–(2.13) in the absence of SFs. We estimate their
1268 decay rates from the equilibrium of equations (2.10)–(2.11), using the reaction rates indicated in Table 1,
1269 obtaining

$$\begin{aligned}
\beta_{tp} &= \frac{k_2 c_t^* c_p^*}{c_{tp}^*} - k_{-2} = \frac{k_2 c_t^{\text{ph}} c_p^{\text{ph}}}{c_{tp}^{\text{ph}}} - k_{-2} = 3.60 \text{ s}^{-1}, \\
\beta_{ta} &= \frac{k_2 c_t^* c_a^*}{c_{ta}^*} - k_{-2} = \frac{k_2 c_t^{\text{ph}} c_a^{\text{ph}}}{c_{ta}^{\text{ph}}} - k_{-2} = 0.035 \text{ s}^{-1}.
\end{aligned}$$

1270 The other decay rates, assumed to model natural decay, are computed from the half-life $t_{i,1/2}$ of the
 1271 molecule via the formula $\beta_i = \ln(2)/t_{i,1/2}$. We know from [15] that the half-life of TIMP-2 in blood is
 1272 $t_{t,1/2} = 4.33$ hours, and compute

$$\beta_t = \frac{\ln(2)}{4.33 \times 3600} \approx 4.45 \times 10^{-5} \text{ s}^{-1}.$$

1273 In [83], the authors reported a half-life in the plasma of $t_{p,1/2} = 19$ min for human recombinant proMMP-2
 1274 injected in mice deficient in MMP-2. As reported in [25], active MMP-9 has a shorter half-life compared
 1275 to the pro and inactive enzyme. Hence, we assume that $t_{a,1/2} = 0.5t_{p,1/2} = 9.5$ min. This gives the
 1276 coefficients

$$\beta_p = \frac{\ln(2)}{19 \times 60} \approx 6.08 \times 10^{-4} \text{ s}^{-1},$$

1277 and

$$\beta_a = \frac{\ln(2)}{9.5 \times 60} \approx 1.22 \times 10^{-3} \text{ s}^{-1}.$$

1278 **Diffusive permeabilities and transmission rates at the BM.** As detailed in Appendix A, we
 1279 consider a BM of width $\varepsilon = 2 \times 10^{-6}$ dm, estimated for the human epidermal BM via new measuring
 1280 techniques, as reported in [96]. We consider diffusion coefficients of TIMP-2 and proMMP-2 within the
 1281 ECM of the CT estimated in [22], *i.e.* $\bar{D}_i = 1.29 \times 10^{-6}$ dm²/s. Given the much higher density of ECM in
 1282 the BM compared to that in the CT, we take the diffusivity of TIMP-2 and proMMP-2 in the BM to be
 1283 $D_i^{\text{BM}} = 1.29 \times 10^{-12}$ dm²/s. This is consistent with the assumption that $D_i^{\text{BM}} \approx \mathcal{O}(\varepsilon^2/s)$ (while \bar{D}_i is of
 1284 the order of ε). Finally, to estimate the diffusive permeability of TIMP-2 and proMMP-2 in the BM, κ_i ,
 1285 and their transmission rate across the BM, $\hat{\kappa}_i$, using definitions (A.16), we take $C_\varepsilon^i = 3$. The best value
 1286 to use for this parameter, introduced in the approximation of the concentration gradient in (A.14), was
 1287 investigated numerically (see Figure 9) Altogether this gives

$$\kappa_i = \frac{3 \times 1.29 \times 10^{-12} \text{ dm}^2}{2 \times 10^{-6} \text{ dm}} \approx 1.935 \times 10^{-6} \text{ dm/s},$$

1288 and

$$\hat{\kappa}_i = \frac{3 \times 1.29 \times 10^{-12} \text{ dm}^2}{4 \times 10^{-12} \text{ dm}^2} \approx 0.9675 \text{ s}^{-1}.$$

1289 C Reduced system and analytical results

1290 We reduce System (2.1)–(2.11), comprising 11 coupled nonlinear equations, to an analytically tractable
 1291 model that retains the key biological processes under consideration. We then study the stability of this
 1292 reduced system and derive necessary conditions for BM rupture, *i.e.* tumour invasion.

1293 **Simplifying assumptions.** We make the following simplifying assumptions:

- 1294 SA1. the inhibition of proMMP-2 and active MMP-2 by TIMP-2 can not reverse (*i.e.* we take $k_{-2}c_{tp} =$
 1295 $k_{-2}c_{ta} \approx 0$ in Equations (2.4)–(2.6) and (2.10)–(2.11));
- 1296 SA2. the activation and inhibition of proMMP-2 are very fast compared to the rest of the dynamics (hence,
 1297 we use the quasi steady-state assumption in Equations (2.7)–(2.11));
- 1298 SA3. stable MT1-MMP expression by cancer cells is already in place and MT1-MMP dimerisation occurs
 1299 rapidly, so that MT1-MMP dimers quickly stabilize to some equilibrium value \bar{c}_d , which is kept
 1300 constant henceforth;
- 1301 SA4. the natural decay of proMMP-2, TIMP-2 and active MMP-2 inside the BM is negligible compared
 1302 to the faster activation/degradation dynamics they are involved in (*i.e.* we take $\beta_p = \beta_t = \beta_a \approx 0$
 1303 in Equations (2.4)–(2.6)).

1304 **Reduced model.** Under these assumptions, System (2.1)–(2.11) reduces to the System (2.25)–(2.27),
 1305 *i.e.*

$$\begin{aligned}\frac{dc_t}{dt} &= \hat{\kappa}_t \bar{c}_t - k_2 c_t (c_p + c_a) - \hat{\kappa}_t c_t, \\ \frac{dc_p}{dt} &= \hat{\kappa}_p \bar{c}_p - k_2 c_p c_t \left(1 + \frac{k_1 k_3}{k_{-1}(k_{-2} + k_3)} \bar{c}_d \right) - \hat{\kappa}_p c_p, \\ \frac{dc_a}{dt} &= \frac{k_1 k_2 k_3}{k_{-1}(k_{-2} + k_3)} \bar{c}_d c_t c_p - k_2 c_t c_a,\end{aligned}$$

1306 where we have introduced the notation $\bar{c}_i \equiv \bar{c}_i(x, t)|_\Gamma$ ($i = \{t, p\}$) for the TIMP-2 and proMMP-2 concen-
 1307 tration at the BM coming from the CT, and equation (2.1) for the digestion of the BM, complemented by
 1308 the quantities obtained from the quasi-state assumptions SA2., *i.e.*

$$c_1 = \frac{k_1 \bar{c}_d}{k_{-1}} c_t, \quad c_2 = \frac{k_2 k_1 \bar{c}_d}{k_{-1}(k_{-2} + k_3)} c_t c_p, \quad c_3 = \left(\frac{k_1}{k_{-1}} \right)^2 \bar{c}_d c_t^2, \quad c_{tp} = \frac{k_2 c_t c_p}{\beta_{tp}}, \quad c_{ta} = \frac{k_2 c_t c_a}{\beta_{ta}}.$$

1309 In the absence of spatial movement in the BM, the reduced system holds pointwise in $x \in \Gamma$.

1310 C.1 Analytical results of the reduced system

1311 We first analyse the steady state of the ODE system (2.25)–(2.27) and its linear stability. We then exploit
 1312 these results to derive sufficient conditions for BM rupture while analysing Equation (2.24).

1313 C.1.1 Steady state

1314 For simplicity, we assume the TIMP-2 and proMMP-2 dynamics in the CT have reached an equilibrium
 1315 and denote their equilibrium value at the BM by

$$\bar{c}_i = \bar{c}_i^* \equiv \bar{c}_i^*(x), \quad i = \{t, p\}, \quad x \in \Gamma. \quad (\text{C.1})$$

1316 **Proposition 7.** *If $\bar{c}_t^* > 0$, denoting*

$$K_R = k_2 + \frac{k_1 k_2 k_3 \bar{c}_d}{k_{-1}(k_{-2} + k_3)}, \quad (\text{C.2})$$

1317 *the steady state solution of the ODE system (2.25)–(2.27) under assumption (C.1) is*

$$\begin{cases} c_t^* = \frac{\hat{\kappa}_t \bar{c}_t^*}{\hat{\kappa}_t + K_R c_p^*}, \\ c_p^* = \sqrt{\left(\frac{\hat{\kappa}_t \bar{c}_t^* - \hat{\kappa}_p \bar{c}_p^*}{2\hat{\kappa}_p} + \frac{\hat{\kappa}_t}{2K_R} \right)^2 + \frac{\hat{\kappa}_t \bar{c}_t^*}{K_R}} - \left(\frac{\hat{\kappa}_t \bar{c}_t^* - \hat{\kappa}_p \bar{c}_p^*}{2\hat{\kappa}_p} + \frac{\hat{\kappa}_t}{2K_R} \right), \\ c_a^* = \frac{k_1 k_3 \bar{c}_d}{k_{-1}(k_{-2} + k_3)} c_p^*. \end{cases} \quad (\text{C.3})$$

1318 *If $\bar{c}_t^* = 0$, the system (2.25)–(2.27) under assumption (C.1) admits infinitely many steady states in the*
 1319 *form*

$$c_t^* = 0, \quad c_p^* = \bar{c}_p^*, \quad c_a^* = C_a, \quad (\text{C.4})$$

1320 *with $C_a \geq 0$ for biological relevance. From the non-negativity of parameters we have that $c_t^*, c_p^*, c_a^* \geq 0$.*

1321 *Proof.* The steady state $Y^* = (c_t^*, c_p^*, c_a^*)$ of system (2.25)–(2.27), under assumption (C.1), satisfies

$$\begin{cases} \hat{\kappa}_t \bar{c}_t^* - k_2 c_t^* (c_p^* + c_a^*) - \hat{\kappa}_t c_t^* = 0, \\ \hat{\kappa}_p \bar{c}_p^* - K_R c_p^* c_t^* - \hat{\kappa}_p c_p^* = 0, \\ (K_R - k_2) c_t^* c_p^* - k_2 c_t^* c_a^* = 0, \end{cases} \quad (\text{C.5})$$

1322 with K_R defined in (C.2). Rearranging (C.5)₁ we obtain

$$c_t^* = \frac{\hat{\kappa}_t \bar{c}_t^*}{\hat{\kappa}_t + k_2 (c_p^* + c_a^*)}. \quad (\text{C.6})$$

1323 Thus, if $\bar{c}_t^* > 0$ we have that $c_t^* \neq 0$ and from (C.5)₃ we retrieve

$$c_a^* = \frac{(K_R - k_2)}{k_2} c_p^* = \frac{k_1 k_3 \bar{c}_d}{k_{-1}(k_{-2} + k_3)} c_p^*, \quad (\text{C.7})$$

1324 *i.e.* (C.3)₃. Substituting (C.7) in (C.6) we obtain

$$c_t^* = \frac{\hat{\kappa}_t \bar{c}_t^*}{\hat{\kappa}_t + K_R c_p^*}, \quad (\text{C.8})$$

1325 *i.e.* (C.3)₁. Substituting (C.8) in (C.5)₂, multiplying by $(\hat{\kappa}_t + K_R c_p^*)$ and rearranging, we obtain

$$[\hat{\kappa}_p K_R] (c_p^*)^2 + [\hat{\kappa}_p \hat{\kappa}_t + K_R (\hat{\kappa}_t \bar{c}_t^* - \hat{\kappa}_p \bar{c}_p^*)] c_p^* - \hat{\kappa}_p \hat{\kappa}_t \bar{c}_p^* = 0. \quad (\text{C.9})$$

1326 Thus we have

$$c_p^* = \sqrt{\left(\frac{\hat{\kappa}_t \bar{c}_t^* - \hat{\kappa}_p \bar{c}_p^*}{2\hat{\kappa}_p} + \frac{\hat{\kappa}_t}{2K_R} \right)^2 + \frac{\hat{\kappa}_t \bar{c}_t^*}{K_R}} - \left(\frac{\hat{\kappa}_t \bar{c}_t^* - \hat{\kappa}_p \bar{c}_p^*}{2\hat{\kappa}_p} + \frac{\hat{\kappa}_t}{2K_R} \right),$$

1327 *i.e.* (C.3)₂, where we have chosen the largest root of (C.9) to ensure non-negativity of the proMMP-2
1328 concentration c_p^* , for biological relevance, which indeed we have from the non-negativity of the parameter
1329 values. Having $c_p^* \geq 0$, we also have that $c_a^* \geq 0$ and $c_t^* \geq 0$ from (C.7) and (C.8), respectively.

1330 On the other hand, if $\bar{c}_t^* = 0$, we automatically have from (C.6) that $c_t^* = 0$. Then, from (C.5)₂ we
1331 have that $c_p^* = \bar{c}_p^*$, while equation (C.5)₃ becomes an identity and any value of $c_a^* = C_a \geq 0$ qualifies as
1332 a biologically relevant steady state. Altogether, this gives (C.4). \square

1333 C.1.2 Condition for BM rupture

1334 We consider rupture of the BM to have occurred if the BM density M goes below a critical value M_{crit} ,
1335 low enough to allow cancer cells to pass through. While this may temporarily happen in short finite time,
1336 we focus on the case in which BM rupture is sustained in the long-term, *i.e.*

$$M^*(x) < M_{\text{crit}} < M_{\text{max}} \quad \text{for some } x \in \Gamma, \quad (\text{C.10})$$

1337 where M^* is the BM density at equilibrium.

1338 **Proposition 8.** *Assuming the system evolves according to the dynamics described by (2.24)–(2.27), under*
1339 *(C.1) and assuming $\bar{c}_t^*(x) > 0$ for some $x \in \Gamma$, long-term sustained BM rupture (C.10) will occur if*

$$C_{RUP}(x) > 0 \quad \text{for some } x \in \Gamma, \quad (\text{C.11})$$

1340 where C_{RUP} is defined as

$$C_{RUP}(x) = \frac{k_1 k_3 \bar{c}_d}{k_{-1}(k_{-2} + k_3)} c_p^*(x) - \frac{r_M}{\gamma} \left(1 + \frac{K_M}{M_{\text{crit}}} \right) \left(1 - \frac{M_{\text{crit}}}{M_{\text{max}}} \right), \quad (\text{C.12})$$

1341 with c_p^* given in (C.3)₂.

1342 *Proof.* We know from Proposition (7) that at the $x \in \Gamma$ where $\bar{c}_t^*(x) > 0$, the steady state concentrations
1343 of TIMP-2, proMMP-2 and active MMP-2 are given by (C.3). For BM rupture (C.10) to occur the
1344 following must hold

$$\left. \frac{dM}{dt} \right|_{c_a^*, M_{\text{crit}}} < 0,$$

1345 which from (2.24) gives

$$-\gamma c_a^* \frac{M_{\text{crit}}}{K_M + M_{\text{crit}}} + r_M \left(1 - \frac{M_{\text{crit}}}{M_{\text{max}}} \right) < 0.$$

1346 Rearranging this and plugging in c_a^* from (C.3)₃, we obtain (C.11) under definition (C.12). \square

D Details of the numerical scheme for System (2.1)–(2.13)

In this section, we describe the discretization of our system that combines a cell-centered finite volume spatial discretization and an explicit Runge-Kutta time integration method. We describe separately the case $\dim(\Omega) = 2, \dim(\Gamma) = 1$ and the case $\dim(\Omega) = 1, \dim(\Gamma) = 0$.

We describe the discretization of the prototypical system for TIMP-2

$$\partial_t \bar{c}_t - D_t \Delta \bar{c}_t = S_t(x, t) - \beta_t \bar{c}_t, \quad \Omega \times (0, T), \quad (\text{D.1})$$

$$-D_t \nabla \bar{c}_t \cdot \nu = \kappa_t (\bar{c}_t - c_t), \quad \Gamma \times (0, T), \quad (\text{D.2})$$

$$-D_t \nabla \bar{c}_t \cdot \nu = 0, \quad \partial\Omega \setminus \Gamma \times (0, T), \quad (\text{D.3})$$

$$\partial_t c_t = \hat{\kappa}_t (\bar{c}_t - c_t) + R_t - \beta_t c_t, \quad \Gamma \times (0, T). \quad (\text{D.4})$$

D.1 Spatial discretization

Case $\dim(\Omega) = 2, \dim(\Omega_{\text{BM}}) = 1$. We assume that the domain $\Omega = [0, L] \times [0, L]$ is a square of side length L . Let $\mathcal{T} = (K_{ij})_{i=1, \dots, N_{x_1}; j=1, \dots, N_{x_2}}$ (with N_{x_1}, N_{x_2} the number of nodes in the x_1 and x_2 direction respectively) be an admissible mesh for Ω in the sense of [34, Proposition 9.2]. For simplicity, we use equal square control volumes (we also use the denomination "cells" for the control volumes), *i.e.* $h_i = h = k_j$ for $i = 1, \dots, N_{x_1}, j = 1, \dots, N_{x_2}$ (h_i, k_j being the side lengths of the control volume $K_{i,j}$ in the x_1 and x_2 directions respectively) and $N_{x_1} = N_{x_2} = N_x$.

We approximate the concentration \bar{c}_t with its cell-averages stored at the cell centers *i.e.*

$$\bar{c}_t(x, t) \approx \bar{c}_{t,i,j} = \frac{1}{|K_{i,j}|} \int_{K_{i,j}} \bar{c}_t \, dx.$$

We formulate the finite volume discretization of equation (D.1) in any control-volume $K_{i,j}$: we have the semi-discrete problem

$$\frac{d\bar{c}_{t,i,j}}{dt} - \frac{1}{|K_{i,j}|} \int_{\partial K_{i,j}} D_t \nabla \bar{c}_{t,i,j} \cdot \nu \, ds = \frac{1}{|K_{i,j}|} \int_{K_{i,j}} S_t \, dx - \beta_t \bar{c}_{t,i,j}.$$

We discretize the flux in an interior cell (*i.e.* for any $i, j = 2, \dots, N_x - 1$) in the standard way using two-point flux approximation

$$\int_{\partial K_{i,j}} D_t \nabla \bar{c}_{t,i,j} \cdot \nu \, ds = h_i \left(F_{i,j+\frac{1}{2}} - F_{i,j-\frac{1}{2}} \right) + k_j \left(F_{i+\frac{1}{2},j} - F_{i-\frac{1}{2},j} \right),$$

with *e.g.*

$$F_{i,j+\frac{1}{2}} = D_t \frac{\bar{c}_{t,i,j+1} - \bar{c}_{t,i,j}}{\frac{1}{2}(k_{j+1} + k_j)}.$$

Furthermore, we approximate the source term as its average on each cell as the concentration, *i.e.*

$$\frac{1}{|K_{i,j}|} \int_{K_{i,j}} S_t \, dx = S_{t,i,j}.$$

Altogether, for each interior cell $K_{i,j}$, we have

$$\frac{d\bar{c}_{t,i,j}}{dt} - \frac{1}{|K_{i,j}|} \left(h_i \left(F_{i,j+\frac{1}{2}} - F_{i,j-\frac{1}{2}} \right) + k_j \left(F_{i+\frac{1}{2},j} - F_{i-\frac{1}{2},j} \right) \right) = S_{t,i,j} - \beta_t \bar{c}_{t,i,j}.$$

As we assumed square cells, the equation simplifies to

$$\frac{d\bar{c}_{t,i,j}}{dt} - \frac{D_t}{h^2} (\bar{c}_{t,i,j+1} - 4\bar{c}_{t,i,j} + \bar{c}_{t,i,j-1} + \bar{c}_{t,i+1,j} + \bar{c}_{t,i-1,j}) = S_{t,i,j} - \beta_t \bar{c}_{t,i,j}.$$

For a cell touching the boundary $\partial\Omega \setminus \Gamma$, the corresponding flux *e.g.* $F_{i-1,j}$ for a cell touching the left boundary of Ω , we have $F_{i-1,j} = 0$.

For a cell touching the boundary Γ , the discretization is different to take into account the Robin boundary condition. We first describe how Equation (D.4) is discretized. The one dimensional domain Γ is partitioned into N_x one dimensional cells C_i . The TIMP-2 concentration in each of these cells is approximated by its average such that we have

$$\frac{dc_{t,i}}{dt} = \hat{\kappa}_t (\bar{c}_{t,i,N_y} - c_{t,i}) + R_{t,i} - \beta_t c_{t,i},$$

1374 for all $i = 1, \dots, N_x$, in which we approximated the integral of the reaction term R_t over the cell C_i , is
 1375 approximated by its average denoted $R_{t,i}$.

1376 Assuming that the BM, Γ , corresponds to the top boundary of Ω . For any $K_{i,j}$ with $i = 1, \dots, N_x$ and
 1377 $j = N_y$, we have

$$F_{i,j+\frac{1}{2}} = D_t \nabla c_{t,i,j+\frac{1}{2}} = -\kappa_t (\bar{c}_{t,i,j} - c_{t,i}).$$

1378 **Case $\dim(\Omega) = 1, \dim(\Omega_{\text{BM}}) = 0$.** We assume that the BM, denoted by the boundary Γ , is located
 1379 at the right-hand side of the domain, *i.e.* $x = L$. As in the previous subsection, we use the finite volume
 1380 method and partition the domain $\Omega = [0, L]$ (L being the size of the domain) in equally sized control
 1381 volumes $\mathcal{T} = (K_i)_{i=1, \dots, N_x}$. The size of each cell is denoted h . We approximate the concentration \bar{c}_t
 1382 in each cell with its average $c_{t,i}$. The semi-discrete form of Equation (D.1) is

$$\frac{d\bar{c}_{t,i}}{dt} - \frac{D_t}{h} (F_{i+\frac{1}{2}} - F_{i-\frac{1}{2}}) = S_{t,i} - \beta_t \bar{c}_{t,i},$$

1383 for $i = 2, \dots, N_x - 1$. The flux is defined by

$$F_{i+\frac{1}{2}} = \frac{\bar{c}_{t,i+1} - \bar{c}_{t,i}}{h}, \quad F_{i-\frac{1}{2}} = \frac{\bar{c}_{t,i} - \bar{c}_{t,i-1}}{h}.$$

1384 for the leftmost cell, *i.e.* $i = 1$, the flux $F_{i-\frac{1}{2}} = 0$ For the rightmost cell, the flux $F_{i+\frac{1}{2}} = -\kappa_t (\bar{c}_{t,i} - c_t)$,
 1385 with c_t being the concentration in the BM given by the ODE (D.4).

1386 D.2 Time integration scheme

1387 Our semi-discrete system is solved using the *ode15s* function of the MATLAB ODE suite [100]. This
 1388 function is a variable step, variable order integration method used to integrate stiff problems (see [100]
 1389 for details about the algorithm).

E Supplementary figures

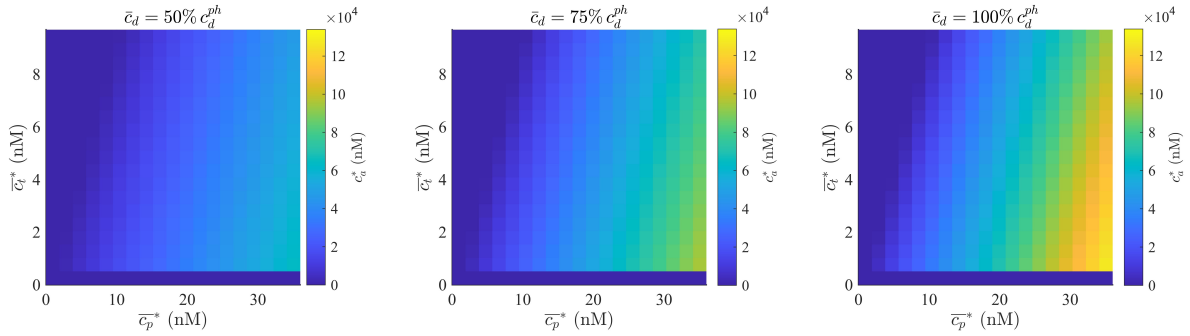


Figure S1: Concentration of active MMP-2 at steady state of the reduced ordinary differential equation (ODE) system (2.25)–(2.27), for varying MT1-MMP dimer concentrations \bar{c}_d corresponding to 50% (left), 75% (center) and 200% (right) of the physiological value c_d^{ph} in Table 1. The remaining details are analogous to those of Figure 3.

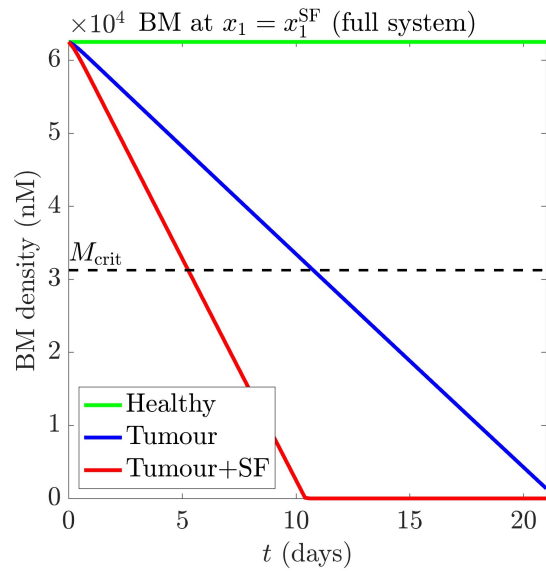


Figure S2: BM density for the healthy (green), tumour (blue) and tumour+SF (red) test cases predicted by the full model over the course of 21 days (3 weeks). The remaining details are analogous to those of Figure 4 (right plot).

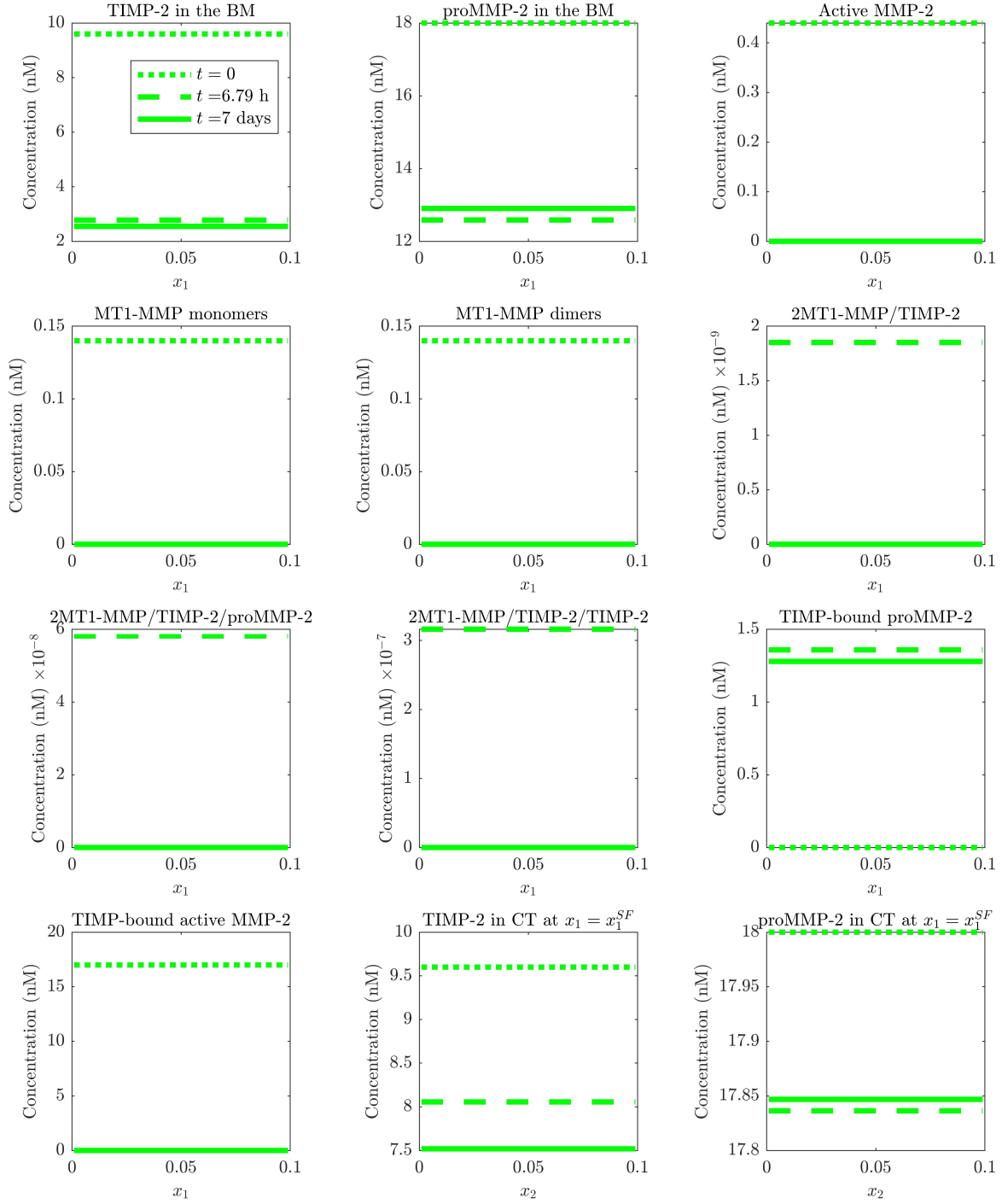


Figure S3: Molecular concentrations in the BM (represented here as the x_1 axis) at $t = 0$ days (dotted line), $t \approx 6.79$ hours (dashed line) and $t = 7$ days (solid line) predicted by the full model for the healthy test case. The remaining details are analogous to those of Figure 4 (healthy test case). We observe a decay of both TIMP-2 and proMMP-2 concentrations and a stabilization to steady values. The active MMP-2 concentration decay to 0 exponentially fast from natural decay and inhibition by TIMP-2. As no tumor cells are present in this test case, MT1-MMP concentration decays to 0 and activation of proMMP-2 is null.

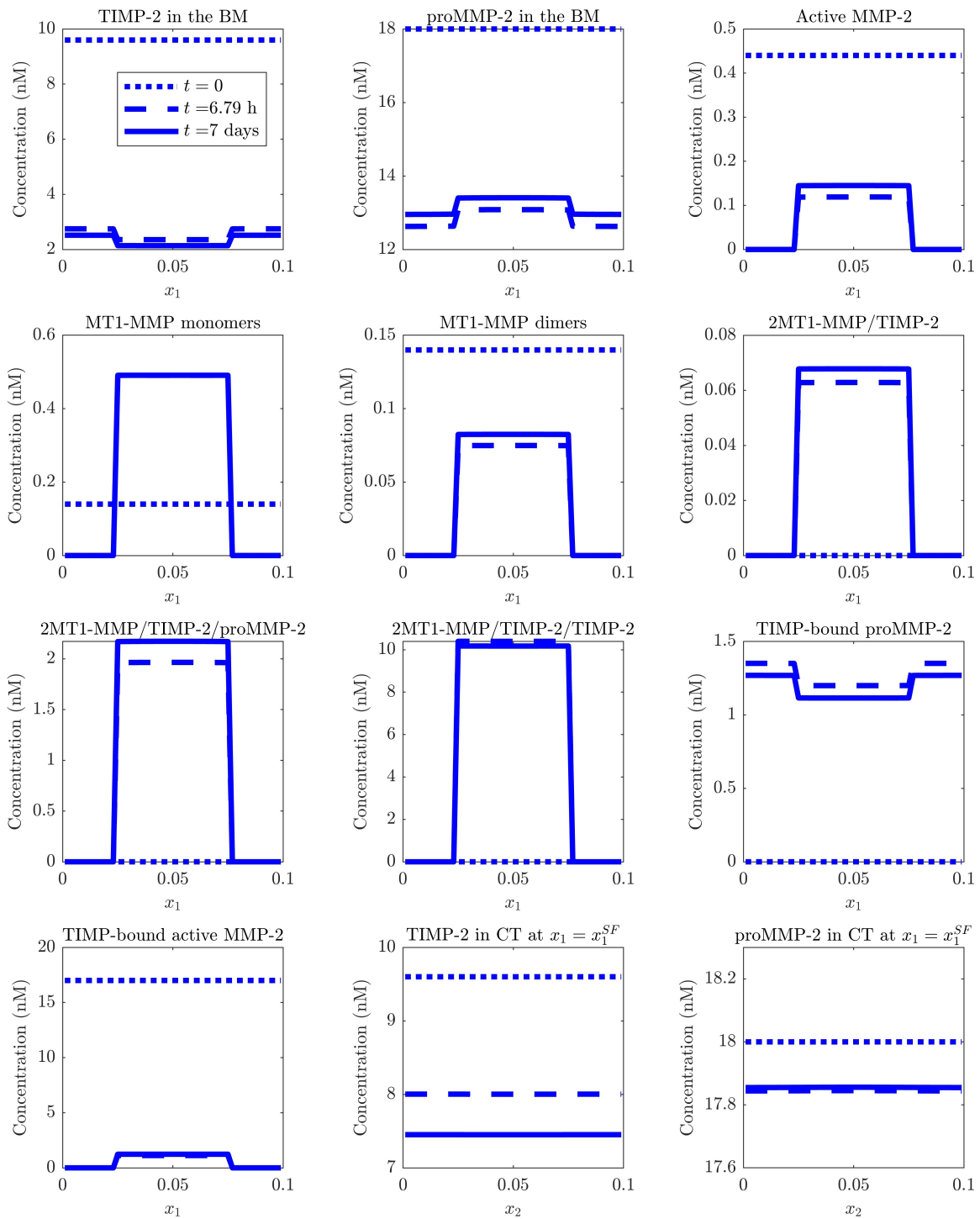


Figure S4: Molecular concentrations at the BM (represented here as the x_1 axis) at $t = 0$ days (dotted line), $t \approx 6.79$ hours (dashed line) and $t = 7$ days (solid line) predicted by the full model for the tumour test case. The remaining details are analogous to those of Figure 4 (tumour test case).

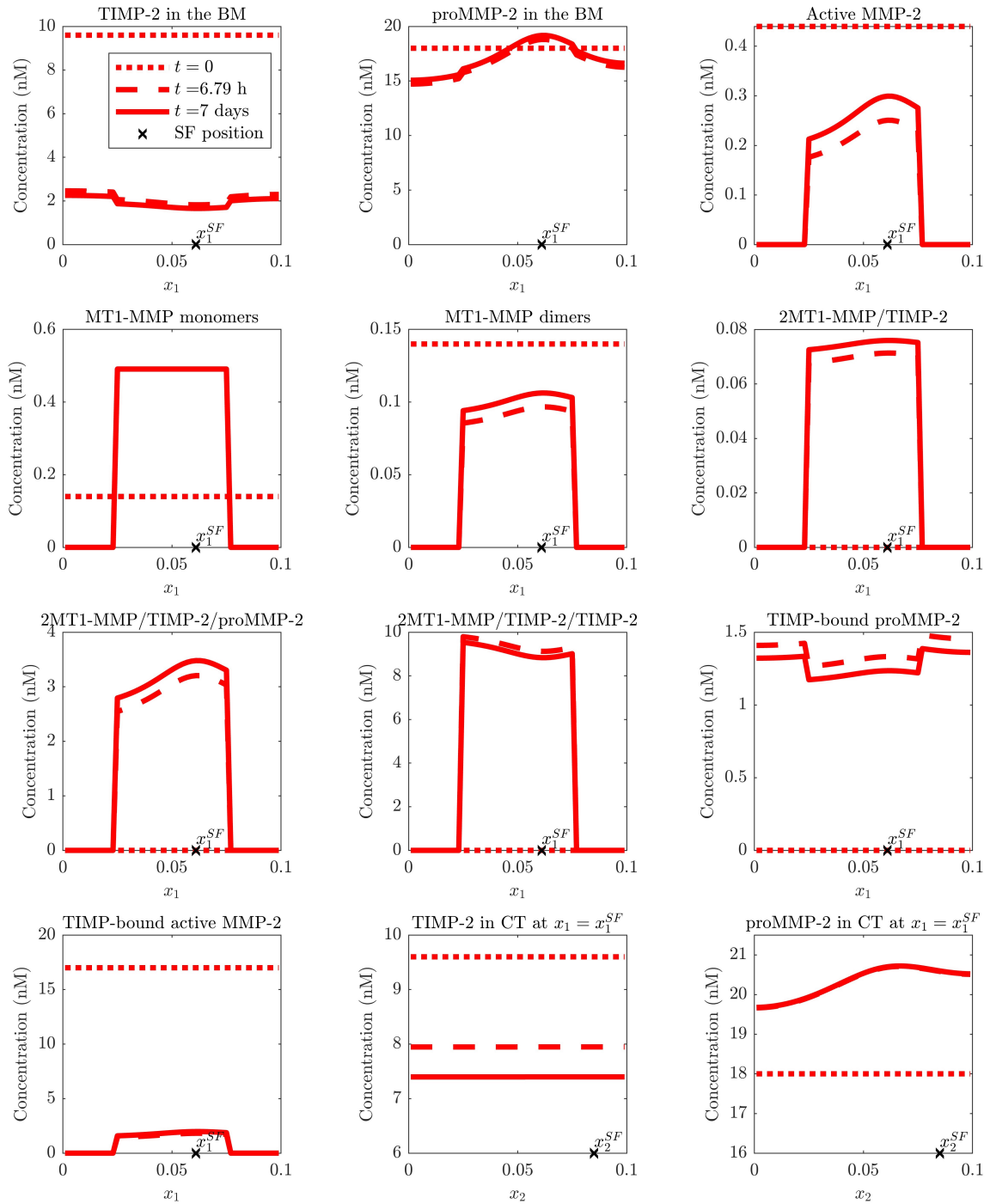


Figure S5: Molecular concentrations at the BM (represented here as the x_1 axis) at $t = 0$ days (dotted line), $t \approx 6.79$ hours (dashed line) and $t = 7$ days (solid line) predicted by the full model for the tumour+SF test case. The remaining details are analogous to those of Figure 4 (tumour+SF test case).